
Masters Theses

Student Theses and Dissertations

Summer 2015

The development of near field probing systems for EMC near field visualization and EMI source localization

Hui He

Follow this and additional works at: https://scholarsmine.mst.edu/masters_theses



Part of the [Electromagnetics and Photonics Commons](#)

Department:

Recommended Citation

He, Hui, "The development of near field probing systems for EMC near field visualization and EMI source localization" (2015). *Masters Theses*. 7435.

https://scholarsmine.mst.edu/masters_theses/7435

This thesis is brought to you by Scholars' Mine, a service of the Missouri S&T Library and Learning Resources. This work is protected by U. S. Copyright Law. Unauthorized use including reproduction for redistribution requires the permission of the copyright holder. For more information, please contact scholarsmine@mst.edu.

THE DEVELOPMENT OF NEAR FIELD PROBING SYSTEMS

FOR EMC NEAR FIELD VISUALIZATION

AND EMI SOURCE LOCALIZATION

by

HUI HE

A THESIS

Presented to the Graduate Faculty of the

MISSOURI UNIVERSITY OF SCIENCE AND TECHNOLOGY

In Partial Fulfillment of the Requirements for the Degree

MASTER OF SCIENCE IN ELECTRICAL ENGINEERING

2015

Approved by

David Pommerenke, Advisor

Jun Fan

Victor Khilkevich

© 2015

Hui He

All Rights Reserved

ABSTRACT

The objectives of this research are to visualize the frequency dependent electromagnetic field distribution for electromagnetic compatibility (EMC) applications and the radiating source reconstruction on complex shaped electronic systems. This is achieved by combining near field probing with a system for automatically recording the probe position and orientation. Due to the complexity of the shape of the electronic systems of interest, and for utilizing the expertise of the user, the probe will be moved manually not robotically. Concurrently, the local near field will be recorded, associated with the location and displayed at near real time on the captured 3D geometry as a field strength map for EMC applications and, for source reconstruction, a reconstructed image showing the far field radiating sources.

ACKNOWLEDGMENTS

Foremost, I would like to express my sincere gratitude to my advisor Prof. David Pommerenke for the continuous support of my study and research, for his patience, motivation, enthusiasm, and immense knowledge. His guidance helped me in all the time of research and writing of this thesis. I could not have imagined having a better advisor for my study.

Besides my advisor, I would like to thank the rest of my thesis committee: Prof. Jun Fan, Prof. Victor Khilkevich for their encouragement, insightful comments, and hard questions.

My sincere thanks also go to Dr. James Drewniak, Dr. Daryl Beetner, and Dr. Yaojiang Zhang, for leading me working on diverse projects.

I thank my fellow lab mates in EMC group of Missouri S&T for the stimulating discussions, for the sleepless nights we were working together before deadlines, and for all the fun we have had in the last three years.

Last but not least, I would like to thank my family: my parents Liping He and Meizhu Tan, for giving birth to me at the first place and supporting me spiritually throughout my study life.

TABLE OF CONTENTS

| | |
|-------------------------------------------------------------------|-----|
| ABSTRACT | iii |
| ACKNOWLEDGMENTS | iv |
| LIST OF ILLUSTRATIONS | vii |
| LIST OF TABLES | xii |
| SECTION | |
| 1. INTRODUCTION | 1 |
| 1.1. RESEARCH MOTIVATION | 1 |
| 1.2. SYSTEM USING FLOWCHART | 5 |
| 1.3. SYSTEM ARCHITECTURE | 6 |
| 2. HARDWARE IMPLEMENTATION | 10 |
| 2.1. TRIANGULATION BASED SYSTEM..... | 10 |
| 2.1.1. Hardware Components | 11 |
| 2.1.2. Modified EMC Scanning Probe | 15 |
| 2.1.3. Determination of the Position of the Probe Tail..... | 16 |
| 2.1.4. Determination of the Position of the Probe Tip. | 18 |
| 2.1.5. Determination of the Orientation of the Probe. | 20 |
| 2.1.6. Accuracy Test of the System..... | 22 |
| 2.2. CMM ARM BASED POSITION DETERMINATION SYSTEM | 25 |
| 2.2.1. Mechanical Design and Assembly | 26 |
| 2.2.2. Sensors Used for this Structure. | 26 |
| 2.2.3. Circuit Schematics for Angle Recording..... | 28 |
| 2.2.4. Calibrating the Angle at the Local Joints. | 29 |
| 2.2.5. Mechanical Calculation..... | 30 |
| 2.2.6. System Accuracy Test | 34 |
| 2.3. OPTICAL TRACKING BASED SYSTEM | 39 |
| 2.3.1. Modified EMI Scanning Probe..... | 41 |
| 2.3.2. Positioning Accuracy of the System | 43 |
| 2.3.3. Orientation of the Probe. | 44 |
| 2.3.4. Optical Tracking System Setup and System Calibration | 45 |

| | |
|--------------------------------------------------------------------|-----|
| 2.3.5. Near Field Scanning Setup | 62 |
| 2.4. COMPARISON OF THE THREE SYSTEM..... | 63 |
| 3. NEAR FIELD VISUALIZATION..... | 65 |
| 3.1. NEAR FIELD SCANNING PROBE..... | 65 |
| 3.2. NEAR FIELD SCANNING TEST CASE..... | 67 |
| 3.3. FIELD DISTRIBUTION FROM INTERPOLATION | 70 |
| 3.4. EMC STUDIO SIMULATION | 71 |
| 3.5. VISUALIZATION OF THE NEAR FIELD STRENGTH IN 3D..... | 74 |
| 3.5.1. 3D Visualization of the Near Field Strength | 74 |
| 3.5.2. A Commercial Product Near-Field Scan..... | 80 |
| 3.5.3. Test Setup..... | 81 |
| 3.5.4. Test Result..... | 83 |
| 4. SAR 2D IMAGING..... | 84 |
| 4.1. EMISSION SOURCE MICROSCOPY ALGORITHM..... | 85 |
| 4.2. OPTICAL TRACKING BASED EMISSION SOURCE MICROSCOPY | 87 |
| 4.3. MEASUREMENT EXAMPLES | 88 |
| 4.3.1. Location Construction of Two Antennas | 88 |
| 4.3.2. Localization of Two Printed Antennas..... | 93 |
| 4.3.3. Reconstruction of Source with Metal Plate Interference..... | 97 |
| 4.3.4. A box with A Slot on One Side | 99 |
| 4.3.5. EMI Scanning..... | 102 |
| 5. CONCLUSIONS AND FUTURE WORK..... | 106 |
| 5.1. CONCLUSION..... | 106 |
| 5.2. FUTURE WORK..... | 107 |
| BIBLIOGRAPHY..... | 108 |
| VITA | 111 |

LIST OF ILLUSTRATIONS

| | |
|------------------------------------------------------------------------------------------|----|
| Figure 1.1. Robotic near field scanning system from API..... | 4 |
| Figure 1.2. Example of portable CMM arm [7]..... | 5 |
| Figure 1.3. Flowchart of probe tracking based EMI scanning system..... | 6 |
| Figure 1.4. Configuration of the CMM arm based system | 7 |
| Figure 2.1. Draw wire sensor based system..... | 10 |
| Figure 2.2. Draw wire sensor CAD model | 12 |
| Figure 2.3. Draw wire sensor..... | 12 |
| Figure 2.4. CAN interface based digital encoder..... | 13 |
| Figure 2.5. Orientation sensor..... | 13 |
| Figure 2.6. CAN to USB convertor | 14 |
| Figure 2.7. CAN bus connection schematic..... | 15 |
| Figure 2.8. CAN bus | 15 |
| Figure 2.9. Modified EMI scanning probe..... | 16 |
| Figure 2.10. Coordinate system for determining the position of the probe tail..... | 17 |
| Figure 2.11. Orientation sensor used for calculating the location of the probe tip..... | 18 |
| Figure 2.12. Coordinate system for calculating the position of the probe tip..... | 19 |
| Figure 2.13. Convention of the pitch and roll orientation..... | 19 |
| Figure 2.14. Geometric elements required to determine the orientation of the probe | 20 |
| Figure 2.15. Mechanical design for the probe recording system..... | 25 |
| Figure 2.16. CMM arm based system..... | 26 |
| Figure 2.17. Hinge joint..... | 27 |
| Figure 2.18. Pivot joint | 27 |

| | |
|-------------------------------------------------------------------------------------|----|
| Figure 2.19. Circuit diagram for angle recording | 28 |
| Figure 2.20. Angle calibration | 29 |
| Figure 2.21. Schematic for angle calibration | 30 |
| Figure 2.22. CMM structure with probe attached to the end axes | 32 |
| Figure 2.23. Input for calculating the position of tip of the probe | 32 |
| Figure 2.24. First repeatability test | 34 |
| Figure 2.25. Repeatability test 2 | 35 |
| Figure 2.26. Repeatability test 3 | 37 |
| Figure 2.27. Points collection test setup | 38 |
| Figure 2.28. CMM arm based system | 38 |
| Figure 2.29. Optical tracking hardware | 40 |
| Figure 2.30. Configuration of the CMM arm based system | 41 |
| Figure 2.31. Rigid body target for object tracking from Iotracker [20] | 42 |
| Figure 2.32. Modified EMI probe for position and orientation tracking | 42 |
| Figure 2.33. A probe tracked and modeled in optical tracking software | 43 |
| Figure 2.34. Euler angles provided by the tracking software | 44 |
| Figure 2.35. Hardware connection scheme | 46 |
| Figure 2.36. A switch implemented through DAQ for pausing scanning | 46 |
| Figure 2.37. Optitrack Motive startup window | 47 |
| Figure 2.38. Changing video type | 48 |
| Figure 2.39. Wand use to calibrate the optical tracking system | 49 |
| Figure 2.40. Wand calibration in progress | 49 |
| Figure 2.41. Calibration calculation in progress, waiting to apply the result | 50 |

| | |
|------------------------------------------------------------------------------------------|----|
| Figure 2.42. Calibration calculation complete | 50 |
| Figure 2.43. Calibration results applied, save the calibration | 51 |
| Figure 2.44. L-shape ground plane reference body | 52 |
| Figure 2.45. Setting up the ground plane reference | 52 |
| Figure 2.46. Saving the ground plane reference calibration | 53 |
| Figure 2.47. Field probe with rigid body fixed on top of it. | 54 |
| Figure 2.48. Rigid body markers seen in Motive software..... | 54 |
| Figure 2.49. Rigid body markers seen in Motive software..... | 55 |
| Figure 2.50. Rigid body and probe with an extra marker at the tip of probe..... | 56 |
| Figure 2.51. Rigid body with an extra marker at the tip of probe..... | 56 |
| Figure 2.52. Top view for rigid body center translation | 57 |
| Figure 2.53. Z-translation being applied in the top view | 58 |
| Figure 2.54. Location of big marker after Z-translation in top view | 58 |
| Figure 2.55. X-translation being applied in the top view | 59 |
| Figure 2.56. Changing of view to left view to move the marker in the Y-orientation | 59 |
| Figure 2.57. Y-translation being applied in the left view | 60 |
| Figure 2.58. Location of big marker after Y-translation in left view | 60 |
| Figure 2.59. Data Streaming | 61 |
| Figure 2.60. Real-time tracking of the big marker (Right window) | 62 |
| Figure 2.61. Optical tracking based near field scanning setup | 63 |
| Figure 3.1. H-field probe used for hand scanning | 66 |
| Figure 3.2. H-field probe's frequency response..... | 67 |
| Figure 3.3. Optical tracking based manual scanning | 68 |

| | |
|-------------------------------------------------------------------------------------|----|
| Figure 3.4. Aluminum test box with a probe over the slot | 69 |
| Figure 3.5. Hardware setup with DUT placed within the field of coverage | 69 |
| Figure 3.6. Real-time scatter plot of the fields on the top surface of the DUT..... | 70 |
| Figure 3.7. Near field scanning from manual scanning (Unit: dBA/m) | 71 |
| Figure 3.8. Voltage source modeling..... | 72 |
| Figure 3.9. Geometry modeling | 72 |
| Figure 3.10. The complete model | 73 |
| Figure 3.11. The mesh model | 73 |
| Figure 3.12. Near field from manual scanning (Unit: dBA/m)..... | 74 |
| Figure 3.13. Real time scan points plot..... | 75 |
| Figure 3.14. Interpolated 3D near field distribution (unit: dBA/m) | 76 |
| Figure 3.15. Flow chart of real time 3D near field manual scanning | 78 |
| Figure 3.16. Scan result of the test DUT with coarse meshing (unit: dBA/m)..... | 79 |
| Figure 3.17. Scan result of the test DUT with adaptive meshing (unit: dBA/m) | 79 |
| Figure 3.18. DUT – a laptop with cable connected | 80 |
| Figure 3.19. Mesh model for 3D field overlay | 81 |
| Figure 3.20. Setup for near field visualization measurement | 82 |
| Figure 3.21. 3D model for near field visualization..... | 82 |
| Figure 3.22. H-field strength (dB scale) | 83 |
| Figure 4.1. Principle of the 2D imaging system | 88 |
| Figure 4.2. Measurement setup schematic..... | 89 |
| Figure 4.3. Ground plane calibration | 89 |
| Figure 4.4. Gimbal stabilizer for holding measurement probe | 90 |

| | |
|----------------------------------------------------------------------------------|-----|
| Figure 4.5. 3D printed fixture for mounting probe on gimbal stabilizer | 90 |
| Figure 4.6. Two antennas placed behind foam-core board | 91 |
| Figure 4.7. Actual measurement setup..... | 92 |
| Figure 4.8. Measurement results..... | 93 |
| Figure 4.9. Board patch layout..... | 94 |
| Figure 4.10. Custom board with a waveguide above..... | 94 |
| Figure 4.11. Measurement setup..... | 95 |
| Figure 4.12. Reconstructed E_x field magnitude (V/m) on the source plane..... | 96 |
| Figure 4.13. Reconstructed E_y field magnitude (V/m) on the source plane..... | 96 |
| Figure 4.14. Measurement setup of two active sources | 97 |
| Figure 4.15. Measured field strength on the scanning plane | 98 |
| Figure 4.16. Reconstructed image on the source plane | 99 |
| Figure 4.17. A box with a slot on one side | 100 |
| Figure 4.18. Measurement setup..... | 100 |
| Figure 4.19. Reconstructed source at 1 GHz | 101 |
| Figure 4.20. Reconstructed source at 6 GHz | 102 |
| Figure 4.21. Metal plate with holes | 103 |
| Figure 4.22. Metal plate covered by aluminum foil..... | 103 |
| Figure 4.23. Measurement setup..... | 104 |
| Figure 4.24. Measurement setup and reconstructed source image (in dB scale)..... | 104 |
| Figure 4.25. Measurement setup and reconstructed source image (in dB scale)..... | 105 |

LIST OF TABLES

| | |
|----------------------------------------------------------------------------------|----|
| Table 1.1. Comparison of the characteristics of different scanning methods | 3 |
| Table 2.1. List of the hardware components used in this system | 11 |
| Table 2.2. Hold the probe vertical on the table (Units: mm) | 23 |
| Table 2.3. Drag the probe to the same point on the table (Units: mm)..... | 23 |
| Table 2.4. Error sources of the system..... | 24 |
| Table 2.7. First repeatability test (Unit: mm) | 35 |
| Table 2.8. Repeatability test 2 (Unit: mm) | 36 |
| Table 2.9. Repeatability test 3 (Unit: mm) | 37 |
| Table 2.10. Positioning accuracy repeatability test sample data (Unit: m) | 44 |

1. INTRODUCTION

1.1. RESEARCH MOTIVATION

Local electromagnetic near field scanning has been used to reveal potential sources which cause electromagnetic compatibility (EMC) problems, to determine equivalent source models [1] and to estimate far field [2]. Near field scanning may provide information about the surface current, tangential fields and the reactive near-field distribution on the device under test (DUT). Furthermore, robotic measurement of the surface current density, via the local magnetic field has been used to visualize the spreading of electrostatic discharge (ESD) induced currents [3][4].

In literature, the planar near field data was obtained by robotic scanners or X-Y positioners [5][6], and 3-axis robots [7]. While robotic scanning allows scanning many points on a simple surface, it is nearly impossible to scan a complex shaped system such as an internet back bone router having many cables. Further, the preprogrammed scan maps do not utilize the observations during the scanning to improve the scan strategy or locations. Figure 1.1 shows a robotic scanner, with a complex shaped system as a DUT. For such a DUT, it is very difficult to avoid collision between the measurement probe and the DUT, if one wants to measure the field values of some locations where with many cable routing. In contrast, by manual scanning, experienced engineers will adopt their scanning based on the observed results. They could collect more points on regions where field values are high or change rapidly, and avoid possible collisions.

Ken Sato et al. have developed systems to show the feasibility of this concept. Four types of measurement method have been prototyped by them, which use magnetic tracker [8], optical tracker [9], infrared camera tracker [10], and Wiimote [11][12] as a

probe position sensor. However, such methods have been limited to only performing near field scanning without post processing.

Table 1.1 contrasts manual scanning with probe location recording to automatic scanning, indicates the usefulness of a probe tracking system from a data analysis, 3D visualization and cost stand points. Therefore, the motivation for the development of the proposed system is the need to combine the high density and precision of conventional robotic scanners with less constrained and adaptable scanning abilities of manual near field scanning.

Table 1.1. Comparison of the characteristics of different scanning methods

| Scanning methods | Characteristics | |
|-----------------------------------------|-----------------|--------------------------------------------------------------------------------------------------------------------------------------------------------------------------------------------------------------------------------------------------------------------------------------------------------------------------------------------------------------------------------------------------------------------------------------------------------------------------------------------------------------------------------------------------------------------------------------------------------------------------------------------------------------------------------------------------------------------|
| Robotic scanning | Advantages | <ul style="list-style-type: none"> • Many scan points possible • Relatively large areas with excellent resolution (50 cm ×50 cm typically) • Good resolution (typically less than 0.05 mm) |
| | Dis-advantages | <ul style="list-style-type: none"> • Most scanning is performed sequentially in a pre-programmed fashion, not intelligently updated using the knowledge of an experienced engineer • Difficult to program the movement of a 6 axis robot on complex shaped objects while 3 axis robots are limited to simple scan surfaces • Difficult to update scan point locations or measurement parameters based on findings at other points • Risk of collisions of the heavy and powerful robot arm and the object being scanned • Very large robots needed for large equipment such as a full size rack • Bulky, heavy, expensive, and needs solid floor mount |
| Manual scanning with location recording | Advantages | <ul style="list-style-type: none"> • Quick EMC diagnostics • Can scan complex shaped objects • Uses the experience and insight of user • Can update and modify scanning grid based on preliminary output results • Documentable scan results • Practically scan size unconstrained • Post-processing abilities |
| | Dis-advantages | <ul style="list-style-type: none"> • Difficult to perform measurement for a long time |



Figure 1.1. Robotic near field scanning system from API

Figure 1.2 shows an example of CMM arm. These arms have multiple rotary axes, which have a high degree of freedom for measuring the 3D position of points. The idea here is to develop a system to track the location and orientation of probe for EMC scanning. With position recording, an experienced engineer will adopt his or her scanning based on the observed results.



Figure 1.2. Example of portable CMM arm [7]

Preliminary work in [13][14] showed the usefulness of the proposed system, which combines many advantages of robotic scanning and the flexibility and user intelligence of manual scanning, and a wide range of mathematical post processing over the obtained data. Application of such system includes near field 2D and 3D visualization and far-field radiating EMI source localization.

1.2. SYSTEM USING FLOWCHART

Figure 1.3 shows the flowchart of the developed systems. To visualize the local fields, the user moves the electromagnetic interference (EMI) scanning probe to the points of interest while measuring the near field strength. A spectrum analyzer or an oscilloscope will measure the electric or magnetic field strength as the probe tracking system records the position and orientation of the EMI scanning probe. The recorded information is post processed to overlay field strength on the 3D model of the DUT for EMI analysis. While doing the manual near field scanning, users utilize their observation and intelligence to update scan points on critical regions and also to avoid possible

collisions between probe and the DUT. As a result, complex structures can be scanned efficiently.

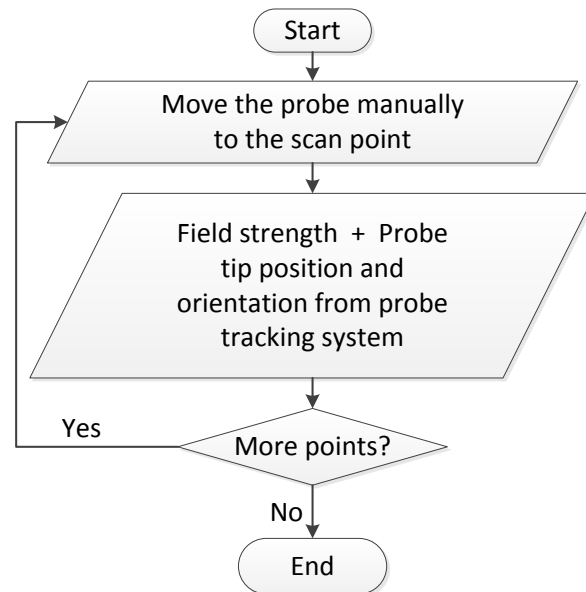


Figure 1.3. Flowchart of probe tracking based EMI scanning system

1.3. SYSTEM ARCHITECTURE

Three types of position recording systems have been developed, including triangulation based position determination system, coordinate measurement (CMM) arm based position determination system, and optical tracking based position determination system.

A magnetic or the electric scanning probe connected with a spectrum analyzer (SA) or vector network analyzer (VNA) is integrated with a probe tracking system, which can be used by an engineer for manual scanning. A SA is used for measuring the

magnitude of near field. A VNA could also be used to measure phase. Figure 1.4 shows the configuration of the system.

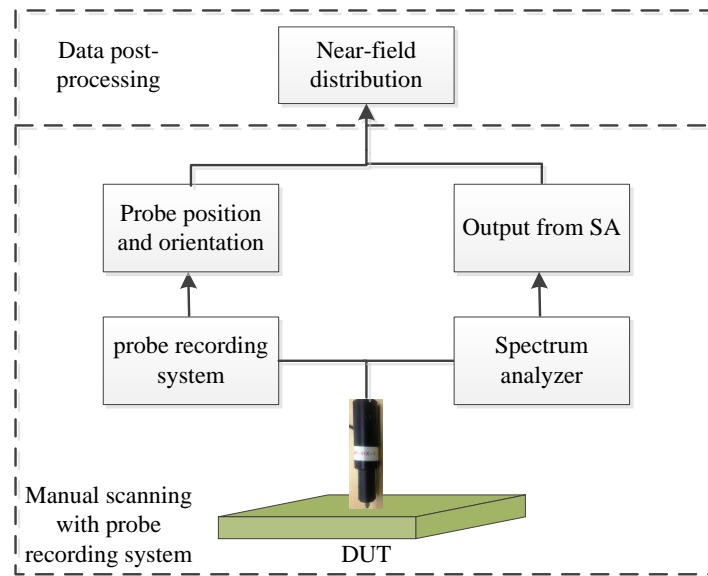


Figure 1.4. Configuration of the CMM arm based system

The system consists of two main components; the probe recording system for determining the location, orientation and documenting the field strengths and, the post-processing software tool for visualization and data manipulation. The software tool takes the input from the probe recording system and estimate the near field distribution.

This system has multiple applications.

- Documentation of manual scanning for visualization of the near field or surface current distribution.
- Estimation of far field radiation [2].
- Identification of potential radiation sources [30].

Publications related to the work discussed in this thesis are:

- 1) H. He, P. Maheshwari, and D. Pommerenke, “Coordinate measurement based EM-field probing system for EMC manual scanning,” submitted to *IEEE transaction on Instrumentation & Measurement*.
- 2) H. He, V. Khilkevich, D. Pommerenke, “Application of Emission Source Microscopy to EMI source localization above 5 GHz,” submitted to *IEEE EMC Symposium, 2015*.
- 3) H. He, P. Maheshwari, and D. Pommerenke, “Optical tracking based EM-field probing system for EMC near field manual scanning,” , *IEEE International Symposium on Electromagnetic Compatibility*, Raleigh, North Carolina, August 3-8, 2014.
- 4) H. He, P. Maheshwari, A. Radchenko, and D. Pommerenke, “EM radiation estimation using an automatic probe position recording system coupled to hand scanning,” *IEEE International Symposium on Electromagnetic Compatibility*, Denver, Colorado, August 5-9, 2013.

Other publications resulting from master studies are:

- 5) X. Jiao, H. He, G. Li, D. Pommerenke, “Designing a 3D printing based channel emulator”, *IEEE International Symposium on Electromagnetic Compatibility*, Raleigh, North Carolina, August 3-8, 2014.

- 6) X. Jiao, H. He, G. Li, D. Pommerenke, “Designing 3D printing based channel emulator with printable electromagnetic materials”, submitted to *Special Issue of Transactions on EMC for the 2014 IEEE EMC Symposium* at Raleigh.

2. HARDWARE IMPLEMENTATION

2.1. TRIANGULATION BASED SYSTEM

The first mechanical structure of the manual near field scanning system was prototyped with three draw wire sensors, which utilize multi-turn rotary encoders to record the length of the wire being drawn out. As shown in Fig. 2.1, a wooden table with three supporting rods was built to provide a manual near field scanning platform. The three draw wire sensors were raised half meter above the table to form a planar surface which is parallel to the top surface of the wooden table. The wires from the draw wire sensors are drawn and meet at a joint point, where a modified EMI scanning probe was attached.

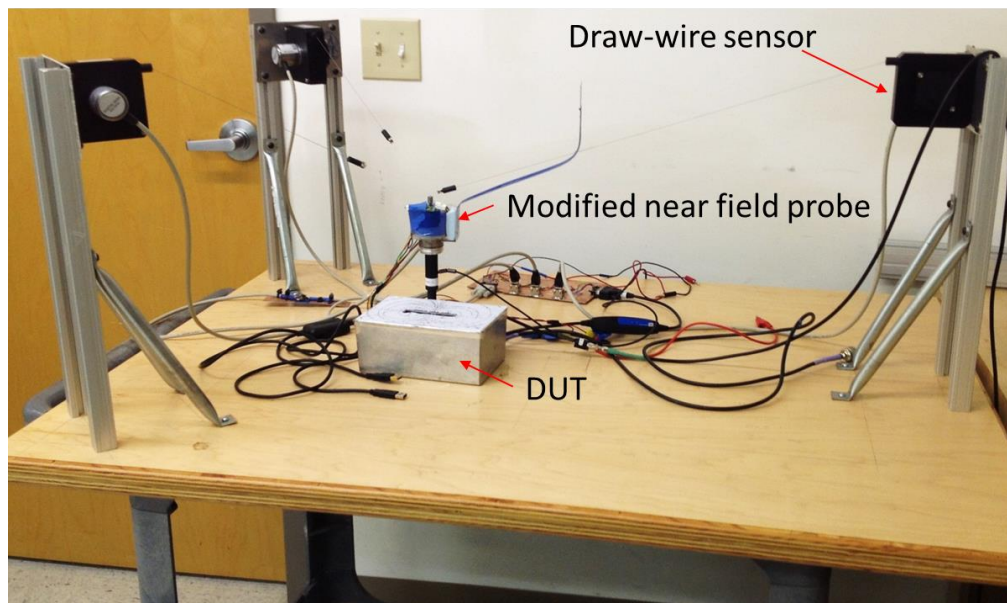


Figure 2.1. Draw wire sensor based system

2.1.1. Hardware Components. The major hardware components for this system are summarized in Table 2.1.

Table 2.1. List of the hardware components used in this system

| Hardware components | Comments |
|----------------------|--------------------------|
| 1 Ply wood table | 3 feet×4 feet×3/4 inch |
| T-slot frame | 18 inches long, 6 pieces |
| Draw wire sensors | From Fraba Posital |
| rotary sensor | From Fraba Posital |
| orientation sensor | From CH Robotics |
| CAN to USB convertor | From Kvaser |
| CAN bus PCB | self-made |

The ply wood table is used as a supporting platform for locating DUT. With this table, the system can be placed at any locations of interest. Draw wire sensors include both multi-turn digital encoder and a string loaded with spring. The major application of this type of sensor is for distance measurement. With the length of wire been drawn out, the digital encoder will turn certain amount of turns, with which the length of the wire been drawn out can be read using computer via CAN to USB interface in a real time fashion. Figure 2.2 shows a CAD model of a draw wire sensor. Figure 2.3 shows a draw wire sensor used in the developed system.

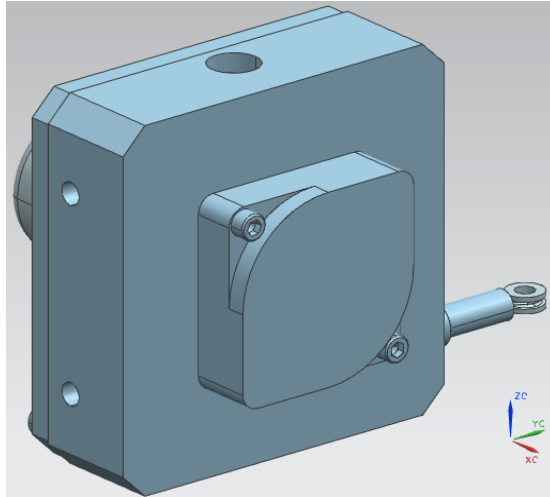


Figure 2.2. Draw wire sensor CAD model



Figure 2.3. Draw wire sensor

Except for three draw wire sensors. Another digital encode is utilized (Fig. 2.4) for recording the phi angle of the probe.

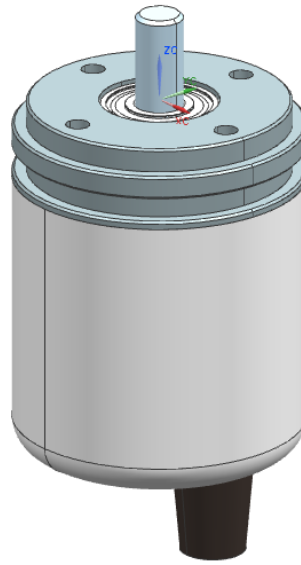


Figure 2.4. CAN interface based digital encoder

An orientation sensor is utilized for calculating the position of the tip of the probe. As shown in Fig. 2.5, the orientation sensor can provide three Euler angles: roll, pitch, and yaw, which are read with series interface: RS232.



Figure 2.5. Orientation sensor

All the digital encoders, including the ones in the draw wire sensors are CAN interface. A Kvaser CAN to USB convertor is utilized to read the data. The CAN to USB convertor is shown by Fig. 2.6.



Figure 2.6. CAN to USB convertor

A CAN bus is made, the connection schematic is shown by Fig. 2.7. The actual board is shown by Fig. 2.8.

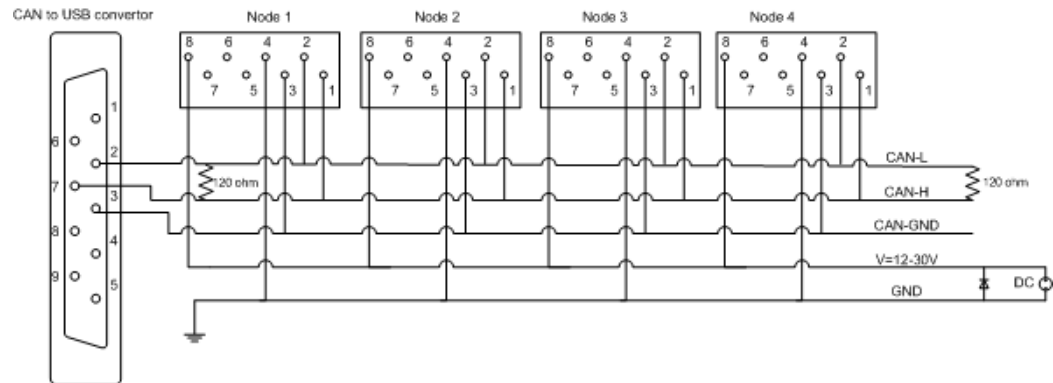


Figure 2.7. CAN bus connection schematic

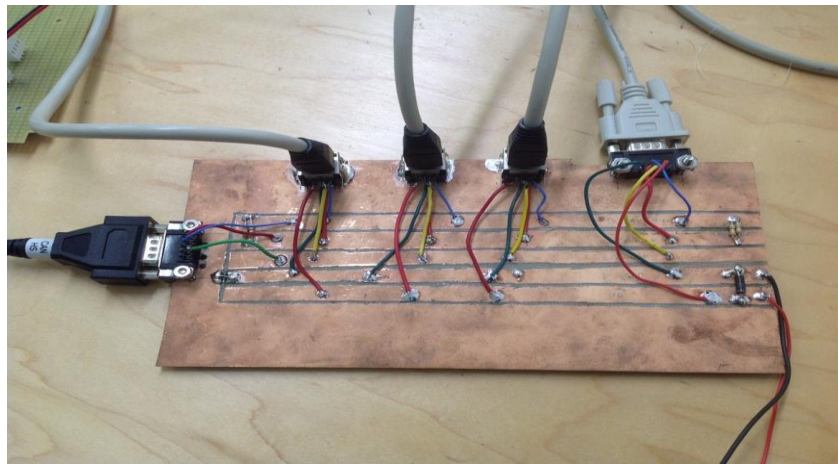


Figure 2.8. CAN bus

2.1.2. Modified EMC Scanning Probe. Figure 2.9 shows the details of the modified EMI scanning probe. An orientation sensor as well as a rotary encoder is attached. A CHR-6dm board is used as an orientation sensor to provide real time yaw, pitch, and roll angles at up to 300 Hz [15]. A rotary encoder is attached with the EMI scanning probe axially to capture its axial rotation.

While performing near field manual scanning, the user will move the probe to the point of interest. This will change the length of the wires. The change in the length of each wire is recorded by the rotary encoder. A controller area network (CAN) bus [16]

interface to the rotary encoder is used to retrieve the length information. With the length of each wire known, the position of the joint point (x_0, y_0, z_0) can be determined through triangulation [17]. Next, the user will orientate the probe and also rotate the probe axially until maximum field strength is observed.

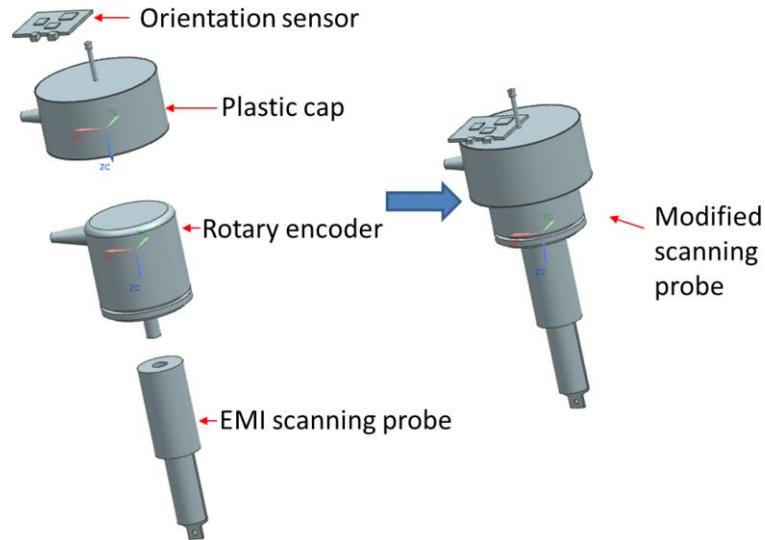


Figure 2.9. Modified EMI scanning probe

2.1.3. Determination of the Position of the Probe Tail. The tail of the probe is determined through triangulation method. With three distances known, the meet points of the three distances are two possible points. The solution is the one which is lower than the plane formed by three draw wire sensors.

As shown by Fig. 2.10, a global coordinate system is constructed. The yellow arrow denotes the location of the origin of the global coordinate system. With the wire length from the three draw wire sensors known, which are denoted as d_1 , d_2 , and d_3 . The equations for calculating the location of the probe tail, $(x \ y \ z)$ is shown below.

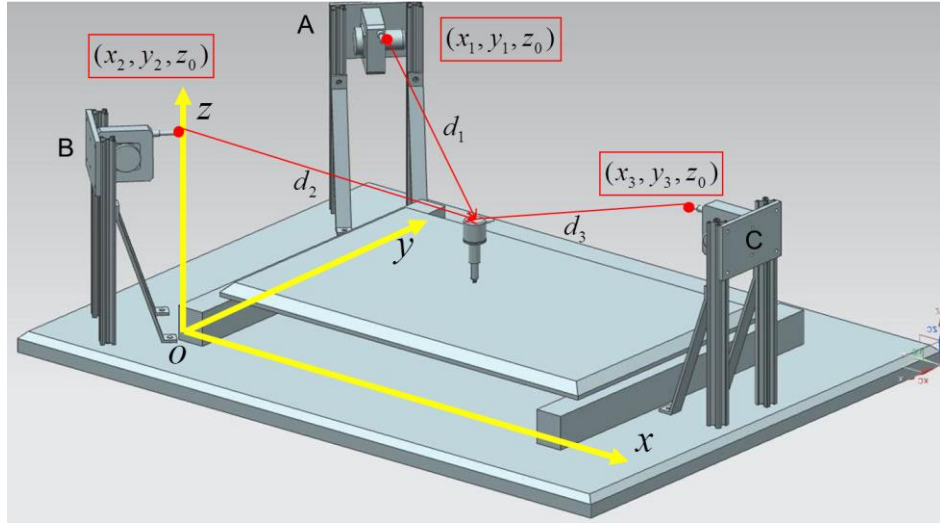


Figure 2.10. Coordinate system for determining the position of the probe tail

$$(x - x_1)^2 + (y - y_1)^2 + (z - z_0)^2 = d_1^2 \quad (1)$$

$$(x - x_2)^2 + (y - y_2)^2 + (z - z_0)^2 = d_2^2 \quad (2)$$

$$(x - x_3)^2 + (y - y_3)^2 + (z - z_0)^2 = d_3^2 \quad (3)$$

The final solution of the location of the probe tail is below:

$$\begin{bmatrix} x \\ y \end{bmatrix} = \begin{bmatrix} 2(x_2 - x_1) & 2(y_2 - y_1) \\ 2(x_3 - x_2) & 2(y_3 - y_2) \end{bmatrix}^{-1} \begin{bmatrix} d_1^2 - d_2^2 + x_2^2 - x_1^2 + y_2^2 - y_1^2 \\ d_2^2 - d_3^2 + x_3^2 - x_2^2 + y_3^2 - y_2^2 \end{bmatrix} \quad (4)$$

$$z = z_0 - \sqrt{d_1^2 - (x - x_1)^2 - (y - y_1)^2} \quad (5)$$

As discussed above, the x, y values are unique. However, there are two possibilities of z values. The one below the plane defined by the three points where draw wire sensors are located is the right solution.

2.1.4. Determination of the Position of the Probe Tip. With the position of the probe tail calculated, the next step is to determine the location of the probe tip (Fig. 2.11). An orientation sensor is used for determine the location of the tip of the probe.

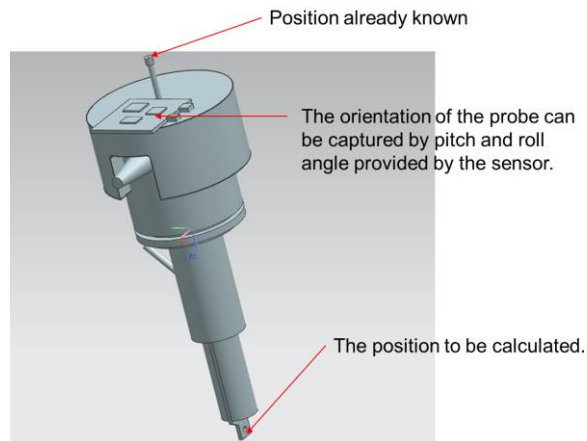
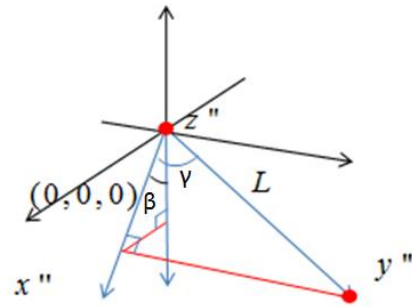


Figure 2.11. Orientation sensor used for calculating the location of the probe tip

A local coordinate system centered at the tail of the probe is constructed (fig. 2.12). In below figure, L is the length of the modified EMI scanning probe, β is pitch and γ is roll. Both of these angles are provided by the orientation sensor in real time. Figure 2.13 shows the orientation of the pitch and roll angle provided by the orientation sensor.



(x'', y'', z'') ?

Figure 2.12. Coordinate system for calculating the position of the probe tip

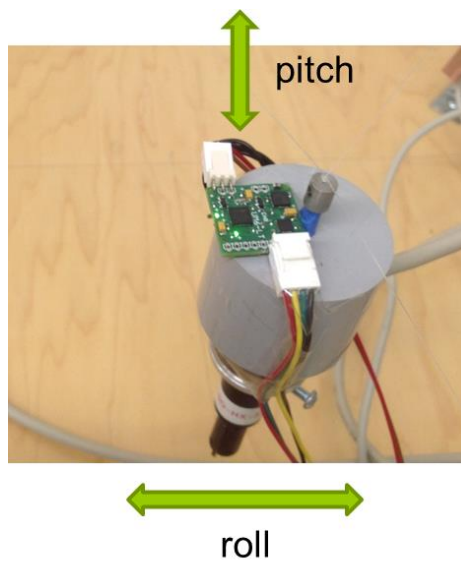


Figure 2.13. Convention of the pitch and roll orientation

Euler angles are provided by the orientation sensor in “yaw (α), pitch (β) and roll (γ)” order. The position of the probe tip is determined through homogenous coordinate transformation [18], as shown by eqn. (6).

$$\begin{bmatrix} x \\ y \\ z \\ 1 \end{bmatrix} = \begin{bmatrix} \cos(\alpha) & \sin(\alpha) & 0 & x_0 \\ -\sin(\alpha) & \cos(\alpha) & 0 & y_0 \\ 0 & 0 & 1 & z_0 \\ 0 & 0 & 0 & 1 \end{bmatrix} \begin{bmatrix} L \cos(\gamma) \sin(-\beta) \\ L \sin(\gamma) \\ -L \cos(\gamma) \cos(\gamma) \\ 1 \end{bmatrix} \quad (6)$$

Where L is the length of the modified probe, β and γ is pitch and roll from the orientation sensor. And x_0 y_0 z_0 is the coordinate of the probe tail.

2.1.5. Determination of the Orientation of the Probe . Figure 2.14 shows the geometric elements for determining the orientation of the probe.

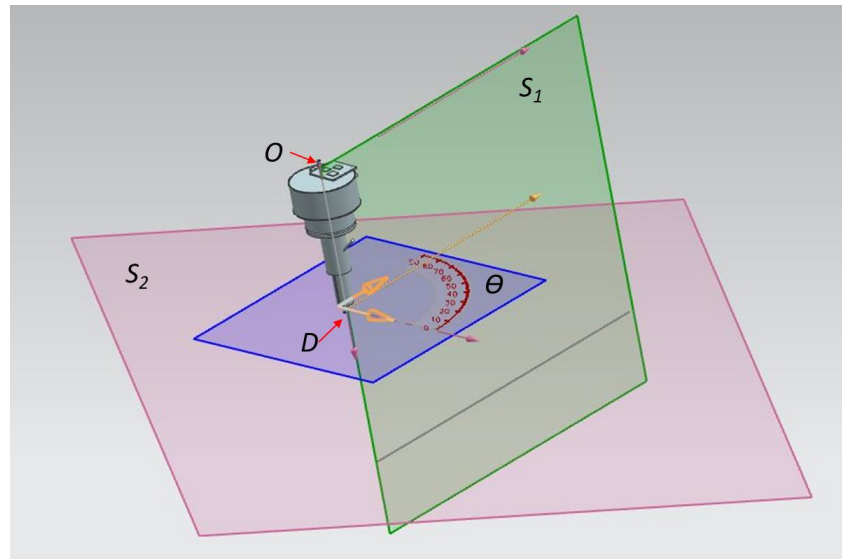


Figure 2.14. Geometric elements required to determine the orientation of the probe

Plane S1 is the surface formed by the wire from draw wire sensor standing along on one side of the table and the axis of the probe; plane S2 is the reference plane (table). The joint point of the three wires is denoted as $O = [x_0, y_0, z_0]$; the probe tip is denoted as $D = [x_d, y_d, z_d]$. The rotation axis is formed by O and D, and vector OD is denoted as $\langle u, v, w \rangle$ by normalizing vector $\langle x_d - x_0, y_d - y_0, z_d - z_0 \rangle$. θ is the angle from the rotary encoder attached to the probe. The rotation matrix for rotating about an arbitrary axis in 3D is formulated as $T_o^{-1}R_{xz}^{-1}R_z^{-1}R_z(\theta)R_zR_{xz}T_o$. Here T_o is matrix to translate point O to the origin.

$$T_o = \begin{bmatrix} 1 & 0 & 0 & -x_o \\ 0 & 1 & 0 & -y_o \\ 0 & 0 & 1 & -z_o \\ 0 & 0 & 0 & 1 \end{bmatrix} \quad (7)$$

R_{xz} is the rotation matrix to rotate the vector OD about the z-axis to the xz – plane.

$$R_{xz} = \begin{bmatrix} u / \sqrt{u^2 + v^2} & v / \sqrt{u^2 + v^2} & 0 & 0 \\ -v / \sqrt{u^2 + v^2} & u / \sqrt{u^2 + v^2} & 0 & 0 \\ 0 & 0 & 1 & 0 \\ 0 & 0 & 0 & 1 \end{bmatrix} \quad (8)$$

R_z is the rotation matrix to rotate the vector OD about the y-axis in the xz-plane to the z-axis.

T_o^{-1} , R_{xz}^{-1} and R_z^{-1} are the inverse of matrix, T_o , R_{xz} and R_z respectively. With the obtained rotation matrix, the orientation of the probe can be determined.

$$R_z = \begin{bmatrix} w / \sqrt{u^2 + v^2 + w^2} & 0 & -\sqrt{u^2 + v^2} / \sqrt{u^2 + v^2 + w^2} & 0 \\ 0 & 1 & 0 & 0 \\ \sqrt{u^2 + v^2} / \sqrt{u^2 + v^2 + w^2} & 0 & w / \sqrt{u^2 + v^2 + w^2} & 0 \\ 0 & 0 & 0 & 1 \end{bmatrix}$$

(9)

2.1.6. Accuracy Test of the System. Repeatability test was conducted to check how accurate the system is in determining probe location. The system repeatability is tested with two scenarios. The first scenario is holding the probe vertical, and dragging it to the same point for several times, and check the software readings of the different runs. Table 2.2 shows the results of the repeatability test in the first scenario. The second scenario is to hold the probe at some angles, but ensure the probe tip reach the same point for different runs. The probe orientation for different runs is not necessarily the same. Table 2.3 shows the test results.

Compare the results of the repeatability test of the two scenarios, it can be seen that, when the value of the orientation sensor is utilized for calculating the probe tip location (scenario 2), the repeatability of the probe tip is decreased to a larger degree. The main reason for causing the decreased reparability is due to the repeatability of the orientation values provided by the orientation sensor. The orientation sensor's repeatability is 2 to 3 degrees, in roll and pitch, and 5 degrees in yaw, which is pretty much a catastrophe for the probe tip positioning accuracy of this system.

Table 2.2. Hold the probe vertical on the table (Units: mm)

| | Run 1 | | | run 2 | | | run 3 | | |
|------------|-------|-----|-----|-------|-----|-----|-------|-----|------|
| | x | y | z | x | y | z | x | y | z |
| Probe tail | 439 | 281 | 164 | 439 | 280 | 164 | 439 | 280 | 164 |
| Probe tip | 436 | 274 | 0.4 | 436 | 274 | 0.5 | 436 | 274 | 0.50 |

Table 2.3. Drag the probe to the same point on the table (Units: mm)

| | Run 1 | | | run 2 | | | run 3 | | |
|------------|-------|-----|-----|-------|-----|-----|-------|-----|-----|
| | x | y | z | x | y | z | x | y | z |
| Probe tail | 432 | 341 | 152 | 424 | 326 | 157 | 423 | 325 | 157 |
| Probe tip | 435 | 275 | 2 | 438 | 275 | 1.6 | 438 | 275 | 1.7 |

By purely measurements repeatability test, it is determined that the positioning accuracy if the system is in centimeter range, which largely restricted the frequency range this system can apply to. There are many error sources causing this large repeatability test results. Many of these sources are non-systematic, so it is not possible to compensate those random errors. Table 2.4 summarized the error sources of this system.

Table 2.4. Error sources of the system

| Error categories | Items |
|-------------------|------------------------------------------------------------------|
| System error | Non-flat table |
| | Non-vertical rods |
| | Hysteresis of the draw wire sensors |
| | Inaccuracy of the orientation sensor |
| Measurement error | The height of the sensors |
| | The length of the integrated probe |
| | Poor repeatability of human when lead the probe to the same spot |

From the repeatability test, it can be seen that the system positioning accuracy is in sub centimeter range. So the application frequency of the system is below GHz. Besides application frequency, other characteristics of the system also prevent it to be further developed, the cons of this system is summarized below:

- The value of manual scanning with position recording concept has been validated by this system.
- The positioning accuracy of the system is largely restricted by the precision of the orientation sensor.
- Even scanning in a short period, fairly amount of fatigue will be introduced due to the force from the three draw wire sensors.

Due to the above characteristics of the system, another structure, which is based on the CMM arm concept is developed and described in detail below.

2.2. CMM ARM BASED POSITION DETERMINATION SYSTEM

An eight axis portable coordinate measurement machine (CMM) arm was prototyped, illustrated by Fig. 2.15. The axis of the arm is made of aluminum tube. The types of linkage include hinge joints, pivot joints, and a sliding joint. Slew bearing is used for the main pivot linkage. The probe is attached to the end axes through a pivot joint. The rotation angle of the hinge joints and pivot joints are recorded by precision potentiometers. The base of the arm connects the camera slider through a sliding joint, which allows enlarging the coverage space of the CMM arm. A draw wire sensor is used to measure the linear displacement of the arm base on the camera slider.

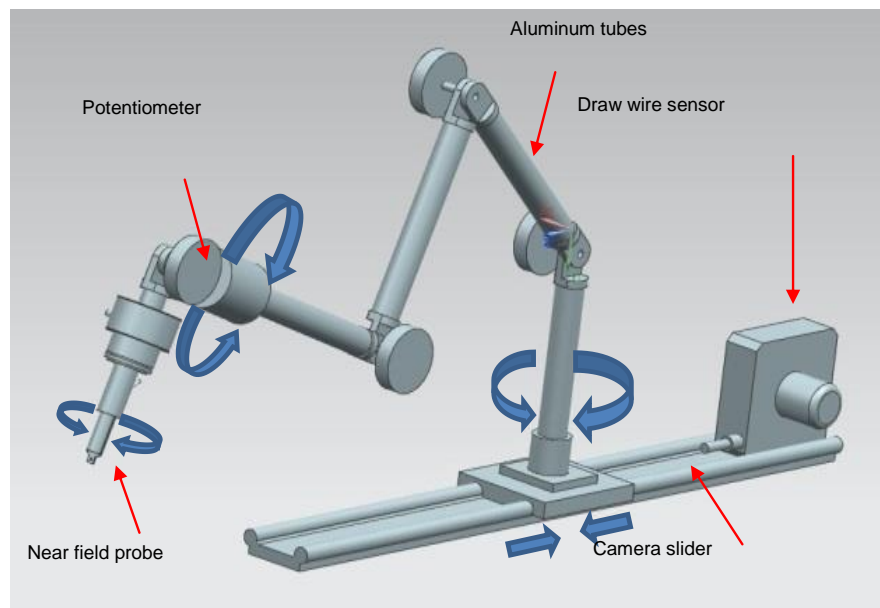


Figure 2.15. Mechanical design for the probe recording system

2.2.1. Mechanical Design and Assembly. As shown in Fig. 2 16, the mechanical system of the probe recording system is a CMM arm structure. Eight axes are included to make sure the arm covers a large 3-D space. The axis of the CMM arm is made of aluminum tube. The types of linkage include hinge joints, pivot joints, and a sliding joint. Slew bearing is used for the main pivot linkage. The probe is attached to the end axes through a pivot joint. The rotation angle of the hinge joints and pivot joints are recorded through a pivot joint. The rotation angle of the hinge joints and pivot joints are recorded by precision potentiometers. The base of the CMM arm connects the camera slider through a sliding joint. Sliding joint allows enlarging the coverage space of the CMM arm. A draw wire sensor is used to measure the linear displacement of the CMM arm base on the camera slider.

2.2.2. Sensors Used for this Structure. The draw wire sensor provides a linear resolution of 49 μ m and allows the CMM arm base to move up to 1m. There are seven potentiometers connected in parallel with a DC source of 10 V to measure the angles.

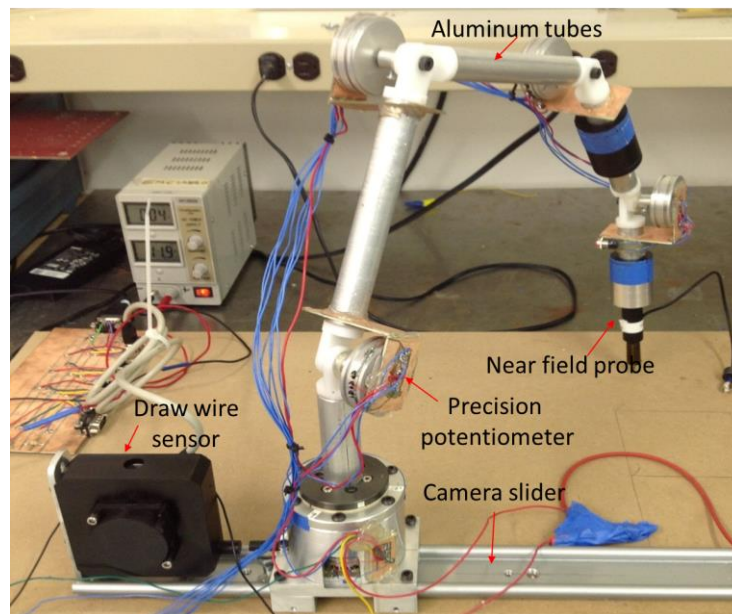


Figure 2.16. CMM arm based system

The voltage reading from the single turn precision potentiometers are recorded on the PC using A/D converters. Due to limited mechanical speed, low sampling rate A/D converters can be utilized. The placement and wiring for the precision potentiometer in hinge joint is shown in Fig. 2.17.

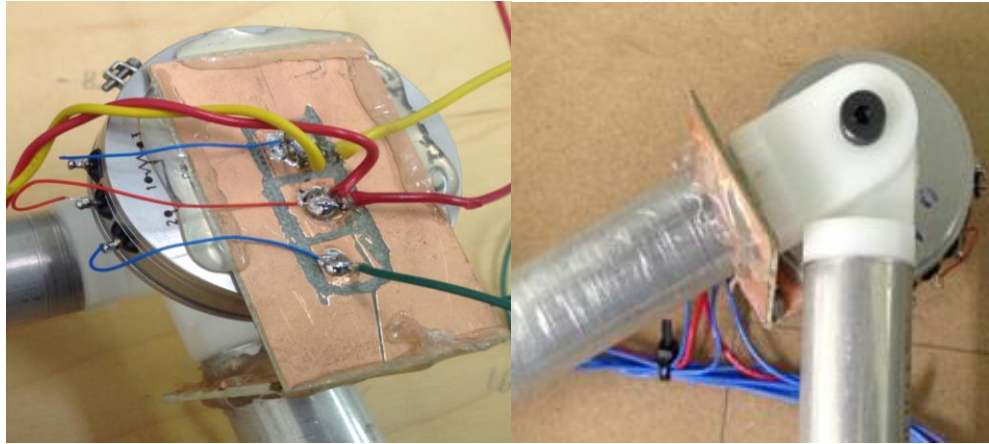


Figure 2.17. Hinge joint

For the pivot joint, a smaller potentiometer is used for capturing the angle of the joint. Figure 2.18 shows the pivot joint, and the placement of the small potentiometer by CAD model.

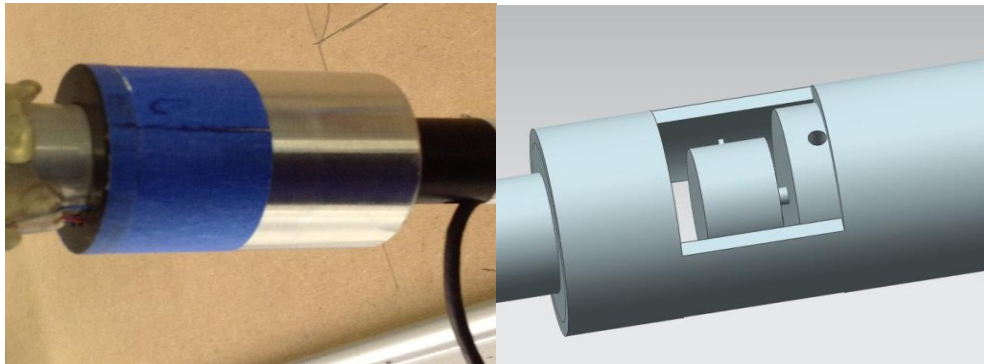


Figure 2.18. Pivot joint

2.2.3. Circuit Schematics for Angle Recording. Figure 2.19 illustrates the principle of how the angle of the joints were recorded by potentiometers. As mentioned earlier, a 10V DC source was connected with the all the potentiometers, which were connected in parallel with each other.

The source voltage and voltage between 2 and 3 measured through a data acquisition device. By utilizing the linearity relationship between the angle, resistance and the voltage, the angle of the joint can be calculated. Equation 10 shows the relationships.

$$\frac{\alpha_2}{\alpha_{tot}} = \frac{R_2}{R_{tot}} = \frac{V_{23}}{V_1} \quad (10)$$

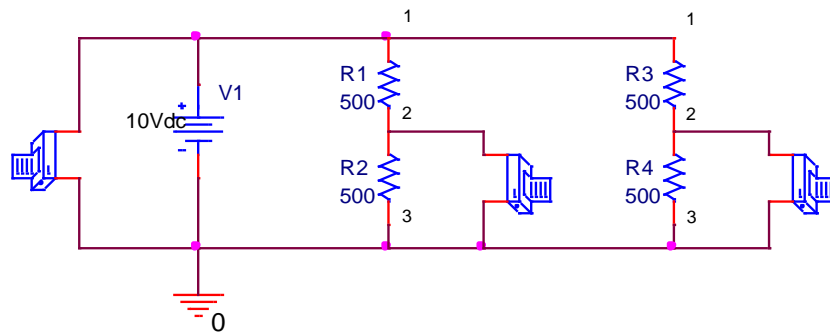


Figure 2.19. Circuit diagram for angle recording

2.2.4. Calibrating the Angle at the Local Joints. In order to interpret the voltage values read by the data acquisition device, and translate it into angle values, angle calibration was a prerequisite. Figure 2.20 shows that, for hinge joint, the two extreme values of the angles are -120 and 120 degrees, respectively. Another calibrating angle is 0 degree. For pivot joint, markers were made to indicate 0, -120, and 120 degrees.

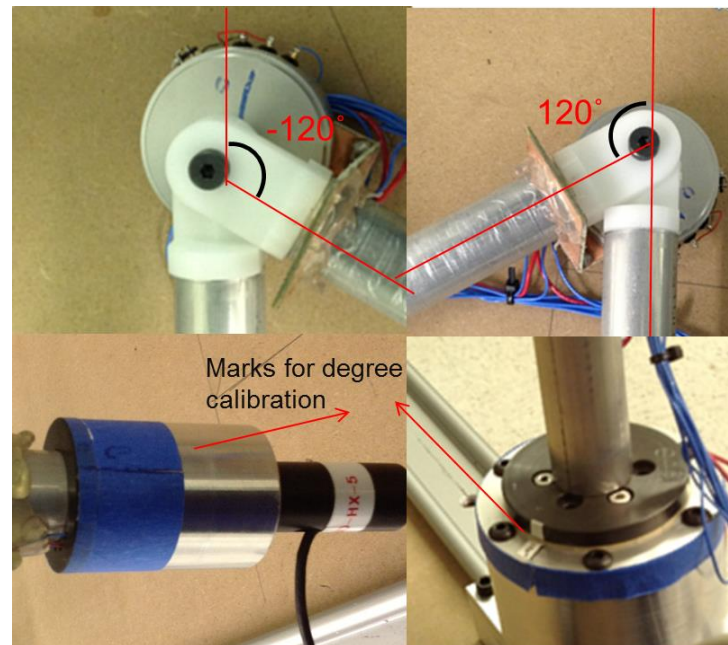


Figure 2.20. Angle calibration

Figure 2.21 shows the angle calibration schematic. Since the assumption is that the potentiometer is linear. For linear representation between the voltage value and the angle value, two unknowns were needed to determine through angle determination. Theoretically, two angles are sufficient for calibration. However, due to the small amount of non linearity of the potentiometer, instead, three angles were calibrated. And Interpolating was used to determine the angles between the three calibrated angle. They are -120, 0, and 120 degrees.

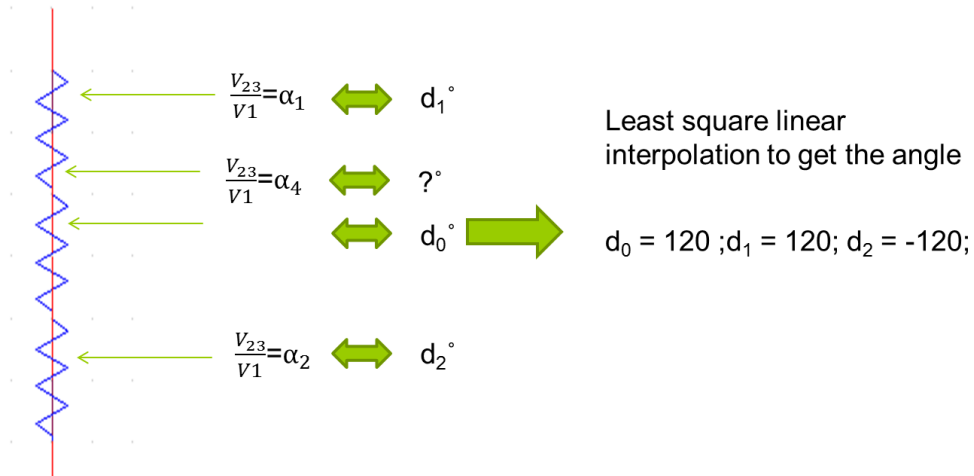


Figure 2.21. Schematic for angle calibration

2.2.5. Mechanical Calculation . In order to calculate the position of the tip of the probe and the orientation of the probe, a global coordinate system is setup as shown in Fig. 2.22. The x-axis is aligned with the slider, the z-axis is perpendicular to the base plane, and the y-axis is formed through right handed rule. Local coordinate systems for each joint are setup by the following rules,

- Z-axis always align with the tube
- Y-axis always perpendicular to the plane formed by two tubes with an angle to each other
- X-axis can be determined through right handed rule

Homogenous coordinate system transformation method [18] is utilized to transform the coordinate of points from one coordinate to another. After determining the homogenous transformation matrices of all the movable links, they are multiplied successively from the tip of the probe to the reference coordinate system, resulting in the actual probe tip position with respect to the globe coordinate system. For a linear translation, the transformation matrix can be formulated as $T_x^{(y)}$, where x denotes the

direction of translation, and y denotes the amount to be translated. A point is formulated using a vector notation $P^n = [x_n \ y_n \ z_n \ 1]^T$, with the 1 as a weighting factor, representing the coordinate of point P in coordinate system n. For example, the origin of coordinate system 0 is located at $[0 \ 0 \ l_1 \ 1]^T$ of coordinate system 1. To translate points in coordinate system 0 to coordinate system 1, $T_z(l_1)$ need to be applied. To determine P^1 from P^0 , the transformation matrix is left multiplied as shown in eqn. (11).

$$P^1 = T_z(l_1)P^0 = \begin{bmatrix} 1 & 0 & 0 & 0 \\ 0 & 1 & 0 & 0 \\ 0 & 0 & 1 & l_1 \\ 0 & 0 & 0 & 1 \end{bmatrix} P^0 \quad (11)$$

For rotation transformation, the matrix can be formulated as $R_x(y)$, where x denotes the axis to rotate around, and y denotes the angle to rotate. If we want to rotate P^0 in coordinate system 0 around z-axis by angle β_1 , the transformation is formulated as shown by eqn. (12).

$$P^1 = R_z(\beta_1)P^0 = \begin{bmatrix} \cos(\beta_1) & -\sin(\beta_1) & 0 & 0 \\ \sin(\beta_1) & \cos(\beta_1) & 0 & 0 \\ 0 & 0 & 1 & 0 \\ 0 & 0 & 0 & 1 \end{bmatrix} P^0 \quad (12)$$

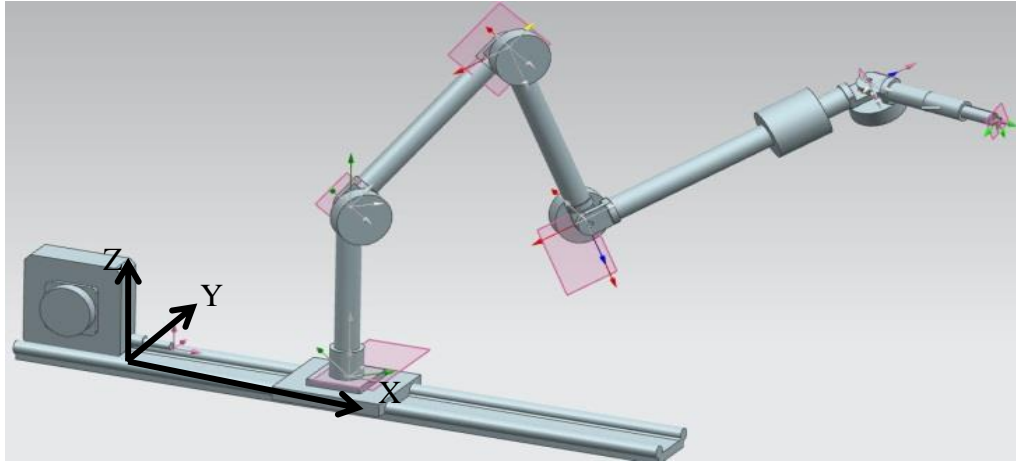


Figure 2.22. CMM structure with probe attached to the end axes

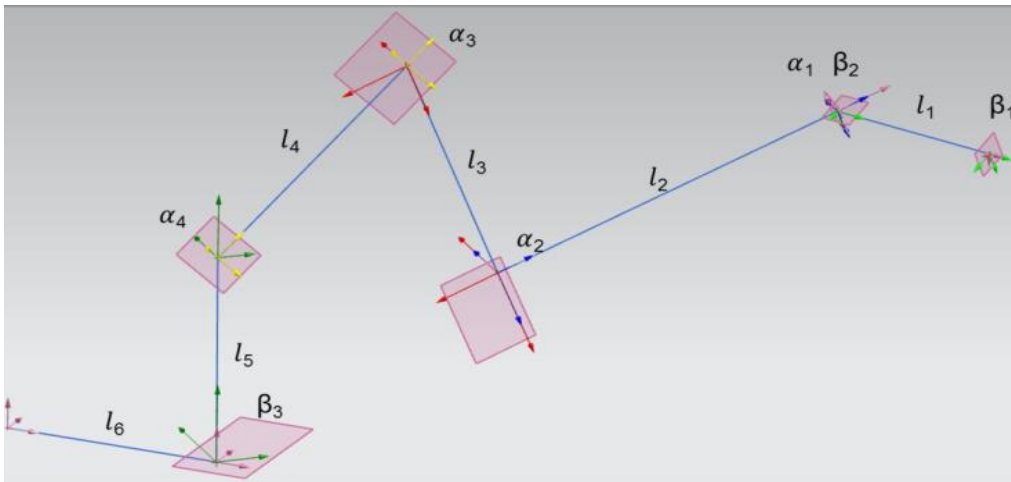


Figure 2.23. Input for calculating the position of tip of the probe

As shown in Fig. 2.23, rotation angle for a hinge joint is denoted as α , rotation angle for a pivot joint is denoted as β and the distance for a sliding joint is denoted as l . If we are trying to find out point $P^0 = [0 \ 0 \ 0 \ 1]^T$ in the local coordinate system at the tip of the probe, there are overall thirteen transformations involved. The complete equation

for denoting point P^0 in the global coordinate system can be derived by using equation (11), (12).

$$P^{13} = T_x(l_6)R_z(\beta_3)T_z(l_5)R_y(\alpha_4)T_z(l_4)R_y(\alpha_3)T_z(l_3)R_y(\alpha_2)T_z(l_2)R_z(\beta_2)R_y(\alpha_1)T_z(l_1)R_z(\beta_1)P^0 \quad (13)$$

$$P^{13} = T_x P^{12} = \begin{bmatrix} 1 & 0 & 0 & l6 \\ 0 & 1 & 0 & 0 \\ 0 & 0 & 1 & 0 \\ 0 & 0 & 0 & 1 \end{bmatrix} \begin{bmatrix} \cos(\beta_3) & -\sin(\beta_3) & 0 & 0 \\ \sin(\beta_3) & \cos(\beta_3) & 0 & 0 \\ 0 & 0 & 1 & 0 \\ 0 & 0 & 0 & 1 \end{bmatrix} \begin{bmatrix} 1 & 0 & 0 & 0 \\ 0 & 1 & 0 & 0 \\ 0 & 0 & 1 & l5 \\ 0 & 0 & 0 & 1 \end{bmatrix} \begin{bmatrix} \cos(\alpha_4) & 0 & \sin(\alpha_4) & 0 \\ 0 & 1 & 0 & 0 \\ -\sin(\alpha_4) & 0 & \cos(\alpha_4) & 0 \\ 0 & 0 & 0 & 1 \end{bmatrix} \begin{bmatrix} 1 & 0 & 0 & 0 \\ 0 & 1 & 0 & 0 \\ 0 & 0 & 1 & l4 \\ 0 & 0 & 0 & 1 \end{bmatrix} \begin{bmatrix} \cos(\alpha_3) & 0 & \sin(\alpha_3) & 0 \\ 0 & 1 & 0 & 0 \\ -\sin(\alpha_3) & 0 & \cos(\alpha_3) & 0 \\ 0 & 0 & 0 & 1 \end{bmatrix} \begin{bmatrix} 1 & 0 & 0 & 0 \\ 0 & 1 & 0 & 0 \\ 0 & 0 & 1 & l2 \\ 0 & 0 & 0 & 1 \end{bmatrix} \begin{bmatrix} \cos(\beta_2) & -\sin(\beta_2) & 0 & 0 \\ \sin(\beta_2) & \cos(\beta_2) & 0 & 0 \\ 0 & 0 & 1 & 0 \\ 0 & 0 & 0 & 1 \end{bmatrix} \begin{bmatrix} \cos(\alpha_1) & 0 & \sin(\alpha_1) & 0 \\ 0 & 1 & 0 & 0 \\ -\sin(\alpha_1) & 0 & \cos(\alpha_1) & 0 \\ 0 & 0 & 0 & 1 \end{bmatrix} \begin{bmatrix} 1 & 0 & 0 & 0 \\ 0 & 1 & 0 & 0 \\ 0 & 0 & 1 & l1 \\ 0 & 0 & 0 & 1 \end{bmatrix} \begin{bmatrix} \cos(\beta_1) & -\sin(\beta_1) & 0 & 0 \\ \sin(\beta_1) & \cos(\beta_1) & 0 & 0 \\ 0 & 0 & 1 & 0 \\ 0 & 0 & 0 & 1 \end{bmatrix} \begin{bmatrix} 0 \\ 1 \\ 0 \\ 1 \end{bmatrix} \quad (14)$$

The coordinate of another point $\tilde{P}^0 = [0 \ 1 \ 0 \ 1]^T$ in the local coordinate system at the tip of the probe is also determined through the same process. With the global coordinates of the two points P^0 and \tilde{P}^0 , the orientation of the probe can be determined.

2.2.6. System Accuracy Test. Tests were conducted to determine the system accuracy. Figure 2.24 shows the first test setup. The system was placed at a planar surface. With other joints/segments been kept still, the last joint, the pivot joint was turned axially. Theoretically the final probe tip position should not be changed. However, due to the non linearity of the potentiometer, the final calculated position has some variation. Table 2.7 shows the repeatability test results, the standard deviation of the coordinates of the probe tip is approximately 1 mm in x and y axis, and sub milimeter in z axis. In principle, with all the other segments fixed, the z axis should have no variation at all. However, the voltage values read by the data acquisition box of all the potentiometers were also changing from time to time. This lead to the small variation in z axis.

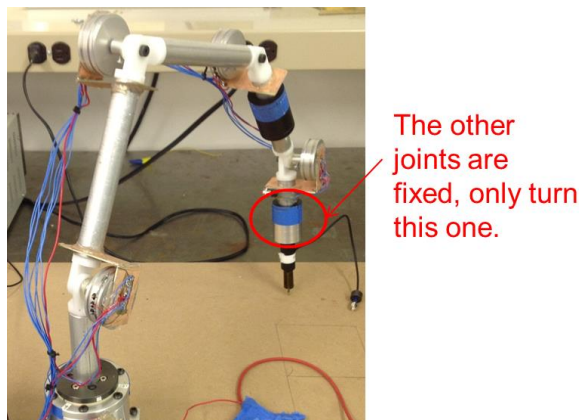


Figure 2.24. First repeatability test

Folowing is the table shows the first repeatability test result. In this table, only ten sets of data are shown. Actually, hundreds sets of data can be obtained in a short time. The bottlenect here is the data processing speed of the daq device. The standard deviation of each axis was calculated based on a larger data sample. The same fact apply to the following tests.

Table 2.7. First repeatability test (Unit: mm)

| Runs | x | y | z |
|-------|--------|--------|--------|
| 1 | 440.68 | 224.68 | -23.60 |
| 2 | 441.98 | 223.61 | -23.31 |
| 3 | 443.61 | 222.88 | -22.75 |
| 4 | 443.25 | 222.48 | -22.95 |
| 5 | 443.14 | 222.43 | -23.31 |
| 6 | 443.38 | 222.48 | -22.86 |
| 7 | 443.24 | 222.58 | -23.10 |
| 8 | 443.38 | 222.77 | -22.99 |
| 9 | 443.37 | 222.09 | -23.16 |
| 10 | 445.13 | 221.66 | -22.72 |
| stdev | 1.39 | 1.07 | 0.27 |

Repeatability test setup two is shown by Fig. 2.25. The same as the first test, except for the high lighted axial joint, all the other segments of the arm were kept in still.

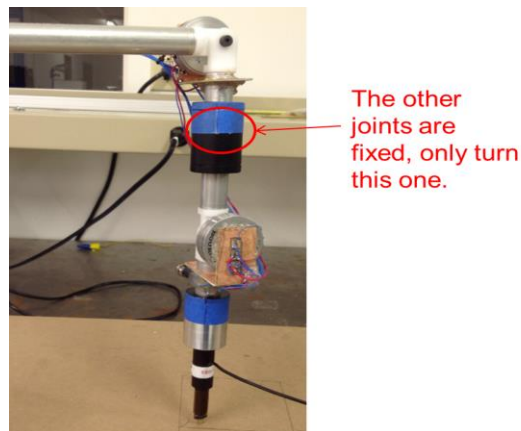


Figure 2.25. Repeatability test 2

The test results is shown by Table 2.8. The standard deviation of each axis for the second test is larger compared with the first test. The reason causing this is pretty random. The explanation would be due to the non rigidity of the CMM arm structure, while

turning the axis axially, it was not easy to maintain the other segments still. This was even more difficult compared with the first test.

Table 2.8. Repeatability test 2 (Unit: mm)

| | x | y | z |
|-------|--------|--------|--------|
| 1 | 355.39 | 144.08 | -25.54 |
| 2 | 351.37 | 139.96 | -26.99 |
| 3 | 349.87 | 139.03 | -27.24 |
| 4 | 349.89 | 139.45 | -26.65 |
| 5 | 348.20 | 141.53 | -26.85 |
| 6 | 349.16 | 141.83 | -26.58 |
| 7 | 349.59 | 141.98 | -27.18 |
| 8 | 351.11 | 142.77 | -26.67 |
| 9 | 350.89 | 143.84 | -27.19 |
| 10 | 350.15 | 145.71 | -27.27 |
| stdev | 2.14 | 3.22 | 0.81 |

The last repeatability test is to rotate all the hinge joints as indicated by Fig. 2.26. It would be expected that, with more potentiometers involved, the repeatability of the system would be even worse compared with the first two tests.

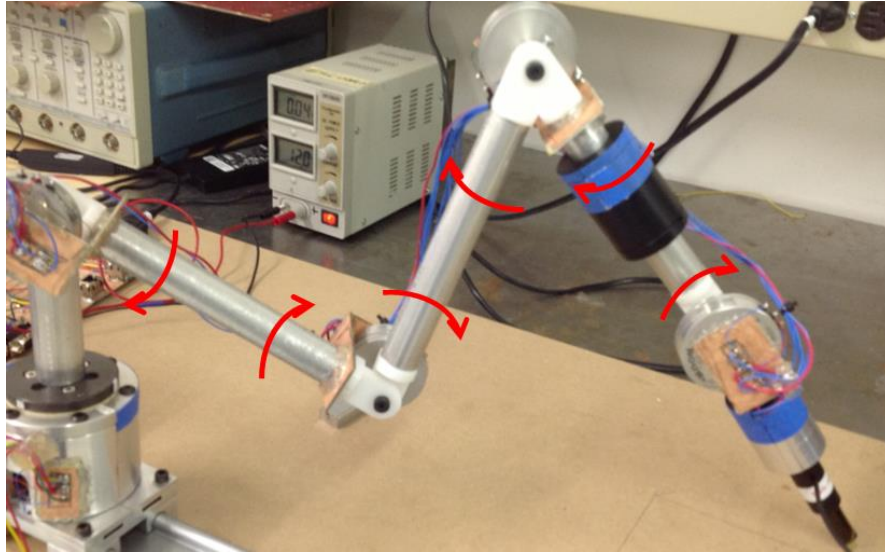


Figure 2.26. Repeatability test 3

Table 2.9 shows the test results.

Table 2.9. Repeatability test 3 (Unit: mm)

| | x | y | z |
|-------|--------|--------|--------|
| 1 | 462.62 | 244.21 | -21.50 |
| 2 | 463.55 | 245.89 | -23.59 |
| 3 | 465.31 | 244.10 | -24.20 |
| 4 | 461.73 | 243.35 | -27.74 |
| 5 | 460.06 | 245.86 | -28.09 |
| 6 | 456.82 | 247.15 | -30.55 |
| 7 | 467.52 | 241.03 | -20.19 |
| 8 | 465.56 | 239.37 | -20.31 |
| 9 | 464.76 | 239.25 | -19.96 |
| 10 | 464.58 | 239.47 | -21.43 |
| stdev | 2.22 | 2.89 | 2.72 |

Figure 2.27 shows that the system is recording positions and indicated by the blue markers placed on the table.

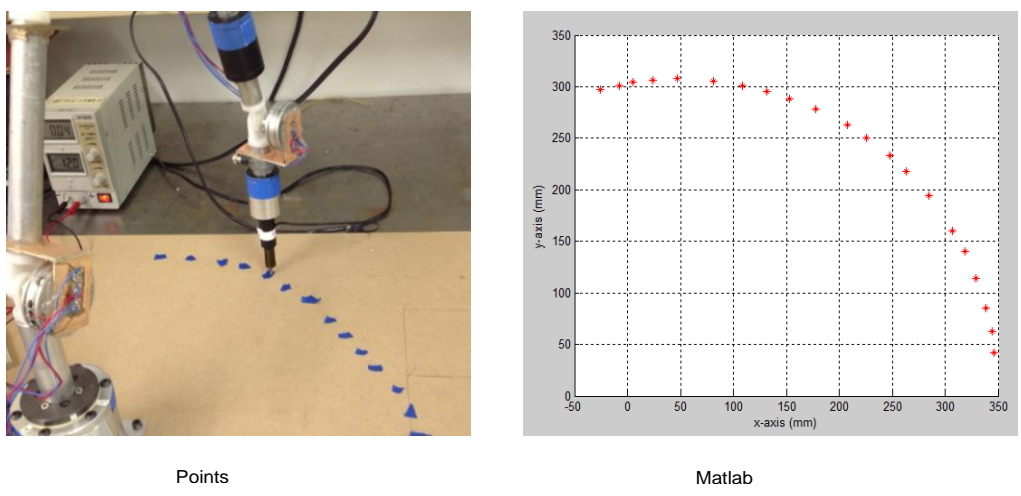


Figure 2.27. Points collection test setup

This system can be used for EMI scanning especially for system with complicated cable routing and surface topology. Figure 2.28 shows the system is used for scanning a TLP system. The TLP has a board with many components on it, and inside the TLP, there were many cables.



Figure 2.28. CMM arm based system

For this CMM arm based system, many degrees of freedom are needed to cover relative large area and to measure complex shapes, thus causing more aggregated positioning errors. The accumulated position error would largely affect the accuracy of the near field measurement and visualization. So another system was developed. Optical tracking based system for EMI scanning was developed and is introduced in the following section.

2.3. OPTICAL TRACKING BASED SYSTEM

Optical systems use data captured from image sensors to triangulate the 3D position of a subject between one or more cameras calibrated to provide overlapping projections. Data acquisition is traditionally implemented using special markers attached to an object; Optical tracking produce data with three degrees of freedom for each marker, and rotational information must be inferred from the relative orientation of three or more markers; the object whose position shall be tracked is equipped with markers. Markers can be light reflectors or light emitters. To also measure the orientation of a body, several (equal or more than three) of these markers have to be arranged at a known geometry.

Tracking cameras scan a certain volume and detect the light that comes from the markers. Their images are processed to identify and calculate potential marker positions. These image data are combined to calculate positions of single markers or positions and orientation of rigid arrangements of several markers.

The result of each measurement are coordinates that describe the position of the markers, and hence the position and orientation of the body carrying the markers.

Figure 2.29 shows the devices used in the system. Four flex 13 cameras from Optitrack [19] are utilized for tracking, a synchronization unit is applied to coordinate the digital videos obtained from each camera, and the calibration square and calibration wand are used for system calibration.



Figure 2.29. Optical tracking hardware

The hardware connection configuration of the developed system is shown by Fig. 2.30. A typical optical tracking system is comprised of four to eight cameras, one synchronization unit, a PC running the tracking software and several rigid body targets attached to various interaction devices. For the near field scanning application, the rigid body target is attached to a near field probe, which was used to measure the near field strength of the device under test (DUT). To visualize the local fields, the EMC engineer moves the probes to points of interest while measuring near field strength. Concurrently, a spectrum analyzer will record the magnetic field as the probe tracking system records the probe's position and orientation associated with each scanning point. Through 3D interpolation, a near field strength indicated by color will be created with the shape of the map mimic the actual DUT. In this way, complex structures can be scanned efficiently.

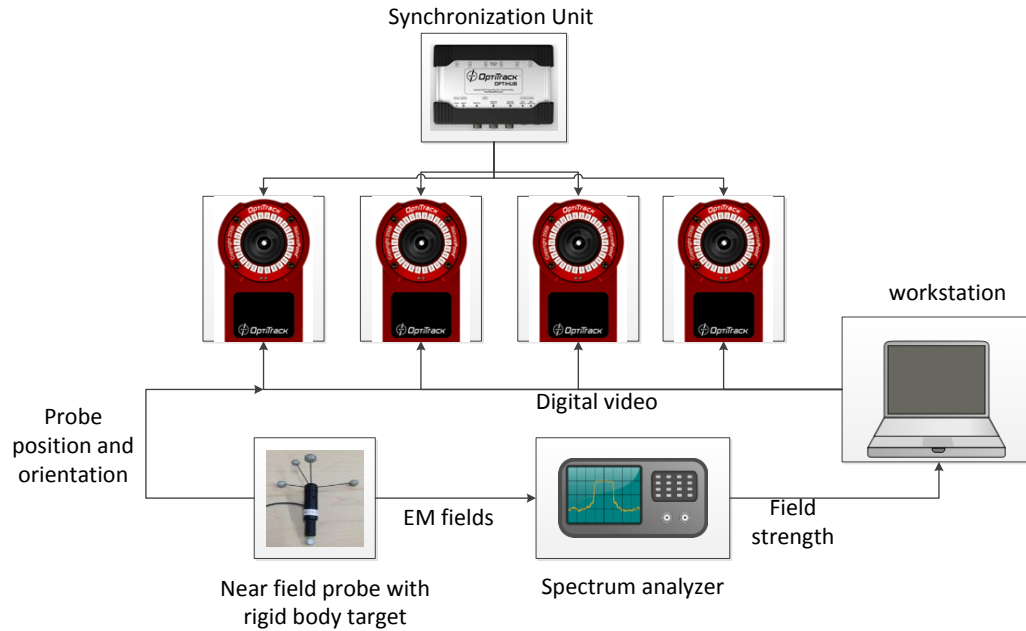


Figure 2.30. Configuration of the CMM arm based system

2.3.1. Modified EMI Scanning Probe. Probe with markers allow tracking, provided that the markers are at least within the sight of two cameras. EMI scanning probes are adapted with markers attached to the upper portion of the probe. Four pieces of markers are affixed to the probe, to record the position and orientation of it. Figure 2.31 shows rigid body targets used to track an object. Figure 2.32 shows an adapted EMI scanning probe.

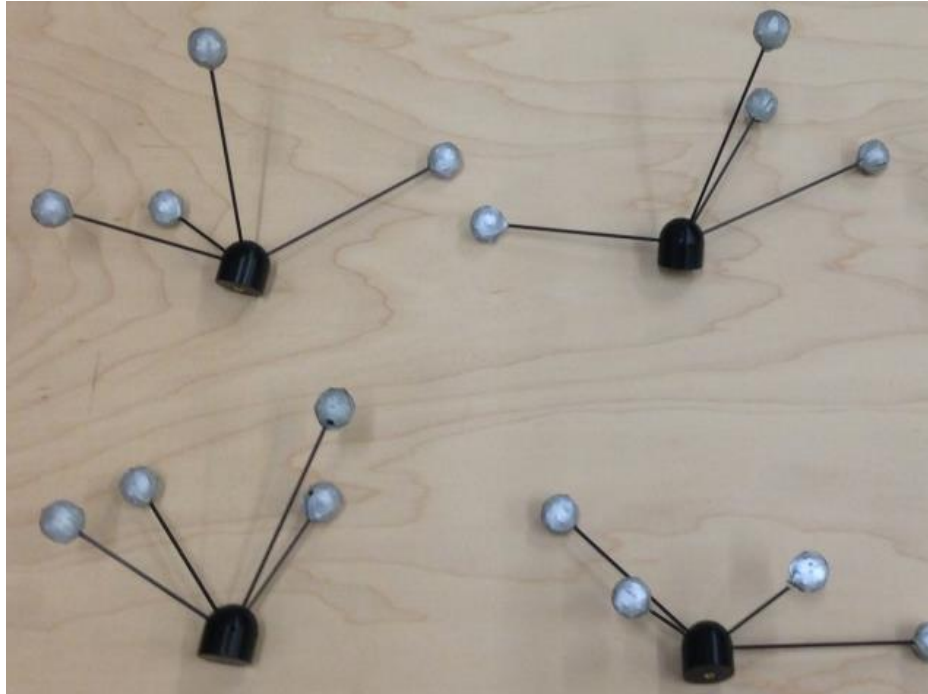


Figure 2.31. Rigid body target for object tracking from Iotracker [20]



Figure 2.32. Modified EMI probe for position and orientation tracking

By setting up the physical optical tracking hardware and calibrating the optical tracking system appropriately, a probe tracking based EMI manual scanning system is prepared. In order to allow the position of the probe tip and orientation of the probe to be tracked accurately, the probe avatar in the probe tracking software need to be setup correctly. Appendix shows how to connect the optical tracking hardware, calibrate the tracking system, and finally, how to build a probe avatar in the tracking software in detail. Figure 2.33 is the avatar of the optically tracked probe in the tracking software. Position and orientation of the probe are displayed by the software in real time.

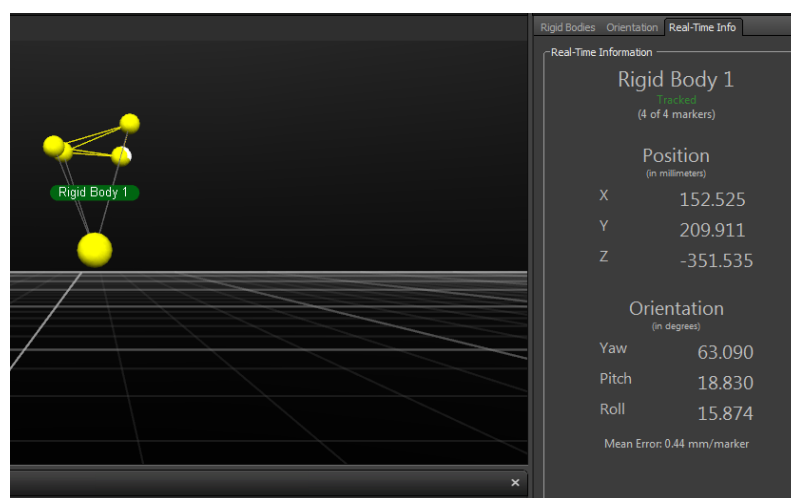


Figure 2.33. A probe tracked and modeled in optical tracking software

2.3.2. Positioning Accuracy of the System. The accuracy of the system is evaluated by wandng two markers with fixed distance between each other within the covered space. The distance between the two markers is 0.5 meters precisely. More than 3000 instances of data points are collected in a short time. The samples are shown in Table 2.10, from which we can see that the positing accuracy of the system is within sub millimeter range.

Table 2.10. Positioning accuracy repeatability test sample data (Unit: m)

| marker 1 | | | marker 2 | | | Distance |
|----------|--------|---------|----------|--------|---------|----------|
| x | y | z | x | y | z | |
| 0.1361 | 0.1860 | -0.4560 | 0.5728 | 0.2493 | -0.2199 | 0.5004 |
| 0.1364 | 0.1865 | -0.4559 | 0.5729 | 0.2492 | -0.2197 | 0.5003 |
| 0.1367 | 0.1868 | -0.4559 | 0.5732 | 0.2491 | -0.2195 | 0.5003 |
| 0.1371 | 0.1872 | -0.4557 | 0.5735 | 0.2489 | -0.2190 | 0.5003 |

2.3.3. Orientation of the Probe. For measurements with orientation of the probe required, the Euler angles provided by the tracking software are illustrated by Fig. 2.34. Yaw is the angle rotated around Y axis, pitch is the angle rotated around Z axis, and the roll is the angle rotated around X axis. A default state can be setup by the software, when Yaw pitch and roll angle are all zeros, which depends on how users interpret the orientation of the probe. Here the orientation of the probe means the direct cosine of the normal of the PCB surface on the probe.

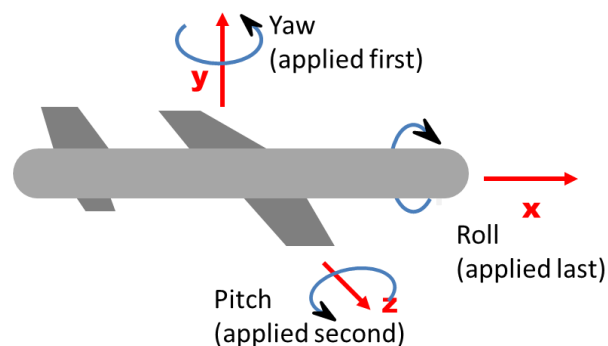


Figure 2.34. Euler angles provided by the tracking software

2.3.4. Optical Tracking System Setup and System Calibration. Before setting up the system, ensure the following software is installed:

- NI-DAQmx 9.0.2
- NI-488.2 3.1.1
- NI-VISA 5.3 - Real-Time OS
- Optitrack Motive

Figure 2.35 shows the hardware connection scheme. Four flex 13 cameras are connected and synchronized by Optihub. The video images are sent to the Motive software for processing to stream out the position and orientation of the tracked object. A near field measuring device, a spectrum analyzer is connected to the PC via GPIB cable, with the near field strength measured by a near field probe. The near field probe is adapted with four markers attached to it. In order to ensure start and stop scanning in the middle of a scanning process, a switch is implemented; a detailed connection scheme will be shown later.

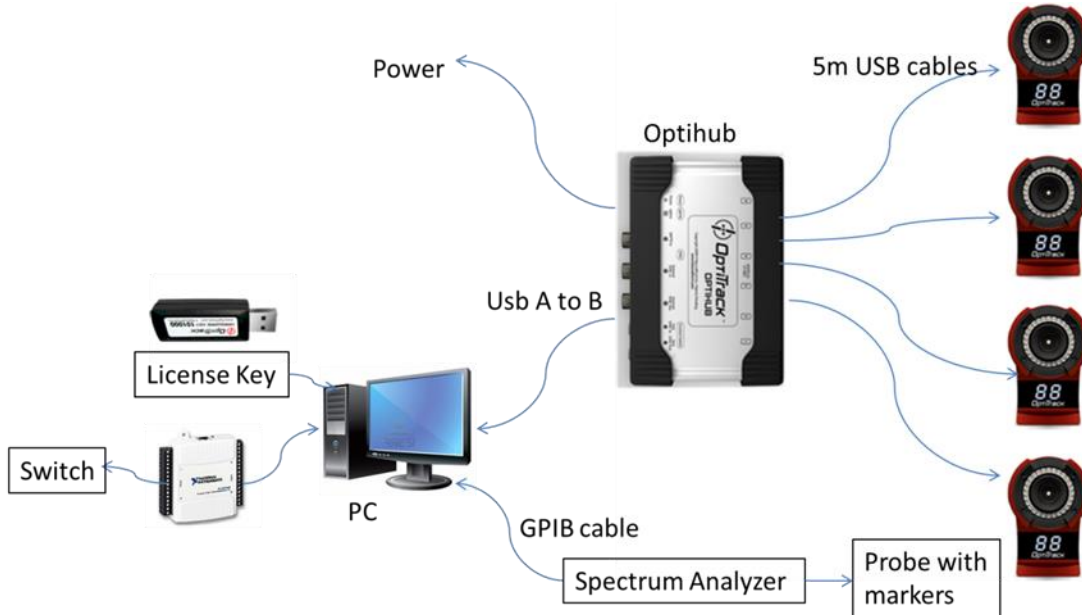


Figure 2.35. Hardware connection scheme

As shown by Fig. 2.36, a NI-DAQ is utilized and connected with a simple switch for pausing scanning. The switch is connected with DAQ digital channel (P0.0 and GND).



Figure 2.36. A switch implemented through DAQ for pausing scanning

Firstly, the hardware key provided with the optical tracking software needs to be inserted into a USB port to start the software. Then, open the program Motive. Figure 2.37 shows the interface after the program is started.

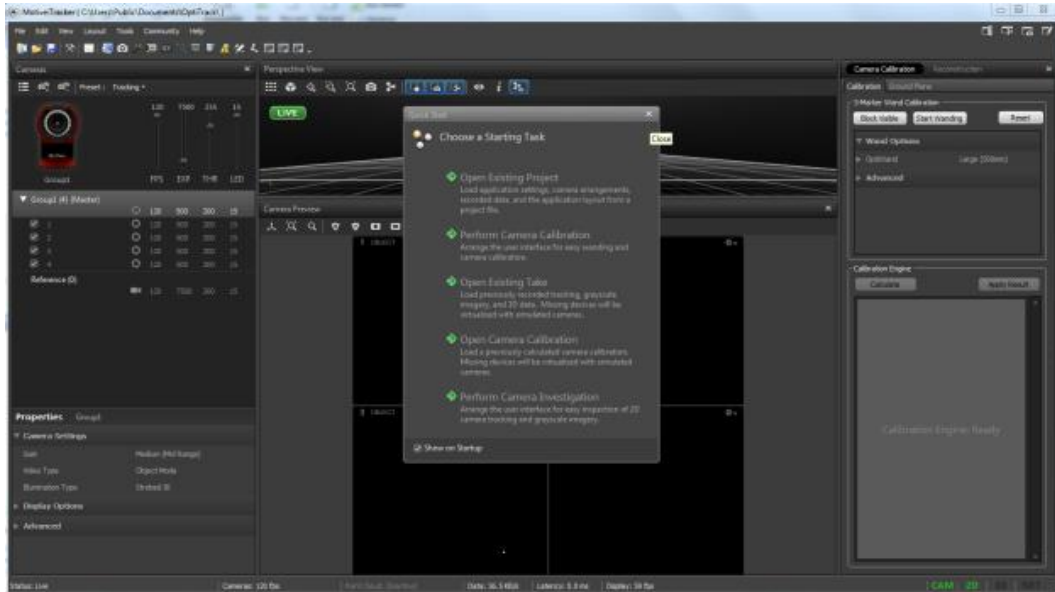


Figure 2.37. Optitrack Motive startup window

There are different ways to setup the cameras. The rule to check a camera setup is good or not is the visibility of the DUT in the optical tracking software. In the optical tracking software, change the mode of the camera to 'Camera X -> Video Type -> 1280x1024 Grayscale mode (Fig. 2.38)'. For measurement segment mode for all the cameras is the right setup.

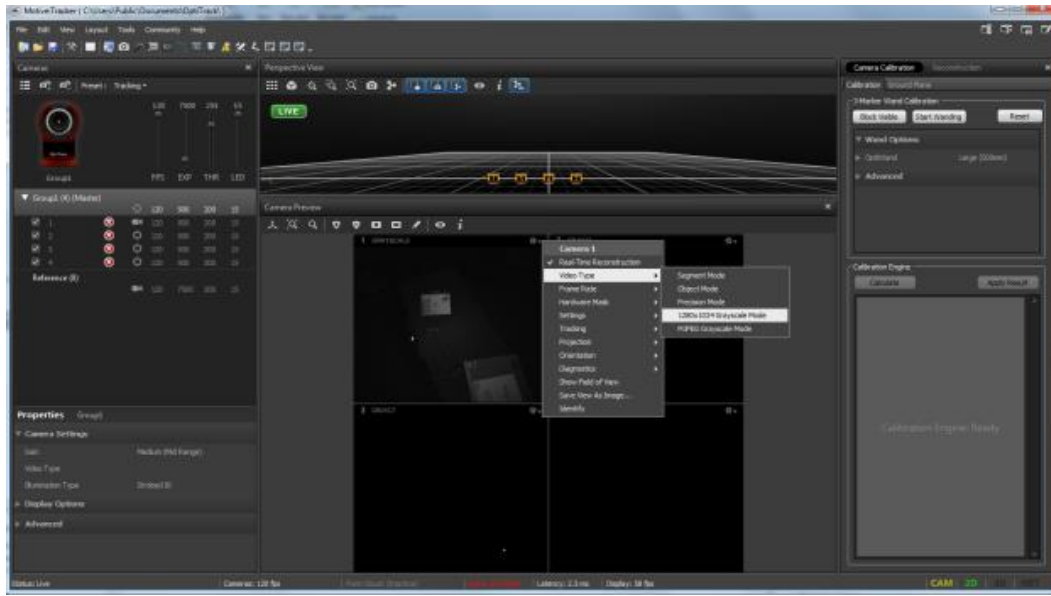


Figure 2.38. Changing video type

To setup the measurement environment appropriately, no reflective things should be present within the coverage of the cameras. If some bright spots are visible other than DUT which might interfere with the markers, then press the ‘Block Visible’ soft key on the right of the screen to filter them out. This will remove the visible bright spots from the scanning area. Another option is to reduce the exposure of each camera on the left side of the screen. The optimal exposure used for the lighting condition at the EMC lab was 60.

To provide a space tracked with good positioning accuracy, camera calibration is a must. Calibration hardware includes the wand, and the ground plane reference. Firstly in the software, press the soft key, “camera calibration”, and then press “Start Wandering”. Using the wand and waving it in front of camera, the camera start acquiring the wand images as shown by Fig. 2.39.



Figure 2.39. Wand use to calibrate the optical tracking system

Waving the calibration wand within the coverage of the cameras, sample points for each camera will be taken and recorded by the software, as shown by Fig. 2.40.

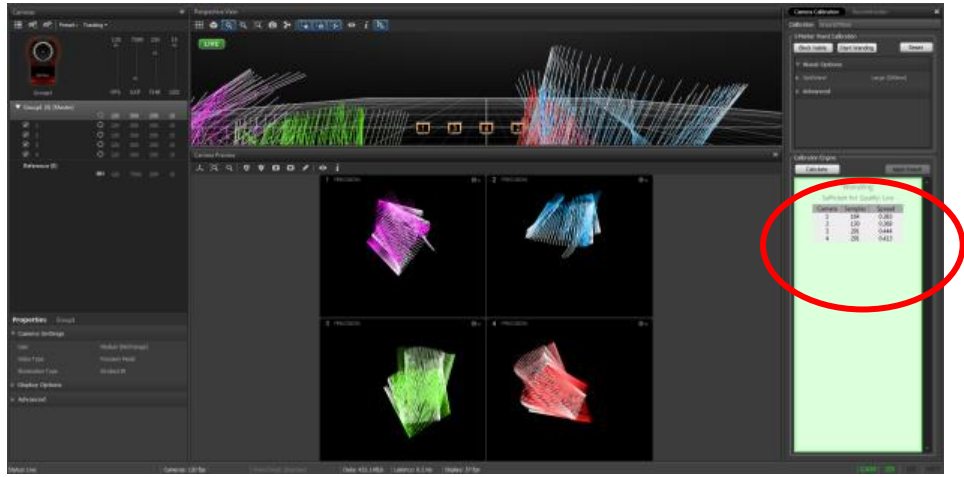


Figure 2.40. Wand calibration in progress

During Wandering, the number of samples captured by the cameras is shown on the bottom right side of the screen. It also shows the updates the status of calibration as sufficient for quality parameter. The accuracy of the calibration depends upon the quality, when it reaches 'High' wandering can be stopped.

The next step is to press the ‘Calculate’ to start calculation of results and complete the calibration procedure. After calculation is completed the software was pop-up showing ‘Ready to Apply’ (Fig. 2.41). At that point, the results can be applied. Also it will ask to save the calibration (Fig. 2.42 and Fig. 2.43).

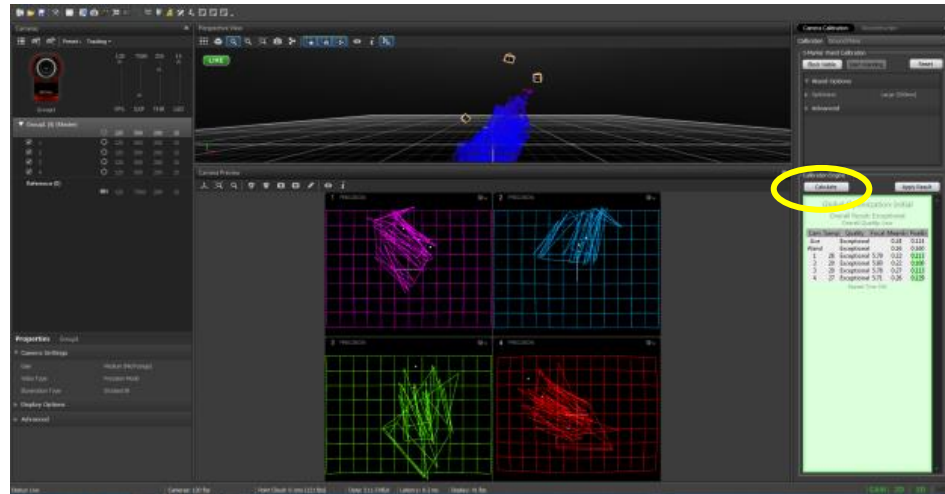


Figure 2.41. Calibration calculation in progress, waiting to apply the result

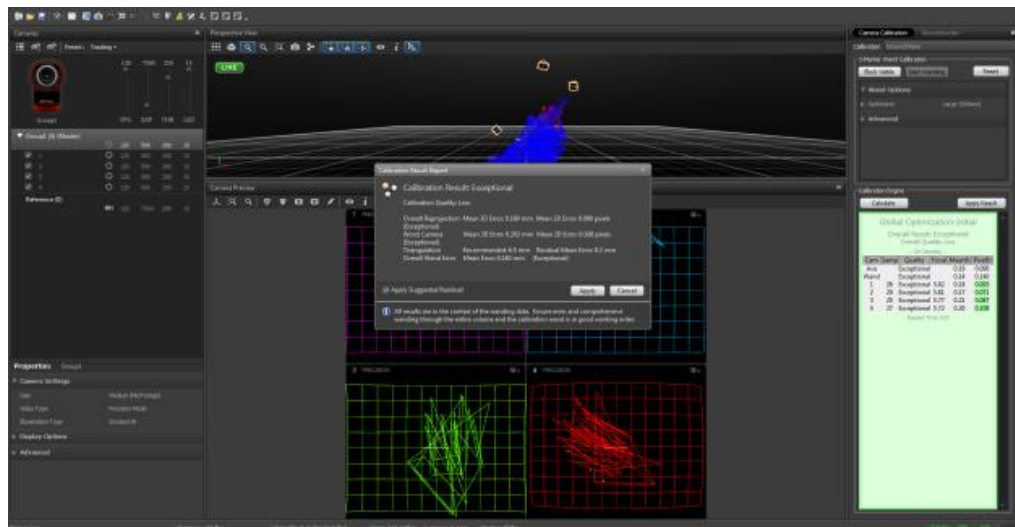


Figure 2.42. Calibration calculation complete



Figure 2.44. L-shape ground plane reference body

Place the ground plane reference body on the location where you want the coordinate system to be located. Ensure the three markers are seen by all the cameras, and no other markers are present except the three markers belong to the reference body.

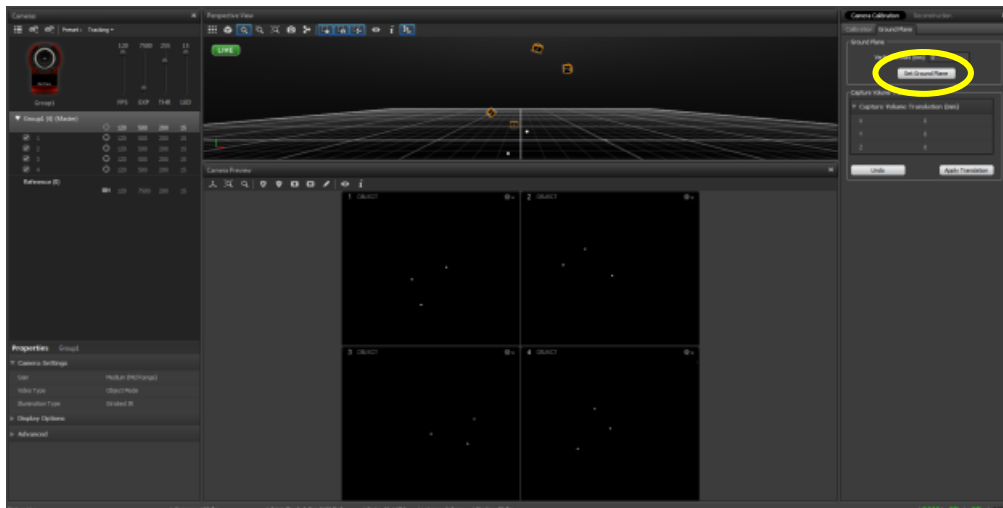


Figure 2.45. Setting up the ground plane reference

In the software, the ‘Set Ground Plane’ softkey sets the ground plane reference (Fig. 2.45). Any vertical offset can be set as required. After setting up the ground plane reference the software will ask to save this calibration too (Fig. 2.46).

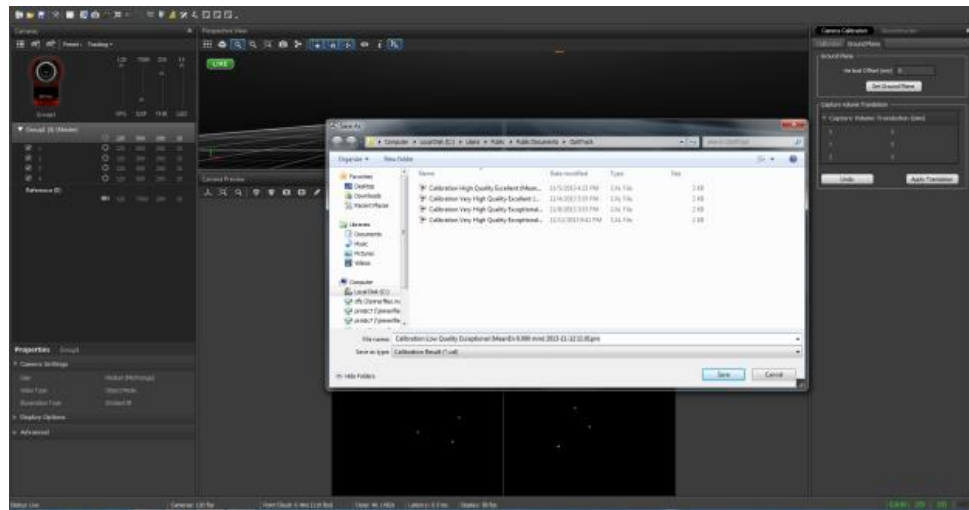


Figure 2.46. Saving the ground plane reference calibration

The adapted field measurement probe in Fig. 2.47 can be need to be tracked. To track the probe the rigid body has to be defined in the optical tracking software. To do that, the rigid body is firstly fixed on top of probe as shown below and placed in the view of cameras.

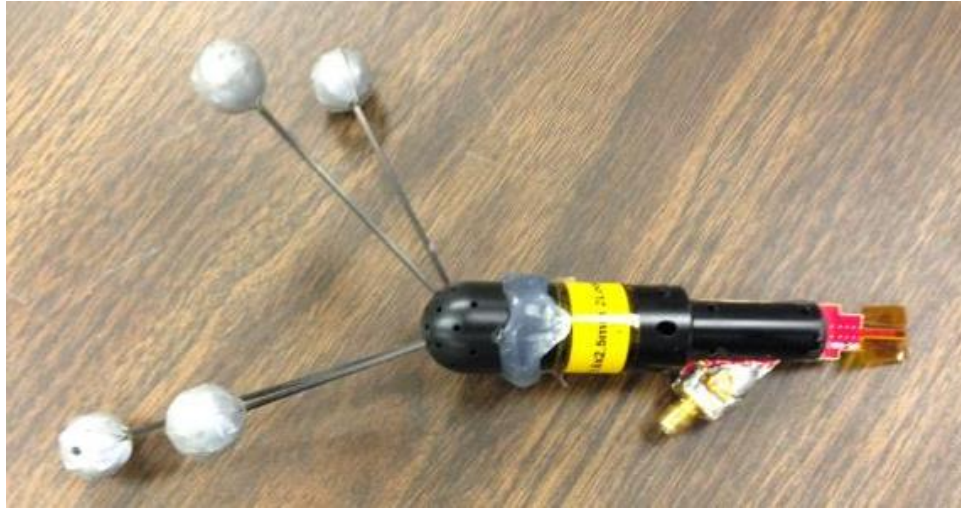


Figure 2.47. Field probe with rigid body fixed on top of it.

Also an extra marker kept on the tip of it for calibration purpose. When the rigid body along with probe is kept in view of cameras, it is seen in the optical tracking system as shown in Fig. 2.48. A rigid body need to be created within the software. Use mouse to select the markers belongs to the rigid body target in the software, and right click.

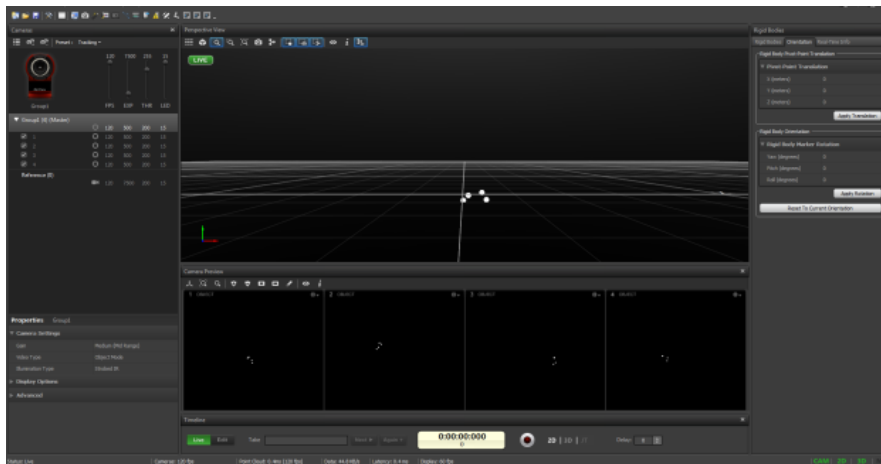


Figure 2.48. Rigid body markers seen in Motive software

Select 'create rigid body', the Motive software can create a rigid body as shown in figure below. Also the markers can be selected individually and 'Create from Selection' softkey can be pressed to create the rigid body.

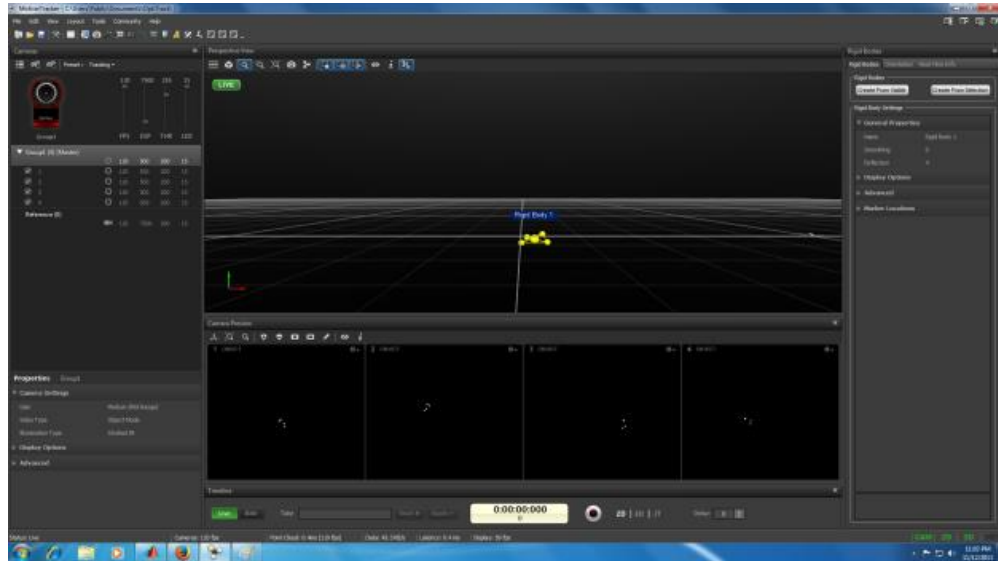


Figure 2.49. Rigid body markers seen in Motive software

For near field measurement, the position of the tip of the probe is the point of interest to be tracked. To do that, place an extra marker is at the tip of the probe to determine the location of the tip of the probe (Fig. 2.50).



Figure 2.50. Rigid body and probe with an extra marker at the tip of probe

This marker along with the rigid body can be seen in the Motive software as shown by Fig. 2.51.

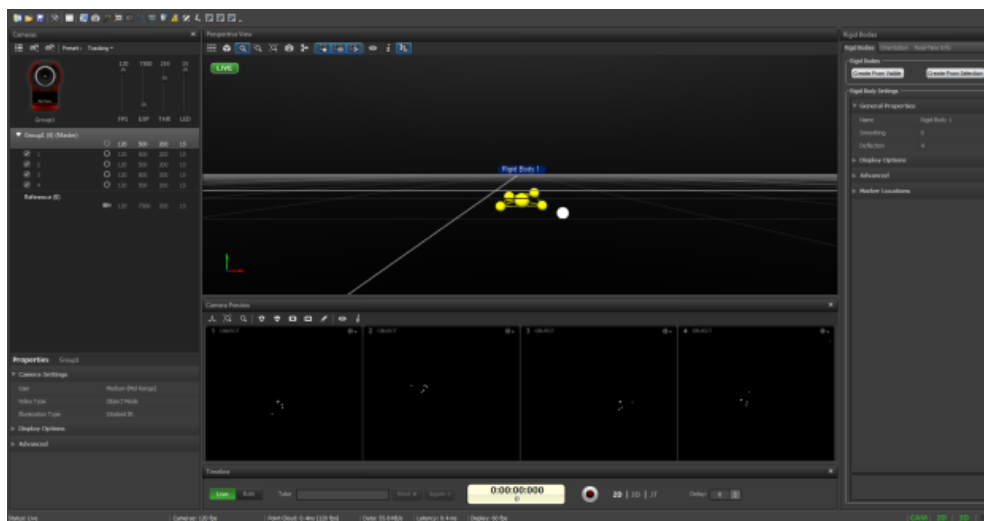


Figure 2.51. Rigid body with an extra marker at the tip of probe

Next is to move the rigid body center (big sphere) marker which is actually being tracked to the tip of the probe. For this the translation has to be done from multiple views as it is a 3D space. Firstly the top view is selected as shown by Fig 2.52.

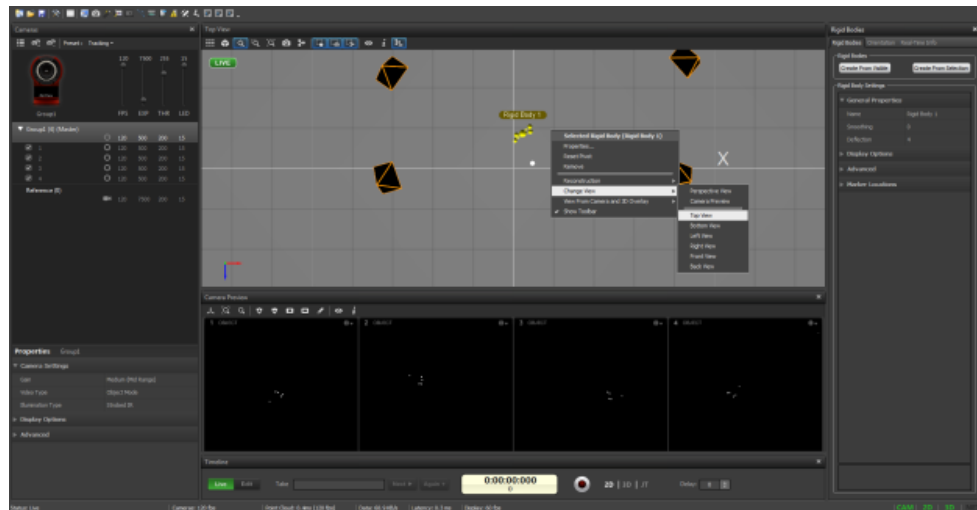


Figure 2.52. Top view for rigid body center translation

In motive software the Y axis is perpendicular to the ground surface. So looking from the top view, the translation has to be done in X and Z orientation. Perform the translation of the pivot point from different views, and ensure the overlap between the extra marker and the pivot point of the created rigid body, as shown by Fig. 2.53 to Fig. 2.58.

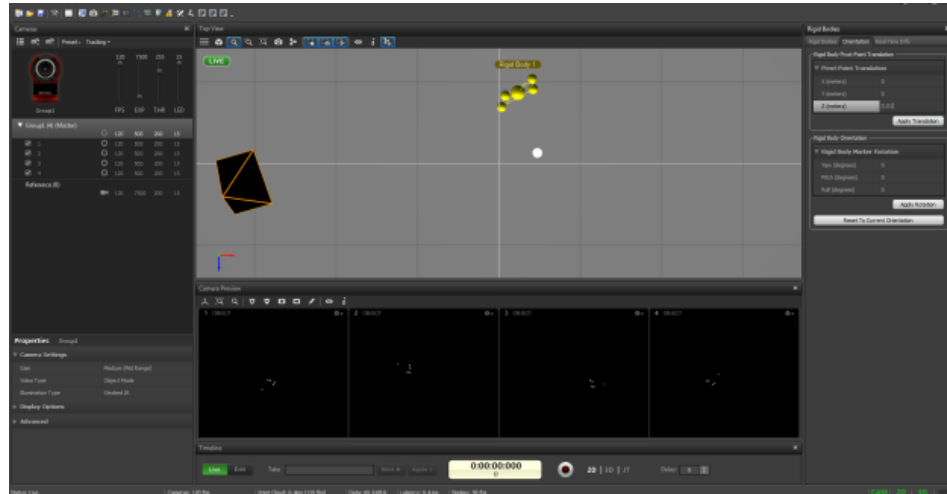


Figure 2.53. Z-translation being applied in the top view

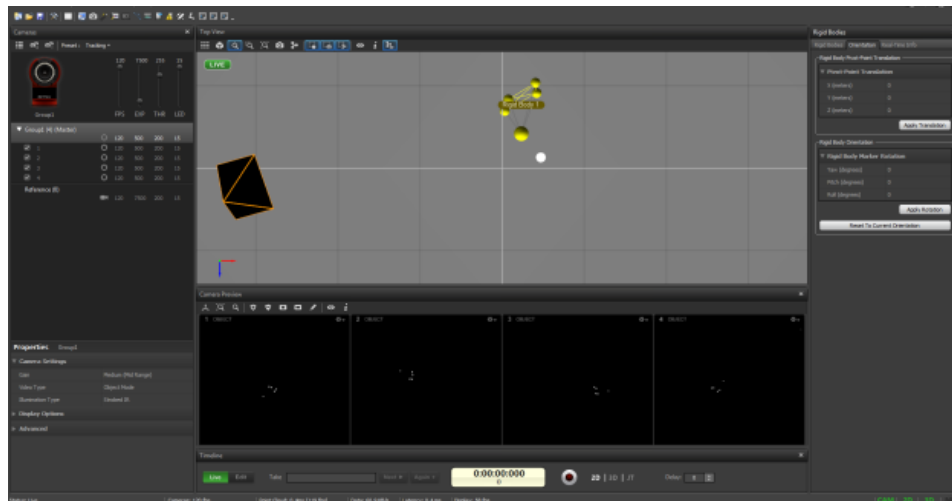


Figure 2.54. Location of big marker after Z-translation in top view

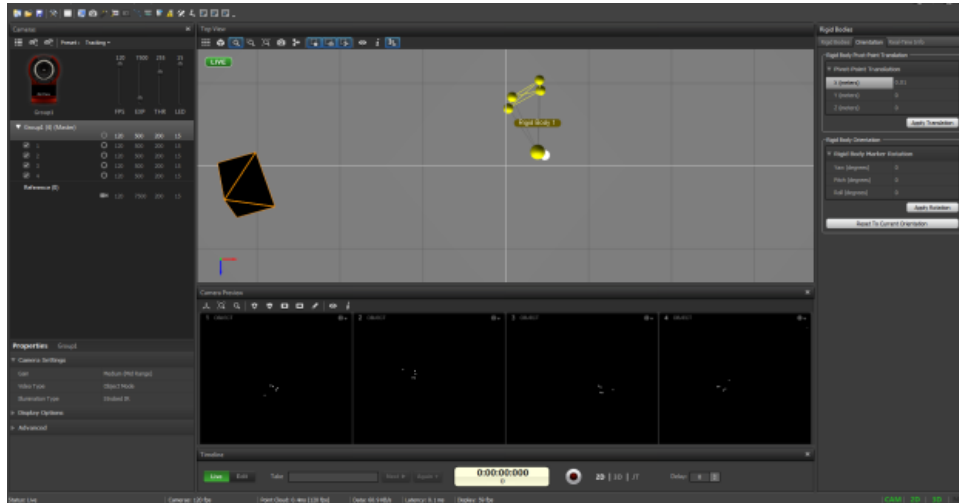


Figure 2.55. X-translation being applied in the top view

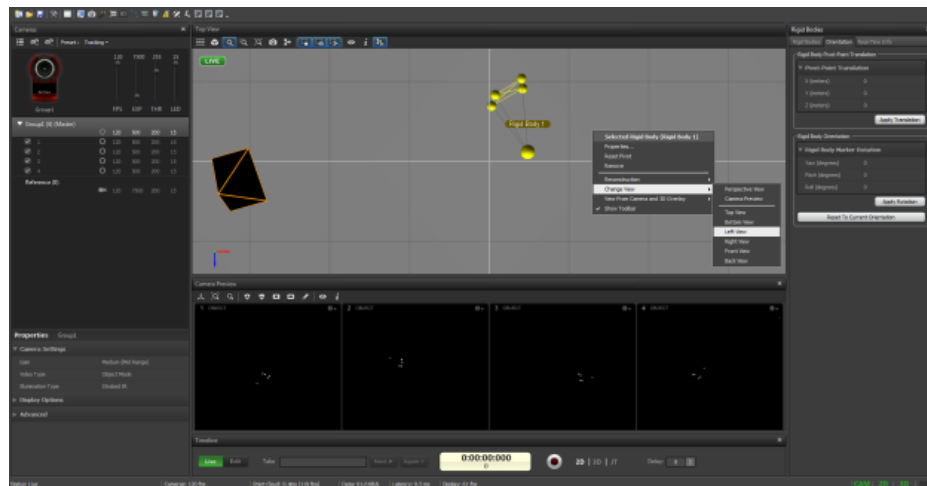


Figure 2.56. Changing of view to left view to move the marker in the Y-orientation

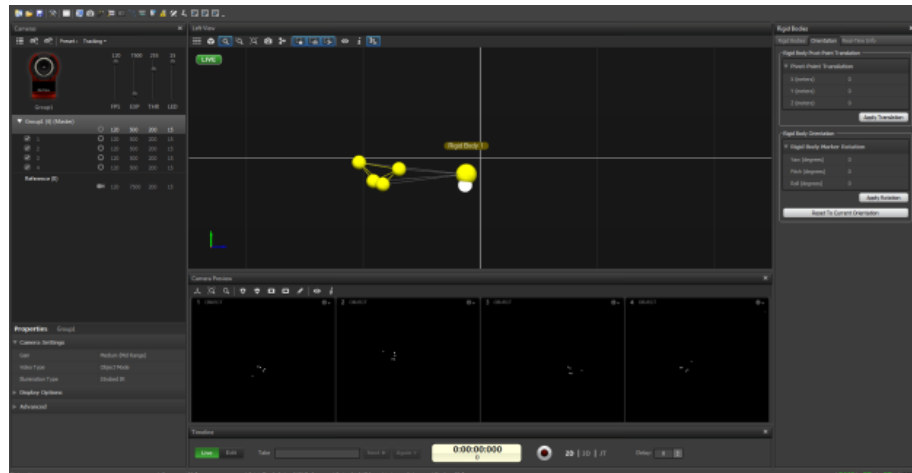


Figure 2.57. Y-translation being applied in the left view

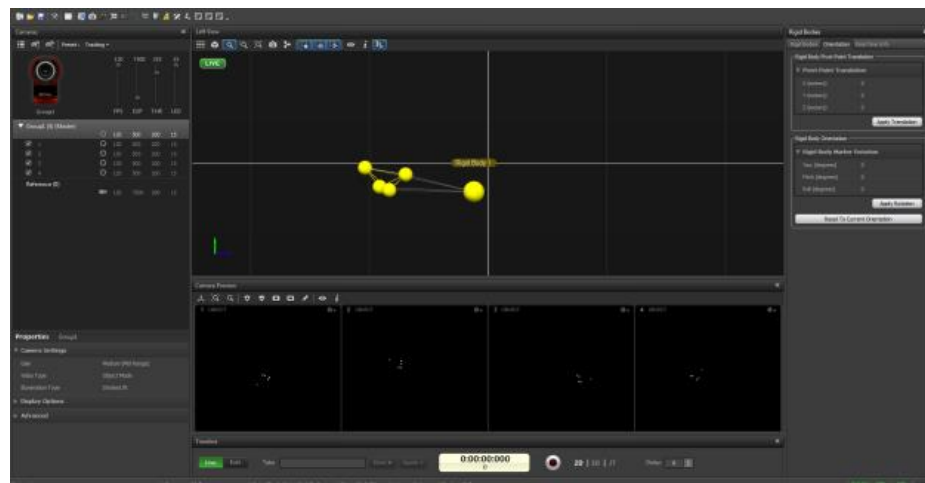


Figure 2.58. Location of big marker after Y-translation in left view

Once the big marker aligns with the tip of the probe the translation can be stopped. Then the current project can be saved.

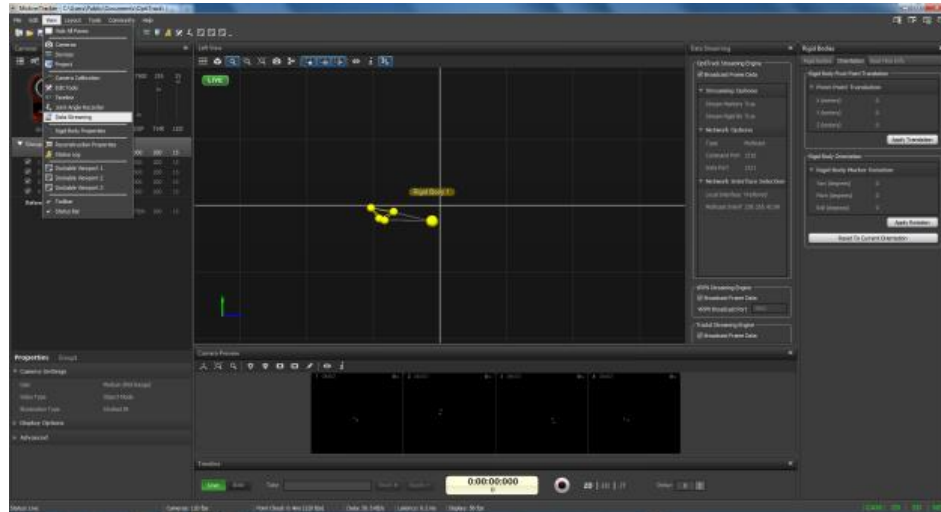


Figure 2.59. Data Streaming

The next step is to turn on the real-time tracking data streaming so the tracking data of the marker can be collected in Matlab. As shown by Fig. 2.59, click the data stream manual on the software. A data streaming window will appear. In that check the ‘Broadcast Frame Data’ in Optitrack Streaming Engine, VRPN Streaming Engine and the Trackd Streaming Engine. Also select ‘Unicast’ from Network Options type instead of ‘Multicast’.

After turning on the data streaming, the real-time tracking of the marker can be observed by moving the marker in the 3D space in the view of the cameras and pressing the ‘real-time Info’ tab as shown by Fig. 2.60.

2.3.5. Near Field Scanning Setup. Figure 2.61 shows the manual near field scanning setup. Tripods are used for holding cameras; a synchronization unit for coordinating the messages from each camera. Adapted EMI scanning probe is held by a user. A workstation with optical tracking software is used for interpreting the video messages from the cameras and the synchronization unit. Manual near field scanning software in the workstation will take both the probe position and orientation from the tracking software and the field strength simultaneously. For more detail about this system, please refer to paper [14].

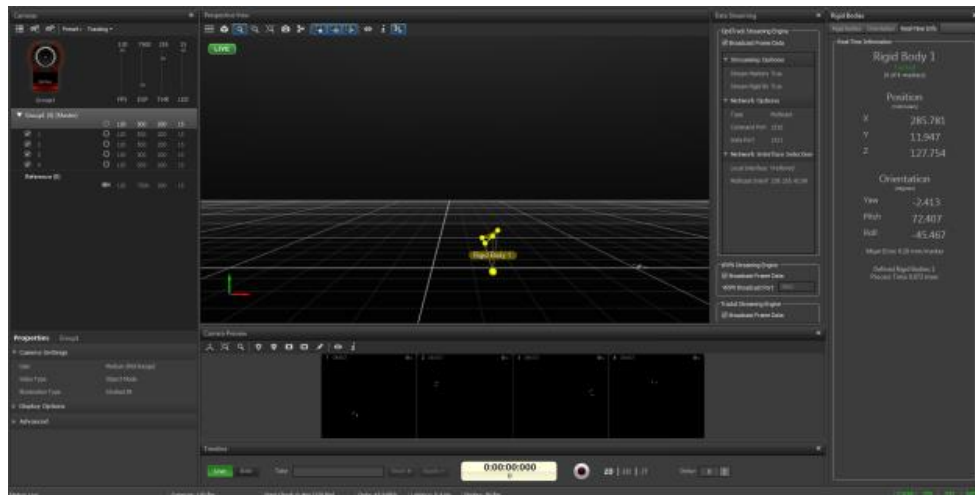


Figure 2.60. Real-time tracking of the big marker (Right window)

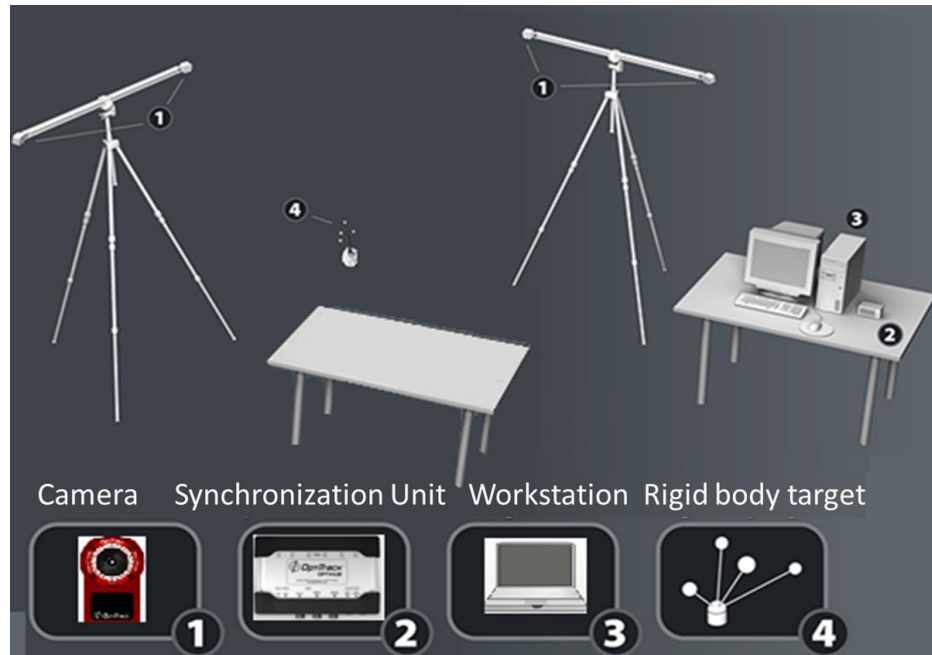


Figure 2.61. Optical tracking based near field scanning setup

2.4. COMPARISON OF THE THREE SYSTEM

Mechanical and optical tracking based systems complement each other. Mechanical tracking is limited by the size of the table or the reach of the arm. Optical tracking allows for larger volume, but fails in shadow regions, such as the interior of an enclosure. For optical tracking based system, to expand the tracking volume, more cameras can always be added, and larger systems can be scanned, which cannot be scanned by the other two systems. In terms of system portability, mechanical systems are more portable, due to their compact structures. Once calibrated, recalibration is not needed when the systems are relocated. On the other hand, the optical tracking system requires tripods or other standstill structures to hold the cameras. Hardware items such as calibration square and calibration wand are needed for position tracking calibration. Once moved, recalibration is always needed.

For the optical tracking based concept, the EMI scanning probe is adapted with a few reflective markers, which is light weight and also has no influence on the field distribution of the DUT. However, for the other two mechanical systems, the probes are connected either with wires or shafts, which to some degree constrained the degree of freedom while the probe is held and moved by the user.

Each system has its pros and cons, and suitable for different scanning situations. Those systems share the same set of applications. In the next sections, the developed applications are described in detail.

3. NEAR FIELD VISUALIZATION

3.1. NEAR FIELD SCANNING PROBE

For an H-field probe, the probe factor calculation is shown by the following equations.

$$V = -\frac{\partial\Phi}{\partial t} = -\frac{\partial B}{\partial t} S = -\frac{\partial H}{\partial t} \mu_0 S \quad (15)$$

$$V = j\omega H \mu_0 S \quad (16)$$

$$|H| = \left| \frac{1}{\omega \mu_0 S} \right| * |V| \quad (17)$$

Where V is the voltage; Φ is the magnetic flux; B is the magnetic flux density; S is the probe loop area; and μ_0 is the magnetic permeability.

Equation (17) gives the probe factor for converting the measured voltages to magnetic field strength. Suppose the orientation of the probe is calculated and denoted as a direction unit vector $\langle \alpha, \beta, \gamma \rangle$. With the H-field magnitude and the orientation of the probe, H-field magnitude in x, y and z axis can be calculated through equations (18), (19) and (20) respectively.

$$|H_x| = |H| * \alpha \quad (18)$$

$$|H_y| = |H| * \beta \quad (19)$$

$$|H_z| = |H| * \gamma \quad (20)$$

So H-field strength is also denoted in a vector format. With the H-field strength for each scan point, the overall H-field distribution are obtained by 2D interpolation. Also, by following the boundary conditions of a surface between two dielectrics, the surface current density distribution can be determined.

Figure 3.1 shows a typical H-field probe that can be used for near field manual scanning. This probe is a Hx probe, with 1mm loop size. Its corresponded frequency response is shown by Fig. 3.2.



Figure 3.1. H-field probe used for hand scanning

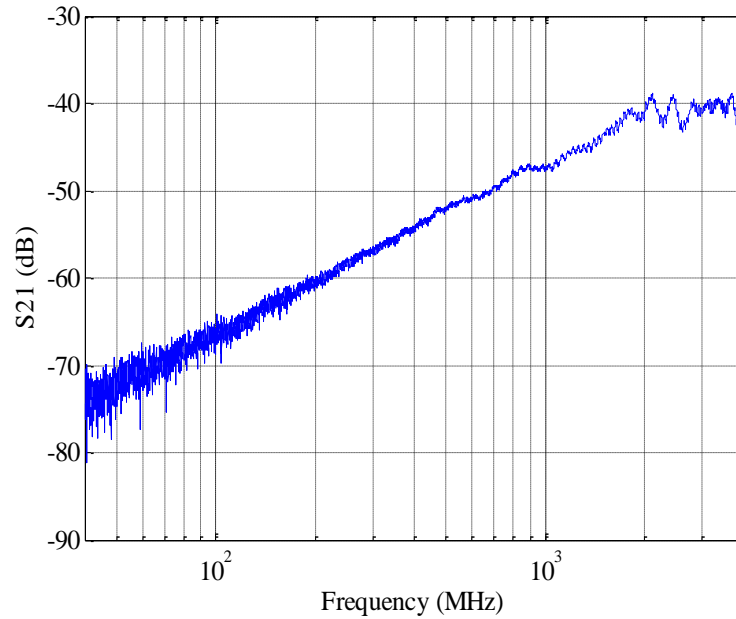


Figure 3.2. H-field probe's frequency response

3.2. NEAR FIELD SCANNING TEST CASE

Optical tracking system is used to demonstrate the procedure of the manual near field scanning system. Figure 3.3 shows the measurement setup for near-field scanning using the optical tracking system. To evaluate the performance of the system, a test structure is built (Fig. 3.4), which is a 2 mm thick aluminum box with a slot open on the top surface. Outer dimensions of the box are: length 187 mm, width 120 mm and height 82 mm. The slot has length 80 mm and width 17 mm. A signal generator output is used to excite the slot with a sinusoid voltage. The frequency of the signal generator is set to be 100 MHz with magnitude as 0 dBm. The box is internally loaded with ferrites to suppress the cavity resonances. Figure 3.5 shows the Hz-field probe (sensitive to fields along the probe axis) used for near field scanning. The measured field strength values along with

the location and orientation data is documented and plotted in real- time. Figure 3.6 shows the data plotted when scanning the top surface of the test structure.



Figure 3.3. Optical tracking based manual scanning

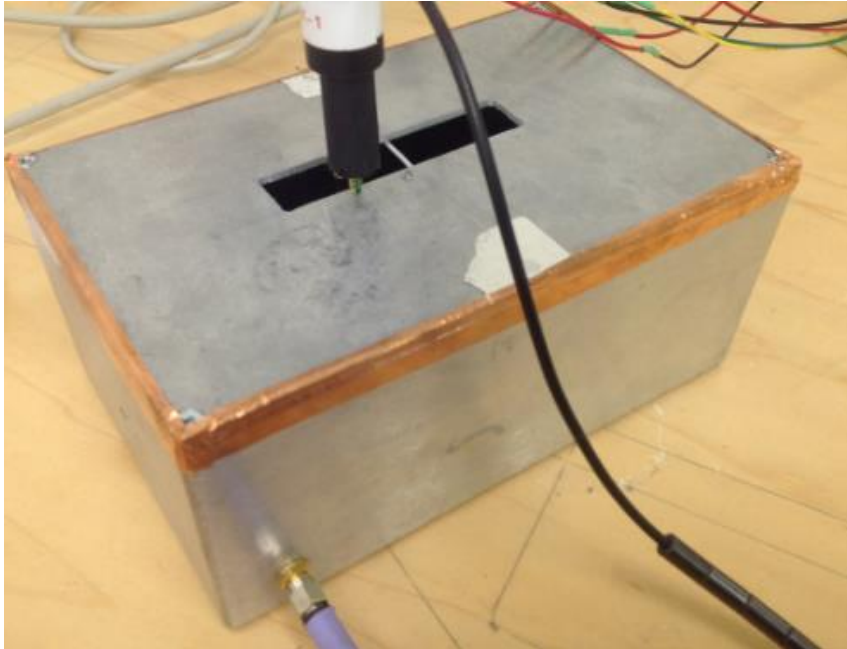


Figure 3.4. Aluminum test box with a probe over the slot



Figure 3.5. Hardware setup with DUT placed within the field of coverage

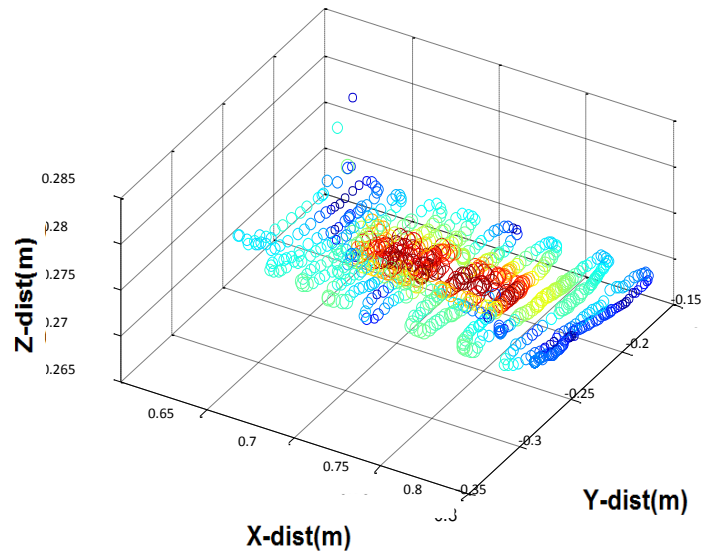


Figure 3.6. Real-time scatter plot of the fields on the top surface of the DUT

3.3. FIELD DISTRIBUTION FROM INTERPOLATION

With the collected data points, interpolation is conducted to obtain a field strength map on the captured 3D geometry. The duplicate data points captured by the user are detected and removed, and the corresponding values are averaged for interpolation. Figure 3.7 shows the interpolated manual scanning result.

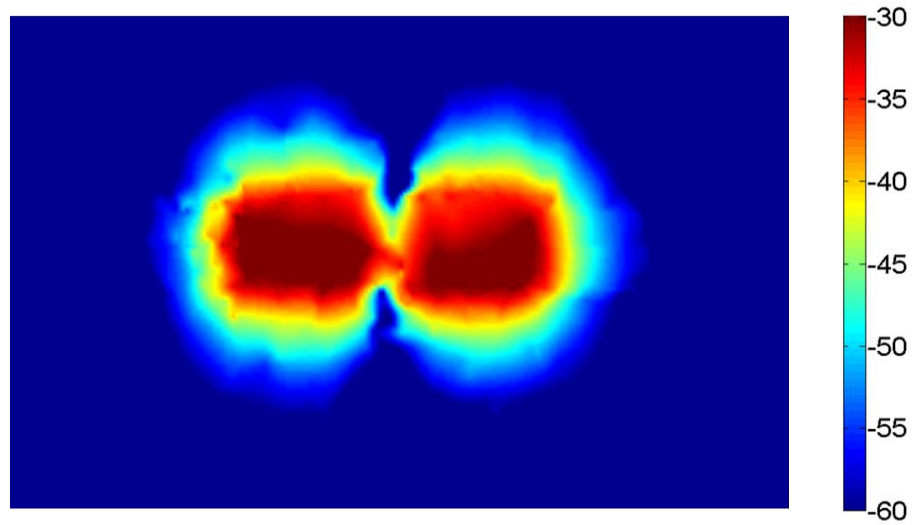


Figure 3.7. Near field scanning from manual scanning (Unit: dBA/m)

3.4. EMC STUDIO SIMULATION

In order to validate the results for the near field H-field scan over the test structure, an EMC Studio [23] simulation is conducted. A model with the physical dimension of the top surface of the aluminum box is created. At the test frequency of 100 MHz the box dimensions are electrically small and the model can be simplified by neglecting the box side and bottom surfaces. Similarly to the scan case the box is excited by a voltage source with of 100 MHz sinusoidal signal of 1.414V peak. The simulation model is shown in Fig. 3.8.

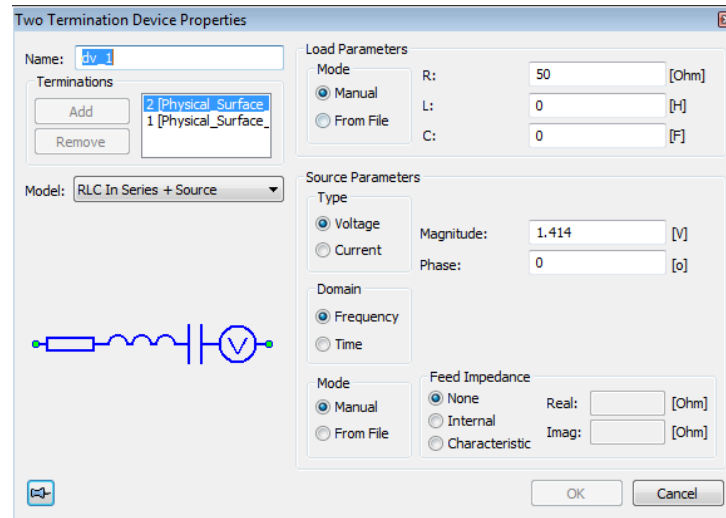


Figure 3.8. Voltage source modeling

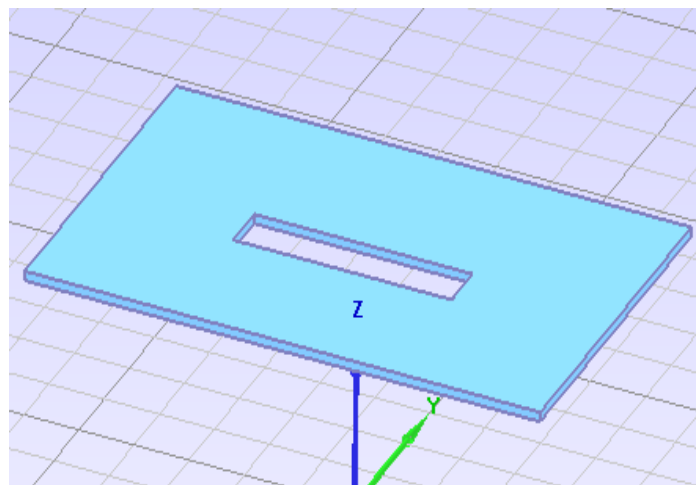


Figure 3.9. Geometry modeling

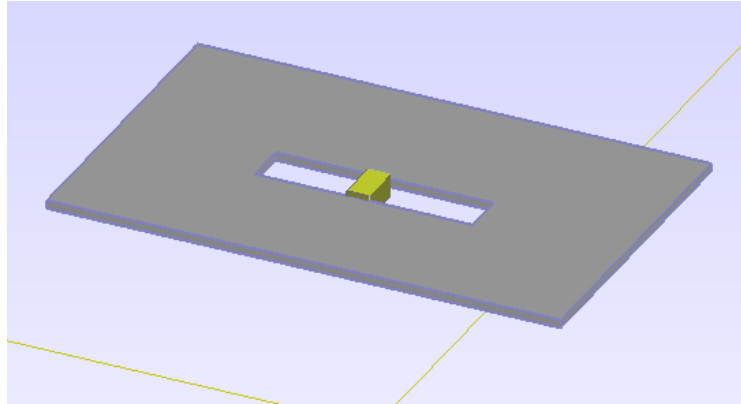


Figure 3.10. The complete model

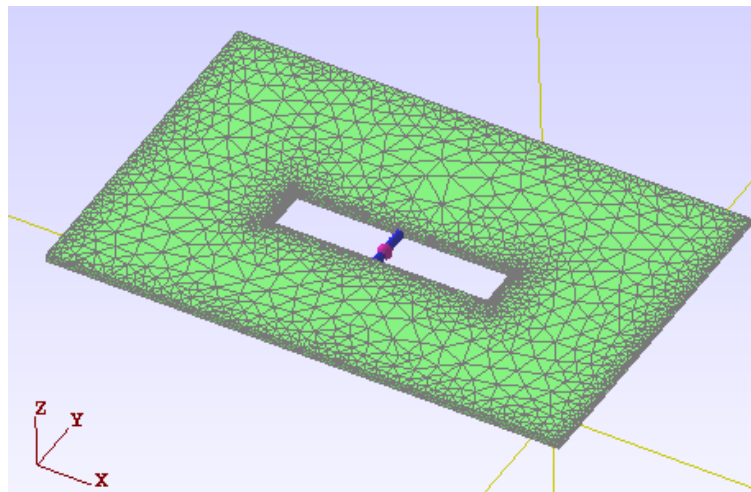


Figure 3.11. The mesh model

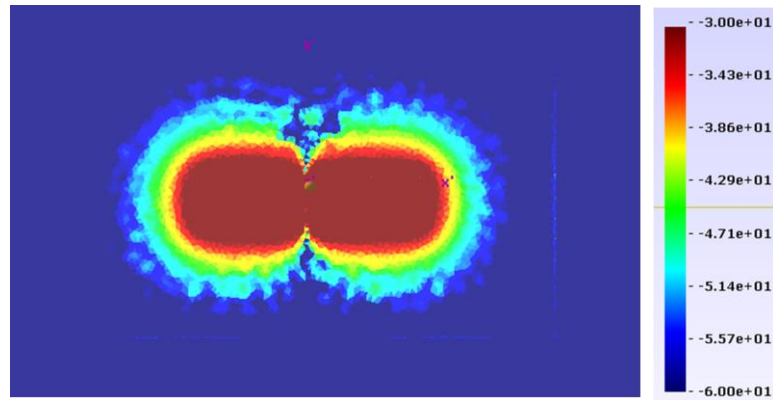


Figure 3.12. Near field from manual scanning (Unit: dBA/m)

As observed, the field distribution obtained from manual near field scan agrees well with the distribution obtained from full wave simulation. The accuracy of the field distribution depends on the number of points collected, but the accuracy of interpolated results is directly proportional to the number of points captured in the high gradient regions. The positioning accuracy of the tracking systems further limits the accuracy. With higher positioning accuracy, better manual scanning results can be obtained.

3.5. VISUALIZATION OF THE NEAR FIELD STRENGTH IN 3D

3.5.1. 3D Visualization of the Near Field Strength . To obtain 3D map of the near field strength of the DUT, global interpolation is possible but the geometric information of the DUT will change. The sharp edges of the DUT been rounded is problematic from the visualization standpoint. Instead, interpolation can be conducted locally. Figure 3.13 shows the collected near field strength of the five sides of the DUT. And each side was interpolated individually and combined to form a 3D view (Fig. 3.14). By using this method, the gaps between interconnects of local regions are unavoidable.

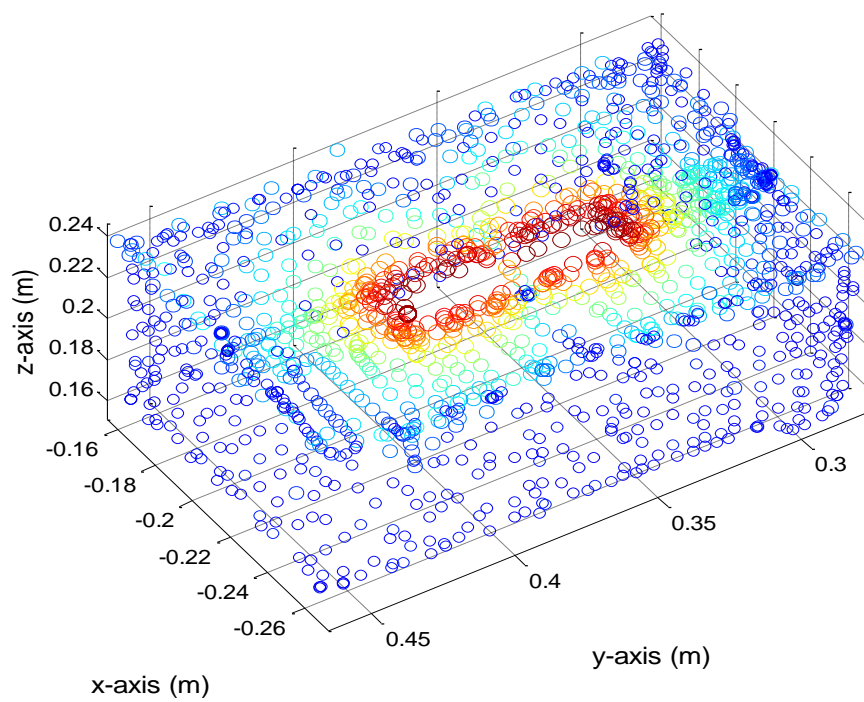


Figure 3.13. Real time scan points plot

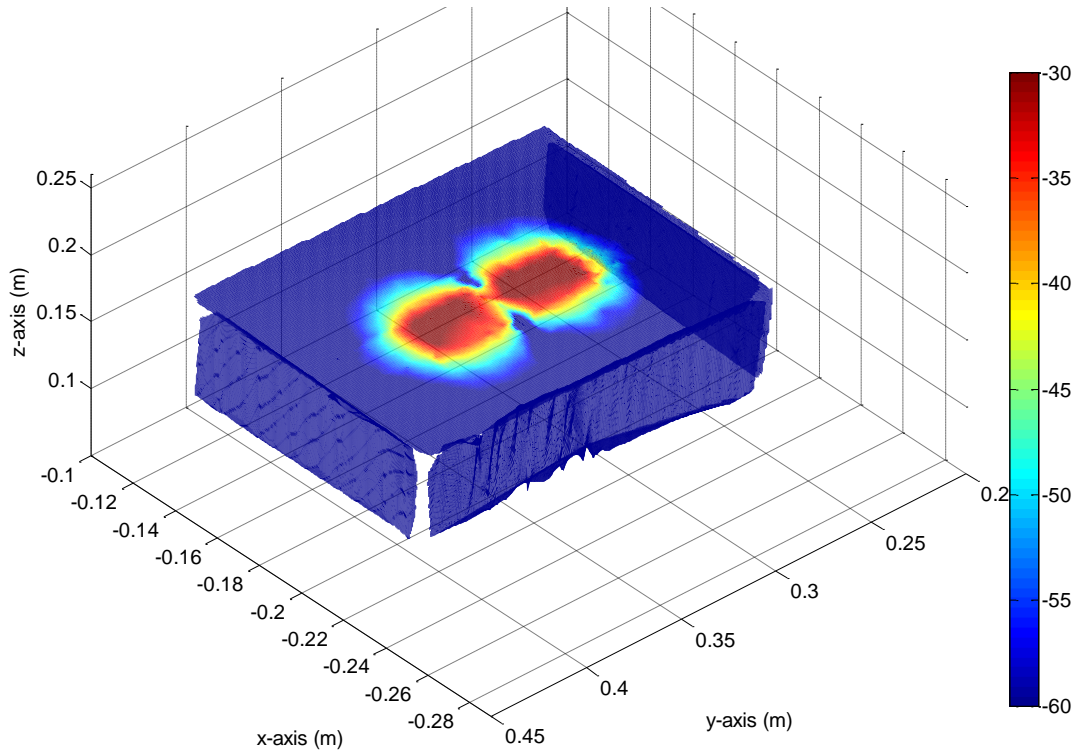


Figure 3.14. Interpolated 3D near field distribution (unit: dBA/m)

In order to obtain 3D near field distribution map of the DUT, a new algorithm is developed, with flowchart shown by Fig. 3.15. The optical tracking system is used to locate the position of the probe. A 3D model of the DUT needs to be obtained in advance, which can either be modelled manually, or through 3D scanning [24]. Here, a 3D model in STL format of the DUT is used. The coordinates of the optical tracking system and the 3D geometry of the DUT are aligned by matching three points from the actual DUT (P_1 , P_2 , and P_3) and also the 3D geometry of the DUT (P_1' , P_2' , and P_3'). From the coordinate values of those points, the translating matrix and rotation matrix can be calculated. Suppose $d = [a, b, c]$ is translated with a , b , and c representing the translation in x , y and z direction for matching P_1' to P_1 , and with $T_d(a, b, c)$ denoting the translating

transformation. $R_z(\alpha)$ denotes rotating angle α around z axis, and $R_x(\beta)$ denotes rotating angle β around x-axis. Overall, three transformations are required. Those three transformations can be combined and represented as a single homogeneous transformation matrix as given in (1), with $c(\alpha)$ denoting $\cos(\alpha)$, and $s(\alpha)$ denoting $\sin(\alpha)$.

$$\begin{aligned}
 T &= R_x(\beta) R_z(\alpha) T_d(a, b, c) \\
 &= \begin{bmatrix} c(\alpha) & -s(\alpha) & 0 & ac(\alpha) - bs(\alpha) \\ c(\beta)s(\alpha) & c(\beta)c(\alpha) & -s(\beta) & ac(\beta)s(\alpha) + bc(\beta)c(\alpha) - cs(\beta) \\ s(\beta)s(\alpha) & s(\beta)c(\alpha) & c(\beta) & as(\beta)s(\alpha) + bs(\beta)c(\alpha) + cs(\beta) \\ 0 & 0 & 0 & 1 \end{bmatrix} \quad (21)
 \end{aligned}$$

With the STL file of the DUT been loaded into the program, the center of the inscribed circle of each triangle, as well as their radius are extracted for locating the triangle where the probe is closest. For increasing the frame rate of the scanning process, the locating algorithm first extract the bounding box of the DUT, if the probe is out of the bounding box, no field rendering will take place. And the k-nearest neighbor algorithm [25] is utilized to decrease the searching time.

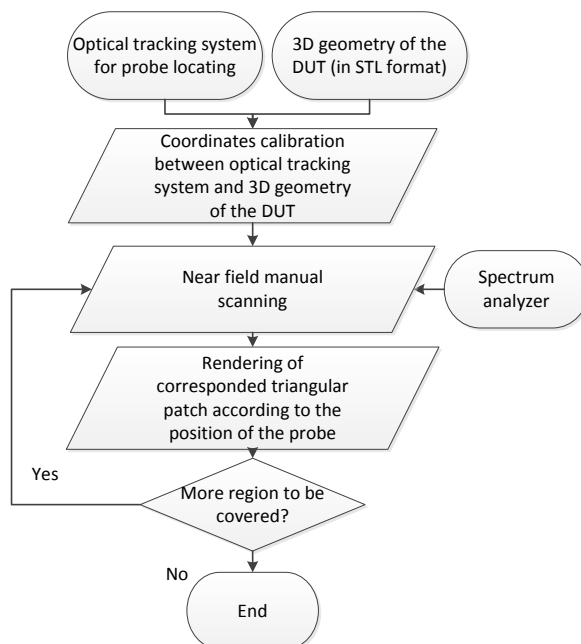


Figure 3.15. Flow chart of real time 3D near field manual scanning

When the probe is detected to be close enough to certain triangle, the color of the triangle is rendered according to the near field strength. All the triangles belong to the DUT can be rendered accordingly, with careful locating of the near field probe.

The algorithm allows a real-time field strength rendering on the 3D geometry of the DUT. Figure 3.16 shows 3D near field manual scanning result having a relatively coarse meshed DUT geometry. Instead of refining the size of all the triangles globally, Fig. 3.17 shows a scanning result with adaptively adjusted triangular mesh. In the region where the field change has high gradient, the size of the triangle is refined, and in the other regions where the field strength is low and constant, the size of the triangle is relatively large. By adaptively changing the size of the triangle, the scanning efficiency as well as the result visualization is improved.

Due to the limitation of human operators, some errors might be introduced. The algorithm allows the engineer to go back to the region where mistakes are suspected and

update the scan result. When the scanning result is satisfactory, the scanning process will be stopped.

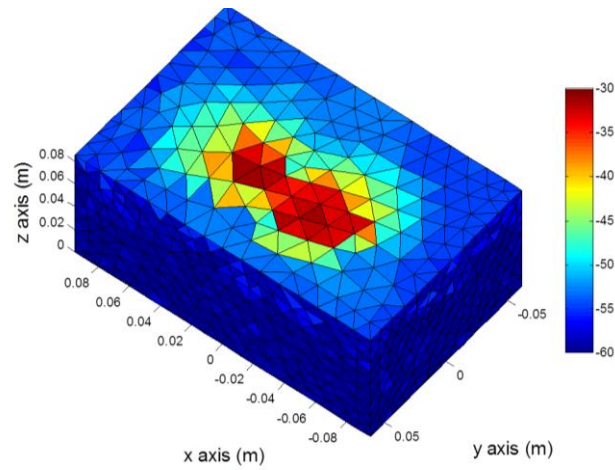


Figure 3.16. Scan result of the test DUT with coarse meshing (unit: dBA/m)

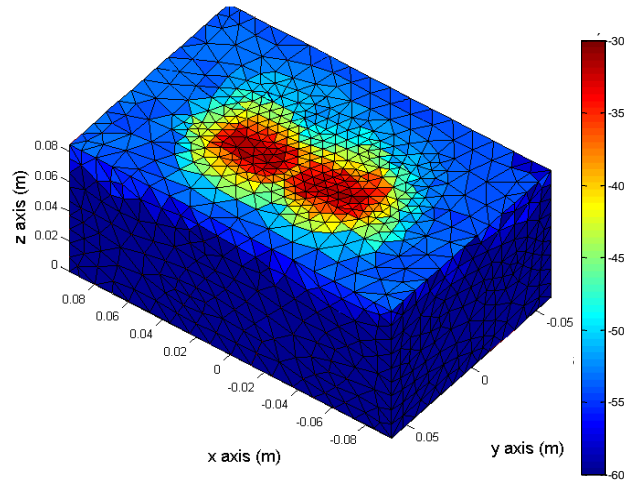


Figure 3.17. Scan result of the test DUT with adaptive meshing (unit: dBA/m)

3.5.2. A Commercial Product Near-Field Scan. The optical tracking system can also be used for near-field scanning using a spectrum analyzer. Such a system would be useful as a quick diagnostic tool for EMI analysis and get a first person idea of the sources of radiation. The setup for near-field scanner is as shown below. Here as only magnitude information is required, spectrum analyzer is used to collect data. The scan can be performed in near-real time by just moving the probe over the DUT.

The near field distribution of a complex object, a laptop (Fig. 3.18) was also scanned to demonstrate the performance of the developed system. As shown by Fig. 3.19, a corresponding mesh model of the laptop is manually modeled for 3D near field visualization purpose. The scanning frequency was 2.4 GHz, which is the Wi-Fi signal emitting from the laptop. To enforcing the Wi-Fi antenna working during the scanning process, this laptop was remotely connected with a PC. Files from the DUT were sent to the remote PC, such that the Wi-Fi antenna was working at the maximum power level.

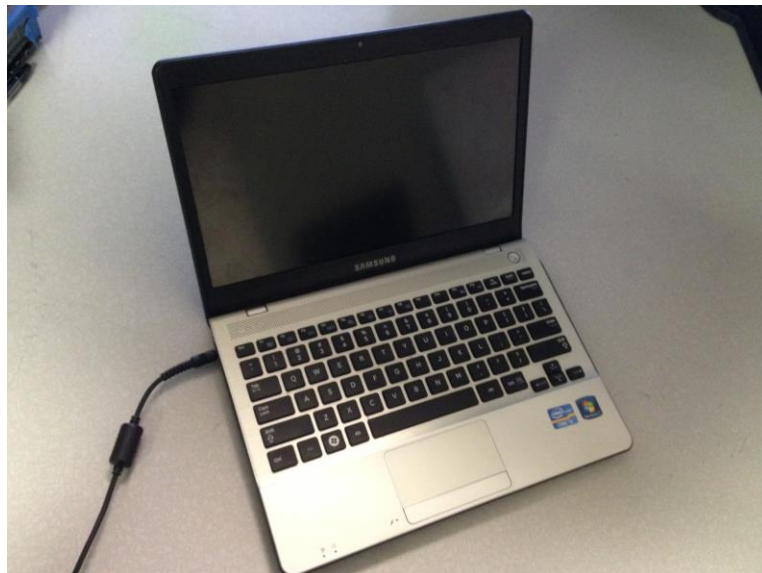


Figure 3.18. DUT – a laptop with cable connected

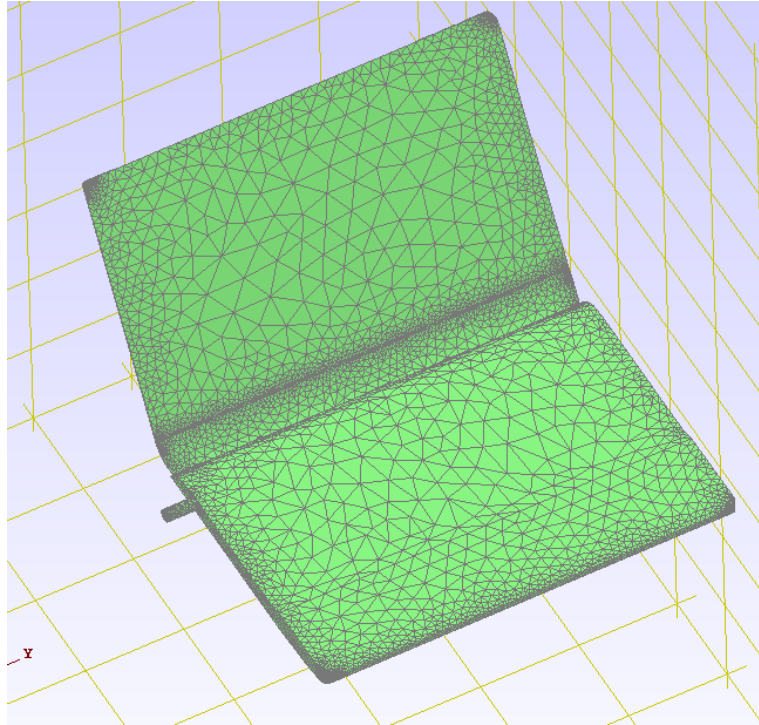


Figure 3.19. Mesh model for 3D field overlay

3.5.3. Test Setup. The measurement setup was very similar to the slot antenna measurement setup as described above. Figure 3.20 shows the actual measurement setup. The same Hz probe was used to measure the normal field distribution over the DUT surface. The probe was tracked by the optical tracking system; SA was used to measure the field strength. A PC was used to receive field information from the SA via GPIB, and receive probe positions from the optical tracking system via USB connection.

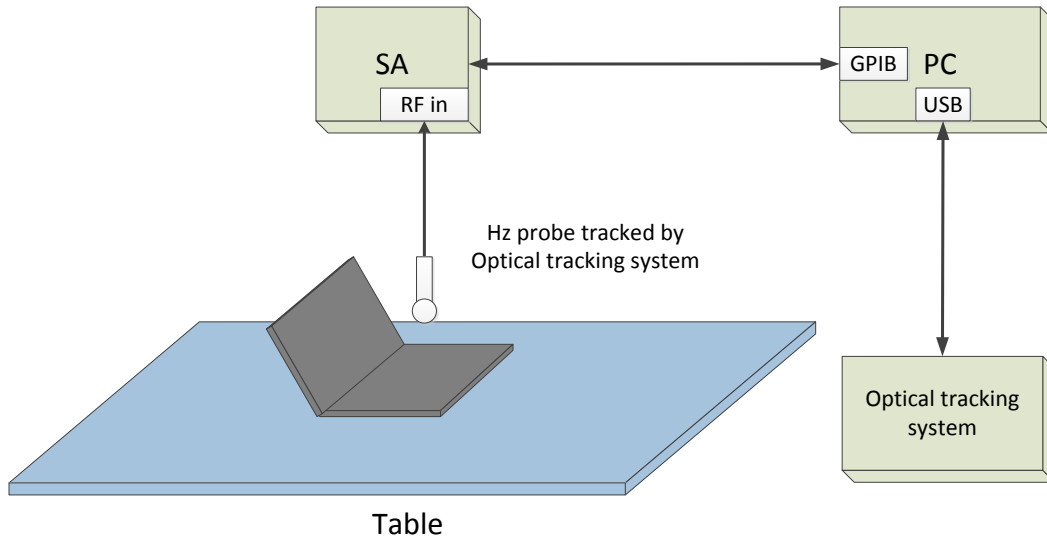


Figure 3.20. Setup for near field visualization measurement

The 3D model of the DUT is shown by Fig. 3.21. Here the 3D model of the DUT was modelled manually. However, CAD models of products are usually available from the vendor. With the model, a discretized model can be created for this field visualization measurement.

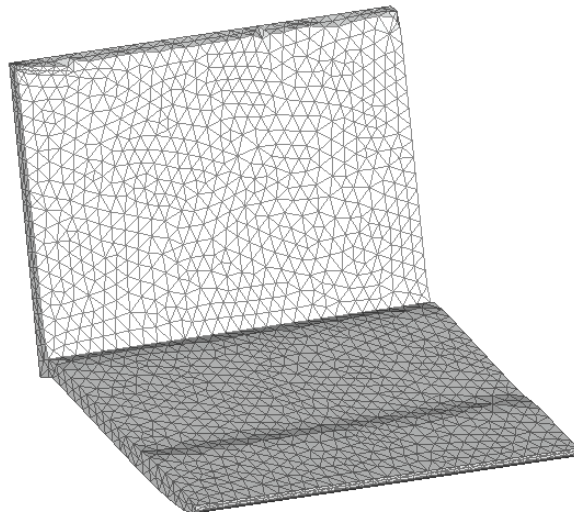


Figure 3.21. 3D model for near field visualization

3.5.4. Test Result. The field distribution of the DUT can be visualized in real-time. Figure 3.22 shows the final field distribution.

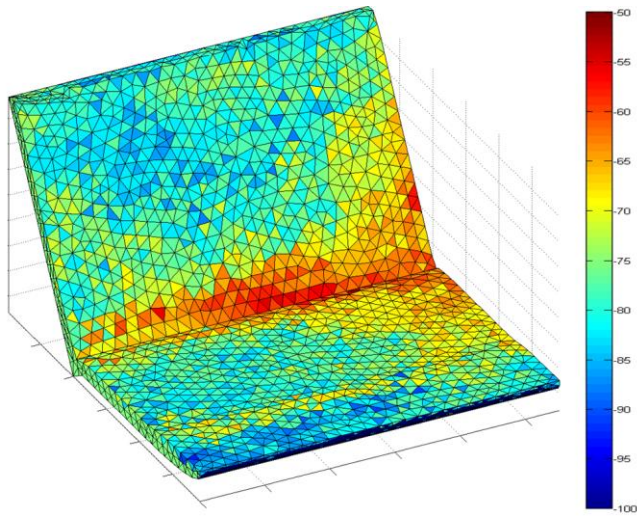


Figure 3.22. H-field strength (dB scale)

4. SAR 2D IMAGING

Optical tracking system based manual scanning system can help engineers to identify EMI sources. The flexibility of manual scanning system with probe tracking capability facilitates an efficient EMI diagnosis. Engineers can use the developed system to identify near field distribution of regions with high chances to be radiating sources. By trial and error, often times, the radiating sources could be identified. However, this diagnosis process often is time consuming, and purely depends on the experience and knowledge of the engineer.

Besides near field electromagnetic scanning, optical tracking system is also applied to emission source microscopy for 2D imaging of radiating source. Near-field contains both evanescent fields and propagating fields. Often, the evanescent waves are dominant, which may lead to the misinterpretation of the dominate sources contributing to the far-field radiation. However, engineers mainly are concerned about the sources of electromagnetic interference (EMI) contributing to far-field radiation.

The same as near field EMI scanning, robotic scanning devices can be used to identify the radiation sources, i.e. the source of the propagating fields. However, for robotic scanning, the probe may not be able to access all locations near the PCB due to the complex geometry and high component density. This leads to the incorrect measurement of fields at different vertical distances from the PCB. To overcome the limitations of near-field scanning in locating EMI radiation sources, the emission source microscopy presented in paper [30] is used to determine the sources of far-field radiation. The method in this paper uses a 2D ESM algorithm based on the SAR technique to detect active sources of radiation on a complex PCB.

The fields from the active radiation sources, along with the amplitude with or without phase, are measured on a planar surface away from the DUT. The probe location is tracked by optical tracking system. A planar surface constructed using foam-core board is used as a reference plane to ensure a planar scan.

4.1. EMISSION SOURCE MICROSCOPY ALGORITHM

Field pattern on the planar scanning field reveals very limited information about the location and number of radiation sources. With plane wave spectrum theory, the measured fields on the observation plane can be expanded. Plane wave theory states that any monochromatic but otherwise arbitrary wave can be represented as a superposition of plane waves travelling in different directions with different amplitudes but the same frequency.

In literature, standard SAR methods use signals reflected from a target and received by a scanning antenna to reconstruct the target's image. The investigators in [26]-[29] have been used SAR for microwave imaging to detect concealed objects and structural defects. To overcome the limitations of the ESM technique developed in paper [30], sparse scanning technique can be used to selectively populate the pre-defined grid. More points can be collected at regions where the near field strength is high and less points on regions with relatively lower near field values. Paper [31] introduces this principle using manual scanning for rapid microwave imaging. The manual scanner in [31] uses a rigid frame, allowing moving the antenna on the scanning plane. The frame obviously constrains the application of the technique (especially limiting the scanning

aperture). The system proposed in this paper is based on the similar principles, but with reduced mechanical constraints on the scanning antenna movement.

Reference [32] shows that electric field intensity in a charge-free region on a plane $(x,y,0)$ can be represented as a superposition of plane waves in the form of Fourier transform,

$$E(x, y, 0) = \frac{1}{4\pi^2} \int_{-\infty}^{\infty} \int_{-\infty}^{\infty} f(k_x, k_y, 0) e^{-j(k_x x + k_y y)} dk_x dk_y \quad (22)$$

$$E(x, y, 0) = F^{-1}(f(k_x, k_y, 0)) \quad (23)$$

Where $f(k_x, k_y, 0)$ is the 2-dimensional Fourier transform of $E(x, y, z)$, as given by,

$$f(k_x, k_y, 0) = \int_{-\infty}^{\infty} \int_{-\infty}^{\infty} E(x, y, 0) e^{j(k_x x + k_y y)} dx dy \quad (24)$$

$$f(k_x, k_y, 0) = F(E(x, y, 0)) \quad (25)$$

Here, k_x and k_y are the spectrum wavenumbers in the x and y directions, respectively. F and F^{-1} are the forward and reverse Fourier transform operators, respectively. Reference [32] shows that the spectrum of the field on any plane parallel to $(x,y,0)$ can be found using,

$$f(k_x, k_y, z) = f(k_x, k_y, 0) e^{-jk_z z} \quad (26)$$

Where $k_z = \sqrt{k_0^2 - k_x^2 - k_y^2}$ is the planar wave dispersion relation, $k_0 = 2\pi/\lambda$ is the free-space wavenumber, and λ is the wavelength of the active source of radiation.

Therefore, if the field on the plane (x, y, z) is known, the field on the plane $(x, y, 0)$ can be found using,

$$E(x, y, 0) = F^{-1}[F(x, y, z)e^{-jk_z z}] \quad (27)$$

where 'z' is the vertical distance of the scanning plane from the source plane.

Using eqn. 27, field can be back-propagated from one plane to another. Suppose the fields are measured on the plane parallel to some source, then the fields on the source plane can be reconstructed. However, the fields are not available in the form of continuous functions. So, in actual measurement, field values are measured at discrete locations. Equation (27) is the basis of the 2-D ESM algorithm.

4.2. OPTICAL TRACKING BASED EMISSION SOURCE MICROSCOPY

Figure 4.1 shows the principle of the developed system. To apply the ESM algorithm, the fields from the sources are measured on a planar surface approximately two to three wavelengths from the DUT in order to be outside the DUT's reactive near-field and to achieve the minimal effect of the probe on the DUT's fields.

Optical tracking system is used to track the position of the field scanning probe. The planar scan is performed manually by optically tracked probe. A regular scanning grid is constructed and populated during the measurement. Due to the flexibility of manual scanning, fields value can be selectively obtained based on the real time observation of the field strength. More points on regions having high field values are

collected. Those points without field values are filled with zeros. By utilizing the ESM back propagation algorithm, the fields on source plane can be determined.

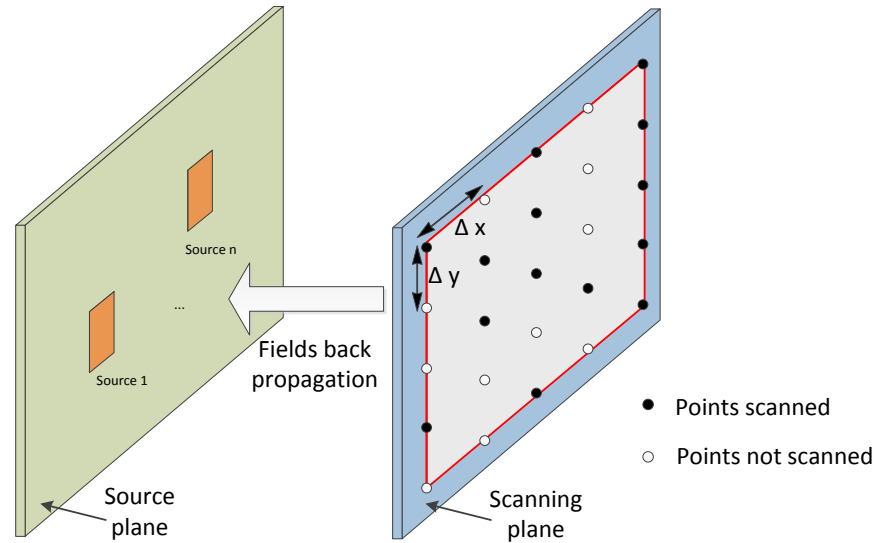


Figure 4.1. Principle of the 2D imaging system

4.3. MEASUREMENT EXAMPLES

4.3.1. Location Construction of Two Antennas. In order to assess the usefulness of the optical tracing system for ESM based EMC applications. Two antennas are placed behind the scanning plane. Here form-core board is used as the reference of scanning plane. A VNA is used for amplitude and phase measurement. The VNA is set to be zero band, 6 GHz. Port 1 excites the antennas, port 2 is connected to the scanning antenna, which is optically tracked (Fig. 4.2).

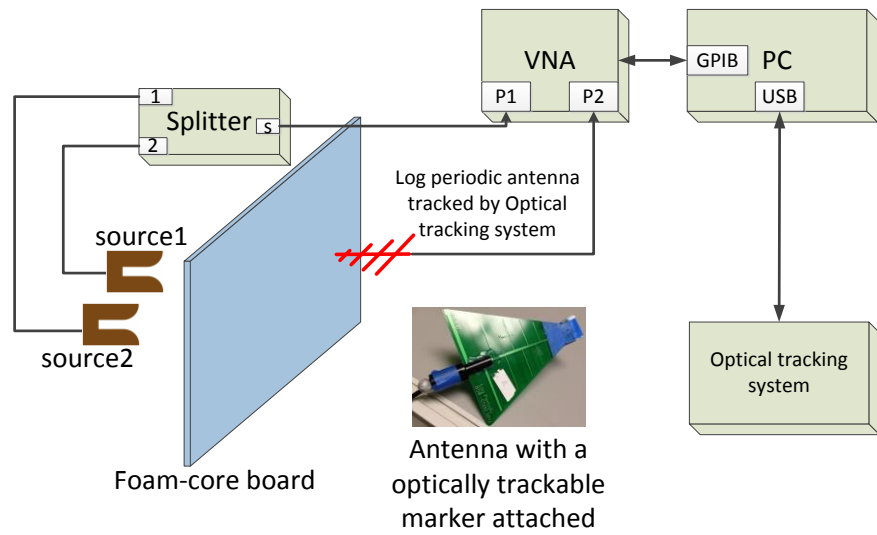


Figure 4.2. Measurement setup schematic

The first step is to setup the optical tracking system as described by chapter 2. The reference coordinate system is placed on the foam-core board as shown by fig. 4.3.

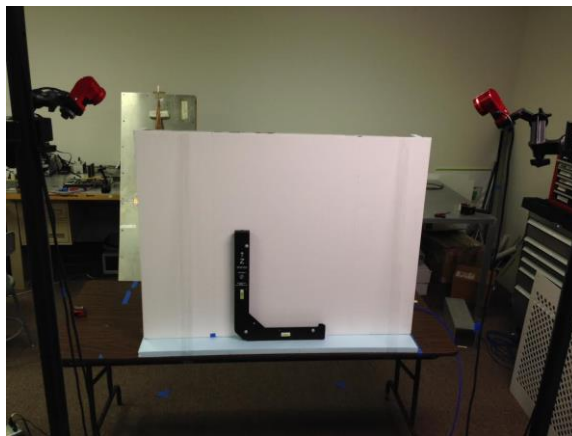


Figure 4.3. Ground plane calibration

After the optical tracking system calibration and reference coordinate system setup. The near field scanning antenna needs to be tracked by the optical tracking system. Different from the near field manual scanning application, a single reflective marker is used for position only tracking. This requires that the operator hold the antenna to either a

vertical or horizontal polarization. Given the fact that inaccuracy may be introduced by the operator for not holding the scanning probe to a perfect horizontal or vertical polarization orientation, a hand held gimbal stabilizer can be used for mounting the scanning probe, such that the scanning orientation can be very well maintained. Figure 4.4, shows the gimbal stabilizer used in this system.



Figure 4.4. Gimbal stabilizer for holding measurement probe

This hand-held gimbal stabilizer is used for camera shooting orientation stabilization, to implement the stabilization of a scanning antenna or waveguide, fixture for mounting the scanning probe to the stabilizer are designed and 3D printed (Fig. 4.5).

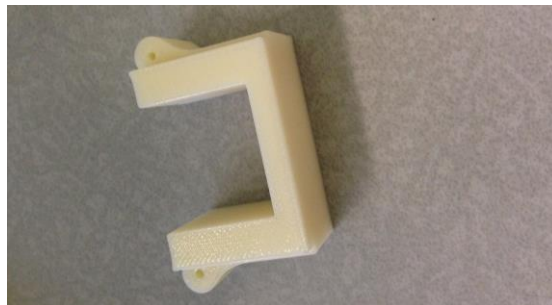


Figure 4.5. 3D printed fixture for mounting probe on gimbal stabilizer

Two antennas with the frequency range cover 6 GHz are placed behind the foam-core board as radiating source (Fig. 4.6).



Figure 4.6. Two antennas placed behind foam-core board

Figure 4.7, shows the overall system setup, the optical tracking system is placed in front of the foam core board. Two antennas are placed behind the foam-core board; a VNA with frequency range from 30k to 6 GHz is used for field magnitude and phase measurement.

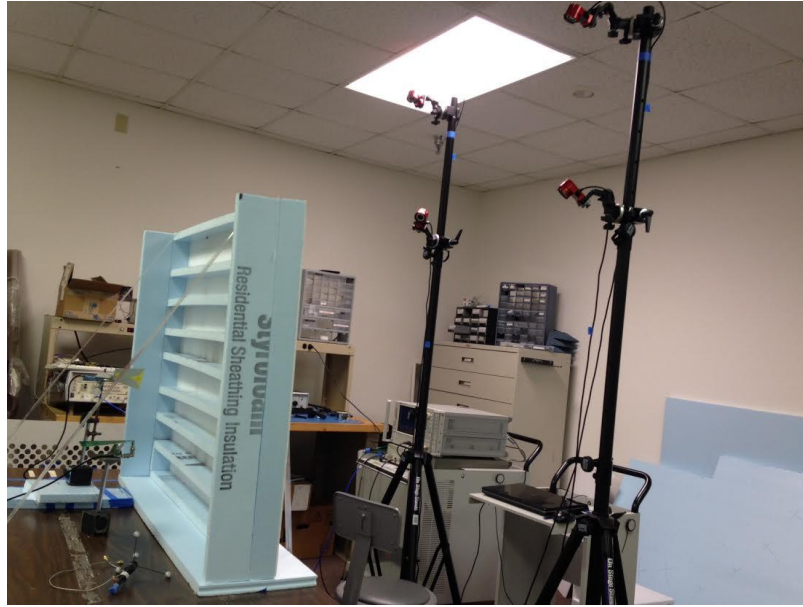


Figure 4.7. Actual measurement setup

Figure 4.8 shows the test result, from which we can see that the source reconstruction results depend on the number of points scanned. More points scanned allow better source reconstruction. From the source plane, the distance between the two source antenna are determined to be 444 mm, which is very close to the actual setup, 445mm. Compared with robotic regular grid scanning, manual scanning is more efficient. The scanning time for this example was around 2 minutes.

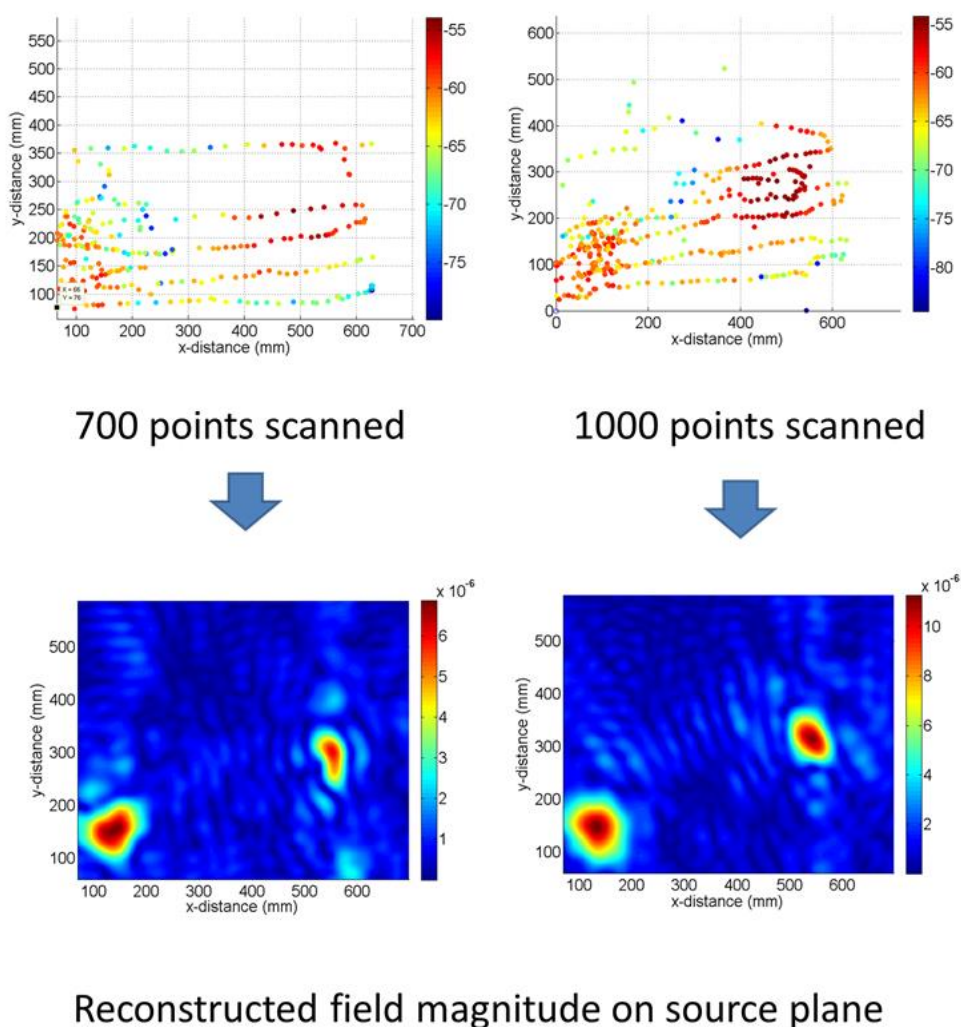


Figure 4.8. Measurement results

4.3.2. Localization of Two Printed Antennas. The above example demonstrated the localization of sources that are relatively far apart. In this example, a custom PCB with several patch antennas and transmission lines was also scanned. Fig. 10 shows layout of the PCB. The PCB was 254 mm x 152 mm, with bigger patches of 20 mm on each side. The measurement was performed at 8.2 GHz.

The planar field amplitude and phase data were recorded on a rectangular plane (foam-core board) above the PCB.

Figure 4.9 shows the custom board patch layout. Patch 1 and patch 2 as indicated in the figure are the two patches to be used as radiating sources.

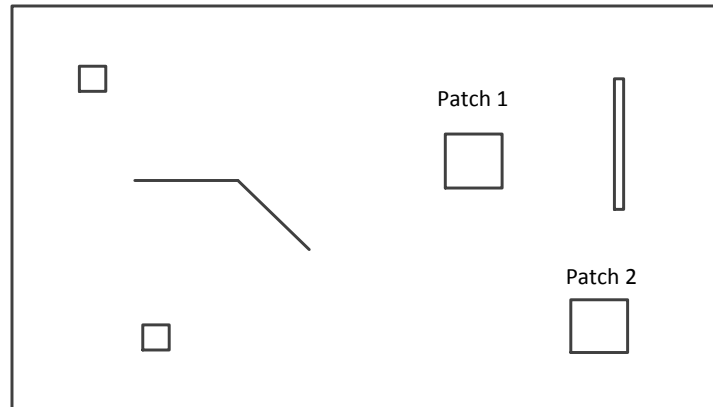


Figure 4.9. Board patch layout

Figure 4.10 shows the custom PCB board. A waveguide is placed directly above the board.



Figure 4.10. Custom board with a waveguide above

The measurement setup is illustrated by Fig. 4.11. Again foam-core board is used as the reference of a planar scanning plane. A VNA is used for amplitude and phase measurement. The frequency is set to be 8.2 GHz. The bandwidth is zero. Port 1 excites the two patches; port 2 is connected to the scanning antenna, which is optically tracked.

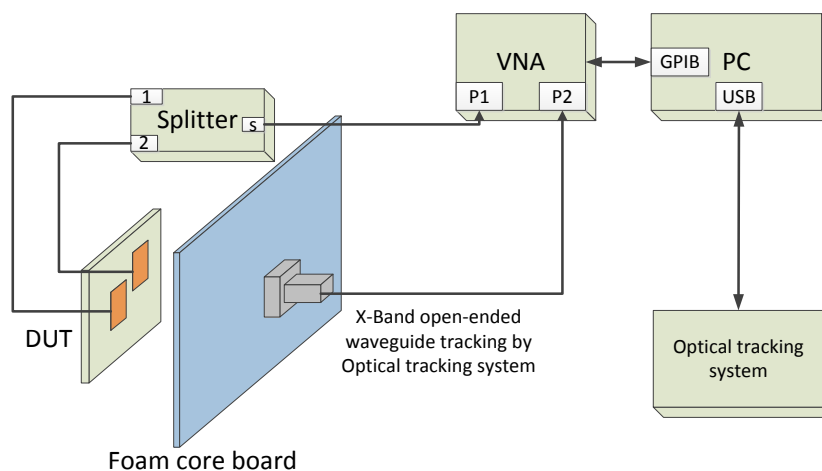


Figure 4.11. Measurement setup

The measurement results is shown by Fig. 4.12. The left figure shows the individual points collected. The right figure shows the reconstructed source 2D image with the collected points.

The scan was performed with the scanning antenna held in two orientations. Both Ex and Ey field on the source plane has been reconstructed. The image of the PCB was overlapped and aligned with the image of the reconstructed source fields to allow an observation of the underlying physical sources of radiation. As Figs. 4.12 and 4.13 indicate, the sources were localized quite accurately.

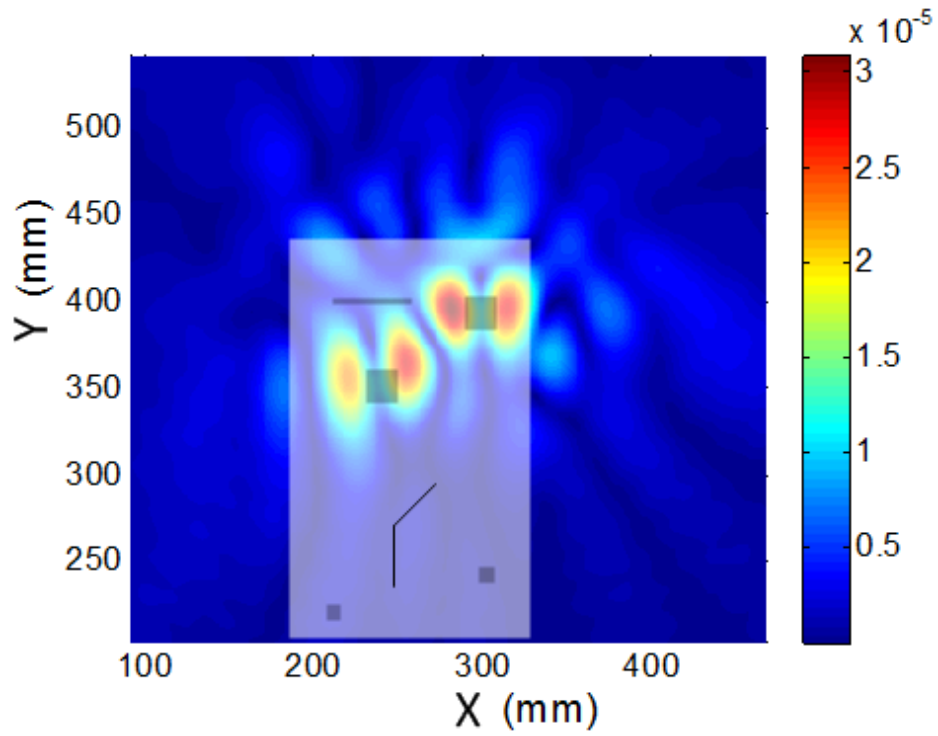


Figure 4.12. Reconstructed E_x field magnitude (V/m) on the source plane

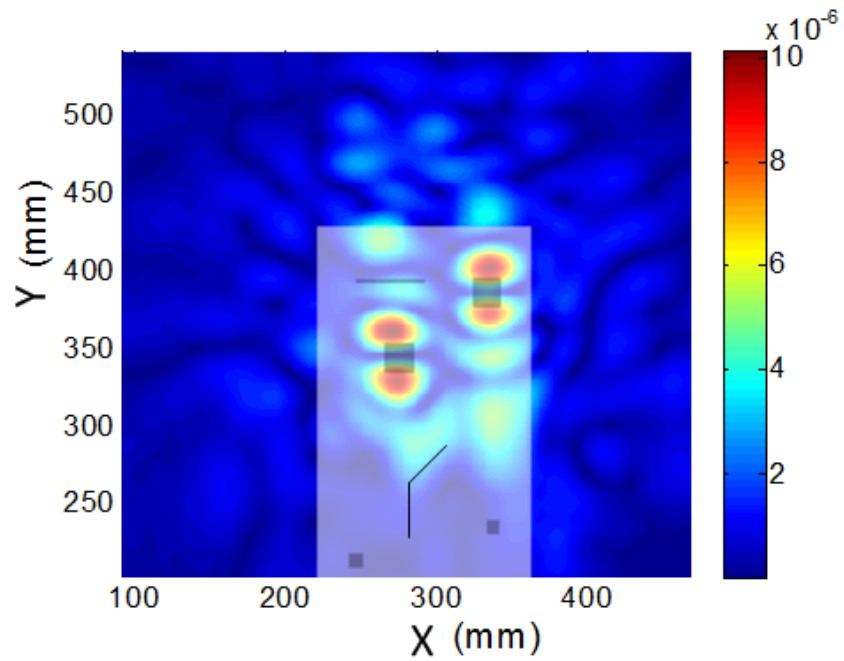


Figure 4.13. Reconstructed E_y field magnitude (V/m) on the source plane

4.3.3. Reconstruction of Source with Metal Plate Interference. Another experiment was done to check the source reconstruction effect. The measurement setup is shown by Fig. 4.14. A metal plate with holes regularly distributed was placed between the planar scanning plane and the two source antenna. The metal plate changed to source. As shown by the measurement setup, the left antenna was placed about 20 cm away from the metal plate, however, the source on right was put very close to the metal plate. Since the source on the left side was some distance away from the metal plate, on the metal plate plane, it was equivalent to several sources. Again the frequency was set to be 6 GHz, 0 span. The scanning antenna was also the log periodic antenna which works up to 6.5 GHz. The scanning result was shown by Fig. 4. 15, and 4.16.

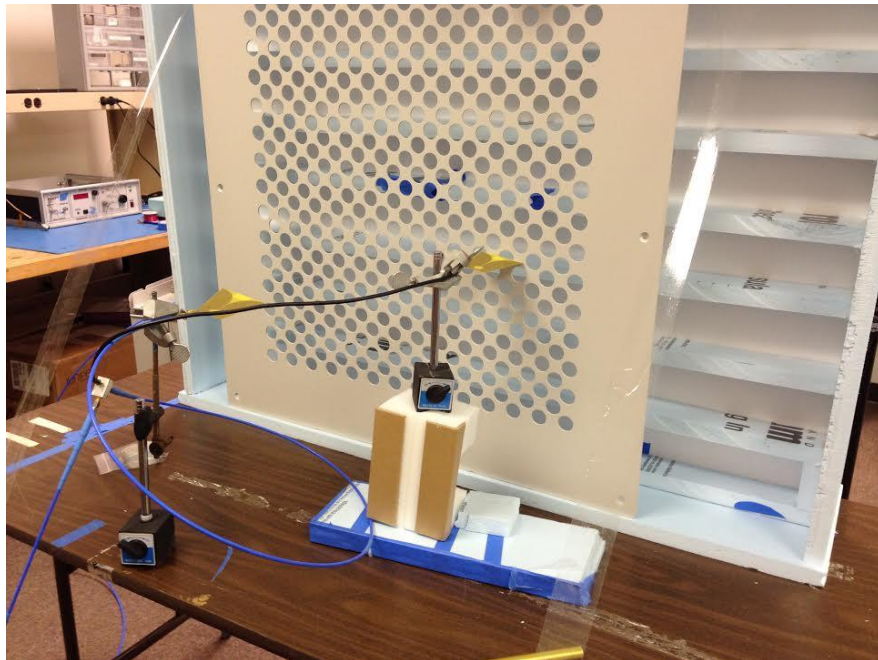


Figure 4.14. Measurement setup of two active sources

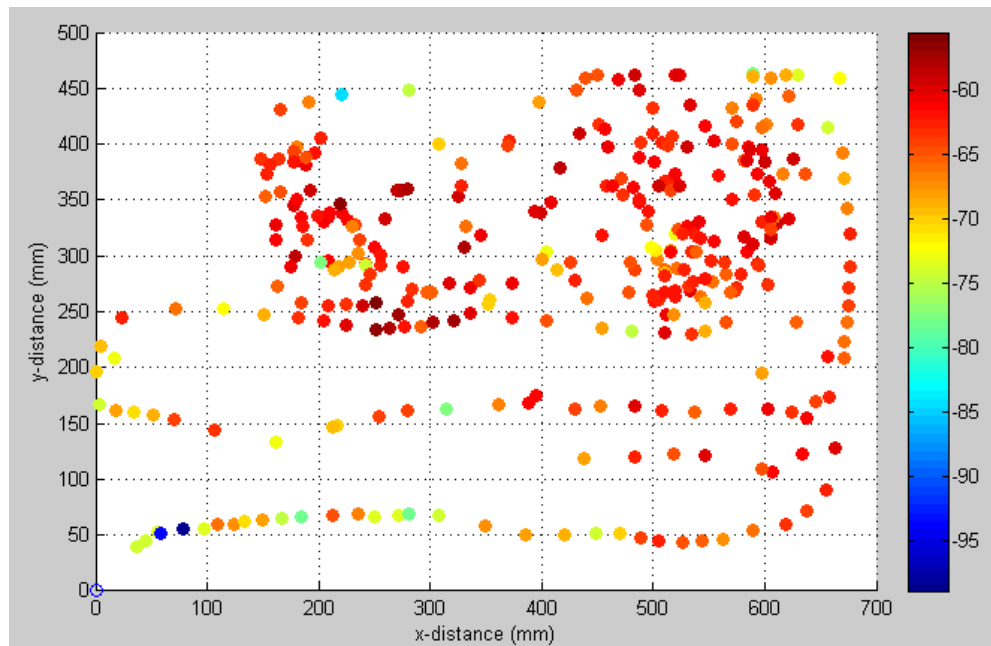


Figure 4.15. Measured field strength on the scanning plane

The reconstructed results shown by Fig. 16 agreed well with what was expected.

It shows two sources, with one source consisting of several sub-sources.

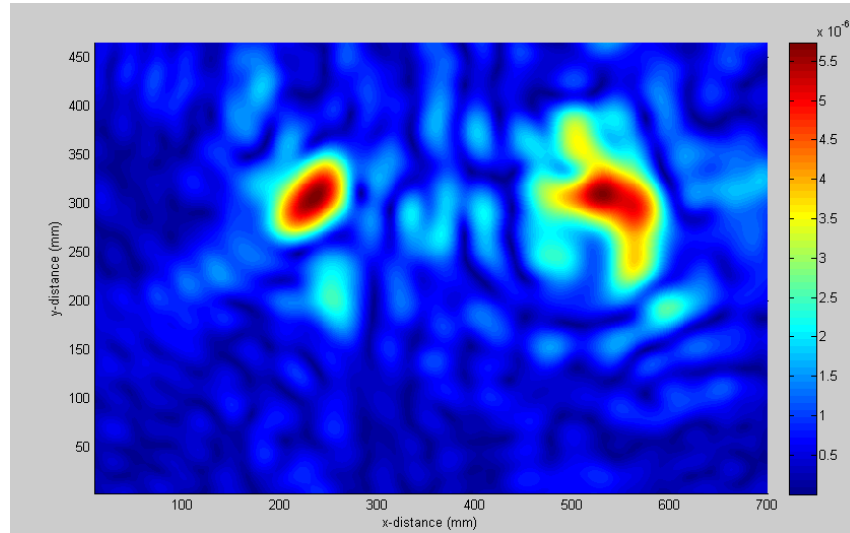


Figure 4.16. Reconstructed image on the source plane

4.3.4. A box with A Slot on One Side. A metal box with a slot on one side was also scanned. There are two SMA female connectors on one side of the box, as indicated by Fig. 4.17. Inside the box, there are two wires; one wire was connected to the inner conductors of the SMA female connectors. This box was excited by port 1 of VNA, with another SMA connector being terminated by 50 ohm load. The purpose of this measurement is to test the application of the developed system in measuring shielding effectiveness of a DUT.



Figure 4.17. A box with a slot on one side

The measurement setup was shown by Fig. 4.18. The DUT was placed behind the foam-core board, with the side having a slot being closest to the scanning plane. Firstly, the frequency was set to be 1 GHz. By scanning, a source was reconstructed (Fig. 4.19).

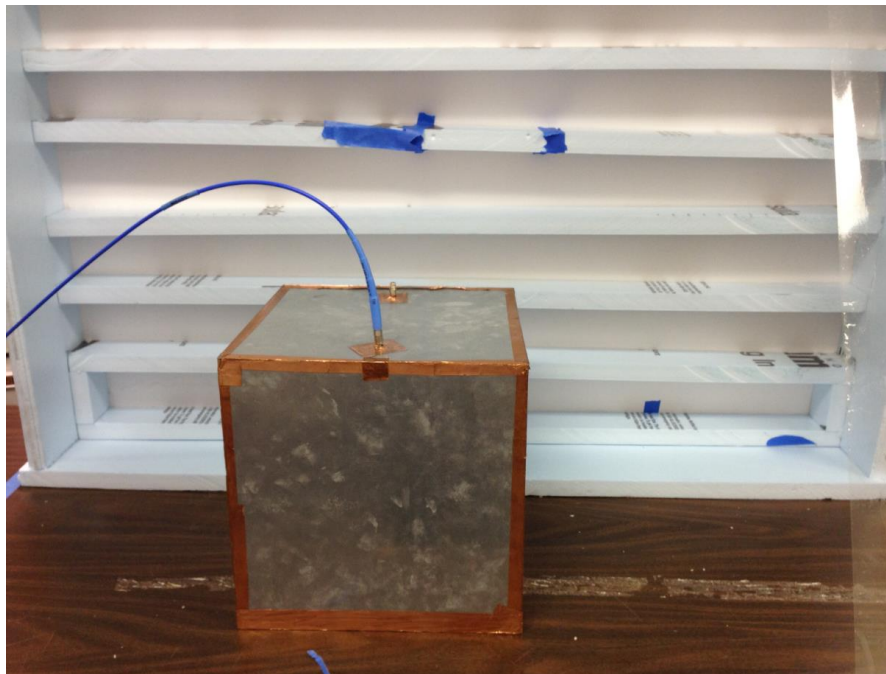


Figure 4.18. Measurement setup

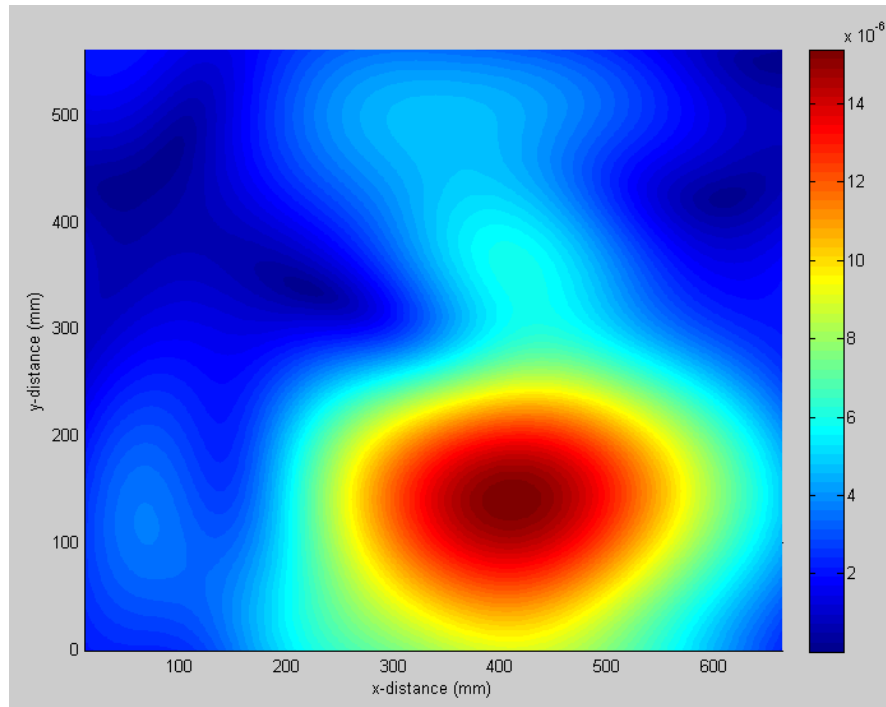


Figure 4.19. Reconstructed source at 1 GHz

When the frequency was set to be 6 GHz, the source reconstruction image was obtained as shown by Fig. 4. 20.

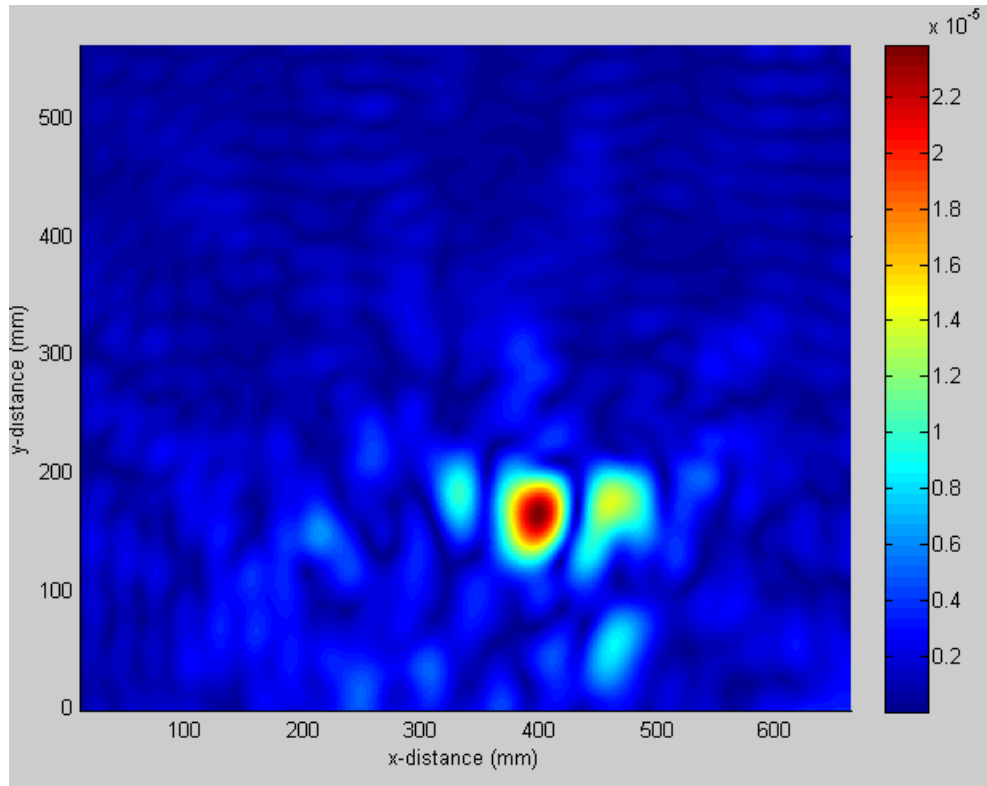


Figure 4.20. Reconstructed source at 6 GHz

By comparing the image at two different frequencies, we can conclude that the algorithm can help determine the location of the slot regardless of the frequency value. At 6 GHz, the reconstructed sources shows one strong source with two weaker sources on each side of the strong source. This indicated a mode image reconstruction on the slot region.

4.3.5. EMI Scanning. The developed system has no restriction on the physical size of DUT, large DUTs can be scanned, which is practically impossible to scan for robotic scanning systems. Shielding effectiveness evaluation can be performed by using the developed system. A metal plate with many holes on it was used as a test DUT.

The layout of the distribution of the holes is shown by Fig. 4.21.

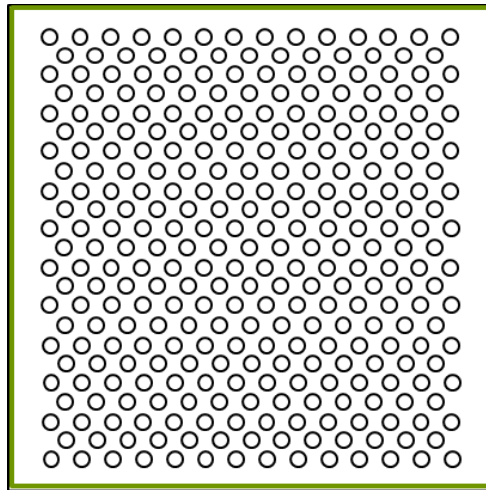


Figure 4.21. Metal plate with holes

Aluminum foil is used to wrap the plate for mimic shielding effect.



Figure 4.22. Metal plate covered by aluminum foil

By poking holes at certain locations, and using an antenna for exciting the poked holes, EMI source reconstruction scanning is setup for evaluating the shielding effects of the setup. The measurement setup is shown by Fig. 4.23. The metal plate wrapped by aluminum foil is put between the source antenna, and the scanning waveguide; Port 1 of VNA was connected with the source antenna; Port 2 of VNA was connected with the scanning waveguide. The frequency is set to be 10 GHz. Again S21 measurement was

conducted to obtain both the magnitude and phase value at each scanning point. Optical tracking system was used for locating the position of the scanning waveguide.

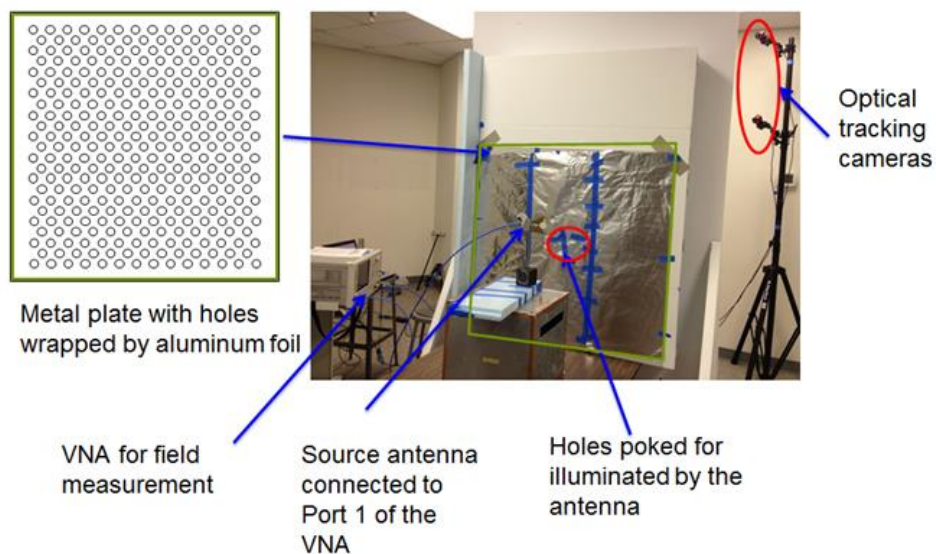


Figure 4.23. Measurement setup

When two holes were poked, the measurement setup and the reconstructed source plane are shown below. From Fig. 4.24, we can observe a good match.

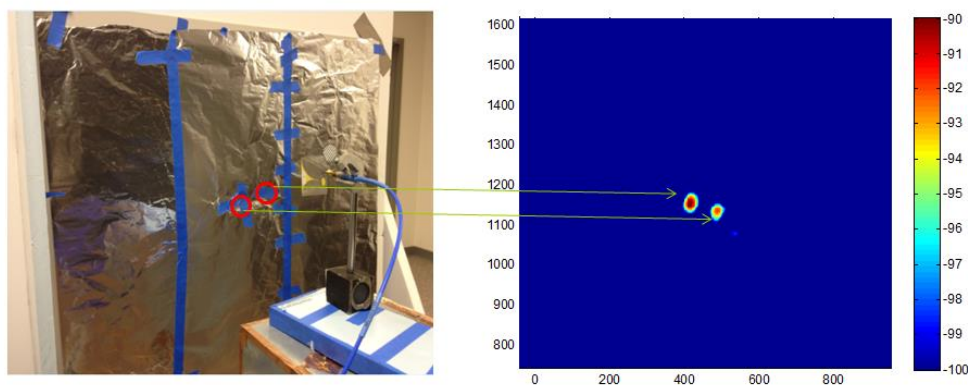


Figure 4.24. Measurement setup and reconstructed source image (in dB scale)

Figure 4.25 shows the comparison between measurement setup and reconstructed source image when five holes were created.

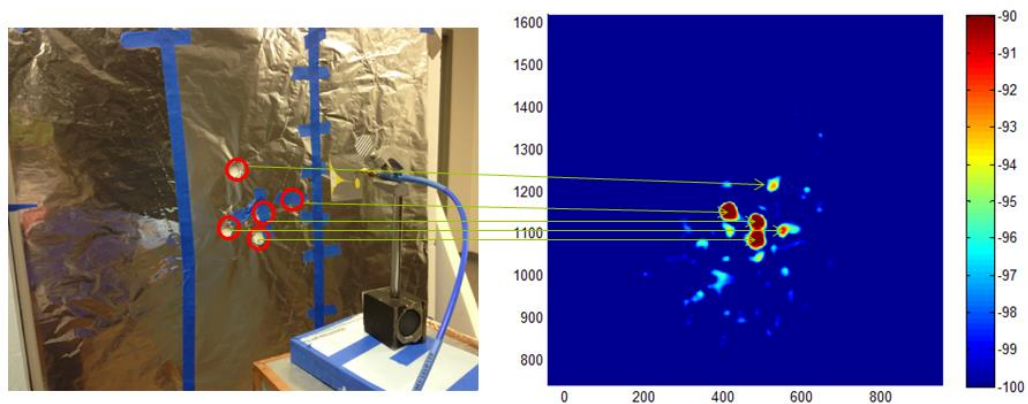


Figure 4.25. Measurement setup and reconstructed source image (in dB scale)

5. CONCLUSIONS AND FUTURE WORK

5.1. CONCLUSION

Probe tracking based manual scanning systems have been developed and validated. Overall, three systems have been prototyped to show the idea of manual scanning with probe tracking capability. These systems utilize the expertise of an experienced EMC engineer and allow complex shaped electronic system of interest to be scanned in an efficient manner. Several applications have been developed and introduced in detail. This first one is visualization of the frequency dependent electromagnetic field distribution. For this application, a test structure was built and scanned. To evaluate the performance of the system, the scanning result was compared with full wave simulation, and a good match was observed. A laptop was also scanned to show the usefulness of the developed system.

Another application is ESM based 2D imaging of far field radiating sources. Traditional robotic scanners preset a scanning grid. So large amount of data points are to be collected, as a result long time is required to obtain a scanning result. In contrast, due to the flexibility of the manual scanning with probe tracked, sparse data sets can be obtained in a short time to determine the location of radiating sources. The developed systems provide a quick and flexible EMI diagnosis solution during the product development stage. Different passive DUTs have been scanned, including two antennas, a customized PCB with two patch antennas excited, a box with a slot on one side, and a cabinet for demonstrating the application of the system on large DUTs.

This system can also be applied to other applications, such as time domain 3D visualization of ESD current spreading, field distribution documentation.

5.2. FUTURE WORK

Far field estimation is very important for EMC compliance. With intense completion, product designers need to develop radiated emission compliant product within a very tight product development schedule. Therefore, the availability of radiated emission measurement facilities and EMI troubleshooting capability is important. Far field measurement using semi-anechoic chamber is a straight forward way to obtain the emission of a prototype. However, semi-anechoic chamber measurement is time and resources consuming. So development of a methodology based on this probe tracking manual scanning system would be very beneficial for designers to effectively and rapidly identify the cause of EMI failure.

This probe tracking system allows near field measurement rapidly and obtains the radiation source effectively with the aid of the knowledge of the designers. By measuring the near field radiation sources using this system, and develop a near field to far field transformation based on amplitude only near field measurement data, would facilitate the EMC countermeasures and enable designers to develop EMC compliant product faster.

BIBLIOGRAPHY

- [1] J. L. Quijano and G. Vecchi, "Near-and very near-field accuracy in 3-D source reconstruction," *IEEE Antennas Wireless Propag. Lett.*, vol. 55, pp. 1046-1049, 2009.
- [2] T. K. Sarkar and A. Taaghola, "Near-field to near/far-field transformation for arbitrary near-field geometry utilizing an equivalent electric current and MOM," *IEEE Antennas Wireless Propag. Lett.*, vol. 47, no.3, pp. 566-573, Mar. 1999.
- [3] W. Huang, D. Pommerenke, X. Jiang, D. Liu, M. Jin, G. Muchaidze, K. Soonjae, and H. K. Ki, "A measurement technique for ESD current spreading on a PCB using near field scanning," *IEEE 2009 International Symposium on Electromagnetic Compatibility*, pp. 18-23, Aug. 2009.
- [4] K. Wang, D. Pommerenke, J. M. Zhang, and R. Chundru, "The PCB level ESD immunity study by using 3 dimension ESD scan system," *IEEE 2004 International Symposium on Electromagnetic Compatibility*, vol. 2, pp. 343-348, 2004.
- [5] Detectus AB [Online]. Available: <http://www.detectus.se/index.html>
- [6] NoiseKen [Online]. Available: <http://www.noiseken.com/>
- [7] Aprel, "EM-ISight Electromagnetic Scanning System" [Online]. Available: <http://www.bizitestequipment.com/pdf/Aprel-EM-ISight-EMI-EMC-Test-System.pdf>.
- [8] K. Sato, H. Kawata and Y. Kamimura, "A Measurement Method for 2-D EMF Distributions Using Infrared Tracker," in *Asia-Pacific EMC Symposium*, 2011
- [9] K. Sato, H. Kawata and Y. Kamimura, "A freehand scanning method for measuring EMF distributions", *IEICE Transactions. J95-B*, No.2, pp.293-301, Feb. 2012.
- [10] K. Sato, H. Kawata and Y. Kamimura, "A measurement of ELF field distributions by using freehand scanning method by Wiimote," in *International Symposium on Electromagnetic Compatibility (EMC EUROPE)*, pp.1-4, Sept. 2012.

- [11] K. Sato, H. Kawata and Y. Kamimura, "A real-time measuring method of 3D EMF distributions using the Wiimote," International Symposium on electromagnetic compatibility (EMC EUROPE), Brugge, Belgium, September 26, 2013.
- [12] Y.Kashimura, K.Sato, Y.Kamimura, "A measuring method for 3-D EMF distribution in ELF-VLF band using the Wiimote," EMCJ Dec 2012.
- [13] H. He, P. Maheshwari, A. Radchenko, and D. Pommerenke, "EM radiation estimation using an automatic probe position recording system coupled to hand scanning," IEEE 2013 International Symposium on Electromagnetic Compatibility, Denver, CO, Aug. 5-9, 2013.
- [14] H. He, P. Maheshwari, and D. Pommerenke, "Optical tracking based EM-field probing system for EMC near field manual scanning," IEEE 2014 International Symposium on Electromagnetic Compatibility, 2014.
- [15] CH Robotics, CHR-6dm Attitude and Heading Reference System product datasheet – Rev. 1.1, Preliminary.
- [16] "what is can bus", [Online] <http://canbuskit.com/what.php>
- [17] B. Hofmann-Wellenhof, K. Legat, M. Wieser, Navigation, Principles of Positioning and Guidance, Springer-Verlag, Wien, 2003
- [18] J. D. Foley, A. v. Dam, S. K. Feiner, J. F. Hughes, and R. L. Phillips, Introduction to Computer Graphics. Reading, MA: Addison-Wesley, 1994.
- [19] NaturalPoint, Inc, Optitrack, [Online], www.naturalpoint.com/optitrack
- [20] Imagination Computer Services GmbH, iotracker, [Online], www.iotracker.com
- [23] EMCoS Ltd., EMCoS EMC Studio, Version 7.0, [Online], www.emcos.com
- [24] W. Boehler, A. Marbs, "3D Scanning instruments," Proceeding of the CIPA WG6 International workshop on scanning for cultural heritage recording, 2002.

- [25] Canny J, "A Computational Approach to Edge Detection," IEEE Transactions PAMI 1986, Vol 10, pp. 679-698.
- [26] Z. Yang, Y.R. Zheng, "Near-field 3-D synthetic aperture radar imaging via compressed sensing," IEEE Int'l Conf. Acoustics, Speech, Signal PROCESSING, ICASSP'12, 1520-6149 (2012), pp. 2513-2516, <http://dx.doi.org/10.1109/ICASSP.2012.6288427>
- [27] Z. Yang, Y.R. Zheng, "A comparative study of compressed sensing approaches for 3-D synthetic aperture radar image reconstruction", Digit. Signal Process. 32, 24–33 (2014). doi:10.1016/j.dsp.2014.05.016
- [28] Z. Yang. "Sparse nonlinear optimization for signal processing and communications," Ph.D. dissertation, Missouri University of Science and Technology, 2014.
- [29] H. Kajbaf, J.T. Case, Z. Yang, Y.R. Zheng, "Compressed sensing for SAR-based wideband three-dimensional microwave imaging system using non-uniform fast Fourier transform," Radar, Sonar & Navigation, IET , vol. 7, no. 6, pp. 658-670, July 2013.
- [30] P. Maheshwari, V. Khilkevich, D. Pommerenke, H. Kajbaf, J. Min, "Application of Emission Source Microscopy to EMI source localization," IEEE EMC Symposium, 2014.
- [31] J. T. Case, M. T. Ghasr, and R. Zoughi, "Nonuniform manual scanning for rapid microwave nondestructive evaluation imaging," IEEE Trans. Instrum. Meas., vol. 62, no. 5, pp. 1250–1258, May 2013.
- [32] C.A. Balanis, "Antenna theory: Analysis and design," 3rd Edition, April 2005.

VITA

Hui He was born in Chenzhou, China. She received her Bachelor degree in Industrial Design in 2006 and Master degree in Mechanical Design and Theory in 2009, both from Sichuan University, Chengdu, China. She received her Master degree from Missouri University of Science and Technology, electromagnetic compatibility laboratory in August 2015. Her current research interests include near field measurement and instrumentation, electromagnetic compatibility (EMC) measurement and simulation, and signal integrity measurement and simulation.